U.S. DEPARTMENT OF ENERGY

PNNL-24356

Prepared for the U.S. Department of Energy
under Contract DE-AC05-76RL01830

Final Report: Nanolayered, self-healing radiation shielding foils

CH Henager, Jr. (PI)
W Setyawan

June 2015

Pacific Northwest
NATIONAL LABORATORY

Proudly Operated by Battelle *Since 1965*

PACIFIC NORTHWEST NATIONAL LABORATORY
operated by
BATTELLE
for the
UNITED STATES DEPARTMENT OF ENERGY
under Contract DE-AC05-76RL01830

Printed in the United States of America

Available to DOE and DOE contractors from the
Office of Scientific and Technical Information,
P.O. Box 62, Oak Ridge, TN 37831-0062;
ph: (865) 576-8401
fax: (865) 576-5728
email: reports@adonis.osti.gov

Available to the public from the National Technical Information Service
5301 Shawnee Rd., Alexandria, VA 22312
ph: (800) 553-NTIS (6847)
email: orders@ntis.gov <http://www.ntis.gov/about/form.aspx>
Online ordering: http://www.ntis.gov


This document was printed on recycled paper.
(8/2010)

Grant/Award #: HDTRA1-08-10-BRCWMD-A
PI Name: CH Henager, Jr.
Organization/Institution: Pacific Northwest National Laboratory
Project Title: Nanolayered, self-healing radiation shielding foils

What are the major goals of the project?

This work addressed the fundamental hypothesis that interface character does not play as critical a role as does interface spacing for the design of radiation damage tolerant materials when the spacing of the interfaces can be controlled in the nanoscale regime. We created, characterized, and modeled basic types of interfaces for the hypothetical design of a damage tolerant metallic foil shielding material having low atomic number, such as Al and Ti. The two types of interfaces include a coherent or semi-coherent "elastically hard" interface with large strain gradients and an incoherent "elastically soft" interface such as those produced between FCC and BCC materials. We created nearly perfect single interfaces that were probed using a suite of high-resolution instruments in order to understand the fundamentals of radiation damage at specific interfaces with well-characterized structures and properties. Modeling and simulation of radiation damage combined with the experimental studies explored the effects of layer thickness and metal/ceramic ratio in the alternating layers. We addressed the question of interface spacing versus interface structure by varying layer spacing in subsequent multi-layered materials in the atomistic models. We determined that neither layer spacing nor layer structure completely governed the behavior of these nanolayered systems as long as the layers are thin with respect to diffusional distances, rather it was the unequal damage that occurred in the layers and the unequal defect fluxes that dictated defect accumulation in these materials.

The project was outlined as follows for each of the three years:

Year 1,2, and 3

- Task 1: Synthesis of multilayer nanoscale structures
- Task 2: Material Characterization
- Task 3: Influence of Ion Irradiation on Films and Interfaces
- Task 4: Modeling and Simulation

What was accomplished under these goals?

1. Summary of Accomplishments

This research has reached some surprising conclusions that were unexpected at the beginning of the research. We were unaware of the major finding of nanolayered defect partitioning until we performed MD simulations of damage in the Al/Ti nanolayered system as reported here. These results were surprising and, unfortunately, bad news for the use of these materials in radiation fields or to high damage doses. The hope for a radiation damage tolerant material based on nanolayered materials is not well founded based on our results.

This work has revealed several important properties of Al/Ti nanolayers in response to radiation damage. During maximum damage production initiated with 1.5-keV PKA, asymmetry in the point defects creation between the two dissimilar materials Al or Ti is observed with ~60% of vacancies are created in Al films while ~70% of interstitials are created in Al films. The excess interstitials in the Al films is a direct consequence of the preferential flux of displaced atoms in this nanolayered system. He irradiation experiments at a low dose of 10^{16} atoms/cm^2 and at room temperature were performed to investigate the interface effects on radiation damage. The experimental data shows a formation of ~1-nm diameter bubbles in the Ti films near the interface. The results from the simulations and experiments seem to suggest that the bubble formation is associated with the preferential flux of SIAs during the irradiation in that the He atoms impinge on the Ti films and displace the Ti atoms into the Al films.

In all of the interface models in this study, the number of Frenkel pairs created during maximum damage production was smaller than the bulk average of the constituent materials. This discrepancy is amplified towards thinner films. This is understood using a phenomenological model that Ti exhibits a larger stopping power than Al and that the fraction of energy deposited in Ti films increases as the films are made thinner. On the other hand, the number of surviving Frenkel pairs at the end of simulations is larger than the bulk average. The difficulty for anti-defect recombination is caused by defect partitioning in which in Al films there are too many interstitials than the available vacancies while the opposite applies in Ti films. This defect partitioning increases with the increasing number of interfaces (thinner films) resulting in more than 90% of surviving interstitials are located in the Al films.

2. Technical Research

To accomplish the goals outlined above the following activities were carried out: 1) Thin films of Al/Ti alternating layers were sputter deposited onto Si or MgO substrates and were carefully characterized, 2) the films were subjected to ion irradiations and He implantation and were then studied post-irradiation, and 3) computational models were used to study film deposition and radiation damage in nanolayered Al/Ti films.

3. Al/Ti Synthesis and Characterization

The thin films consisted of alternating layers of Al and Ti with layer thicknesses of 5 to 50 nm in order to determine the effects of interface spacing as discussed in the objectives. Figure 1 shows a cross-section view of layered thin film with a corresponding X-ray diffraction pattern. Figure 2 shows the 20-nm and 5-nm films for comparison.

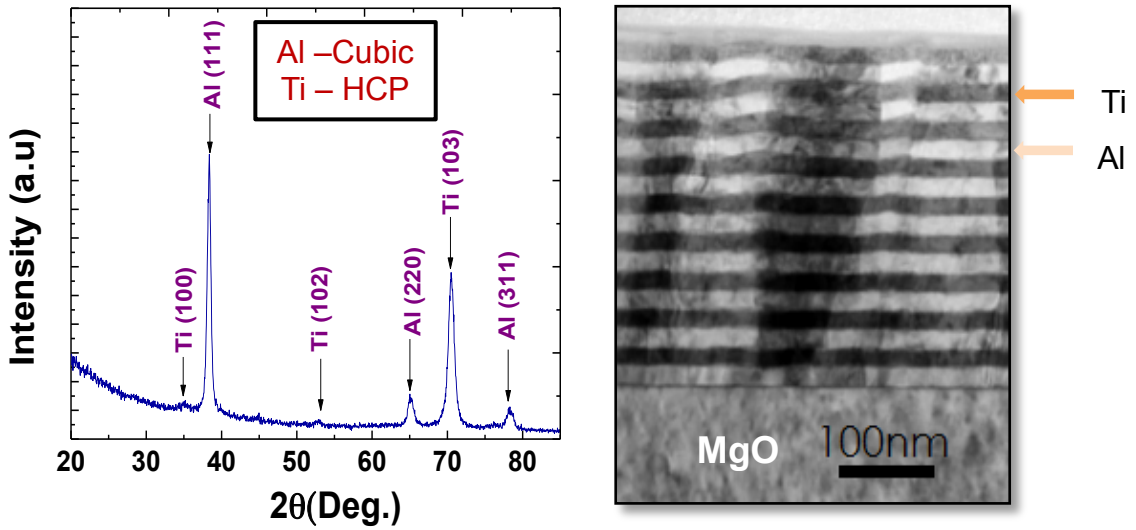

(a) (b)

Figure 1. An X-ray diffraction pattern taken under glancing incidence in (a) and a cross-section TEM image of a sputtered thin Al/Ti layered film on MgO in (b). The layers here are 20 nm thick for a bilayer period of 40-nm. The XRD pattern reveals that Al is fcc and that Ti is hcp.

These films were then characterized using a combination of techniques, including transmission electron microscopy (TEM), Rutherford backscattering (RBS), glancing incidence X-ray diffraction (GIXRD), and atom probe tomography (APT) to determine morphology and composition of the layers. These methods became the standard methods for thin film characterization and were also used to determine the effects of radiation damage on the layered structure. In addition, He-ion microscopy (HIM) was used to both implant He into the films but also to image the films. However, the best imaging was obtained using TEM and STEM methods for under- and over-focused image conditions to examine the layers for He and He bubble formation. Ion irradiation was also accomplished using Au ions in the PNNL accelerator system.

RBS was used to characterize initial thin film depositions to explore layer thickness and perfection in a geometry that was consistent with ion irradiations as shown in Figure 3. Thus, the films could be characterized before and after ion irradiations without removing the samples from the vacuum chamber. These initial results indicated a very good correlation between RBS thickness calculations and TEM image data. This agreement is indicated in Figure 4 for RBS data on the 20-nm thick nanolayered sample.

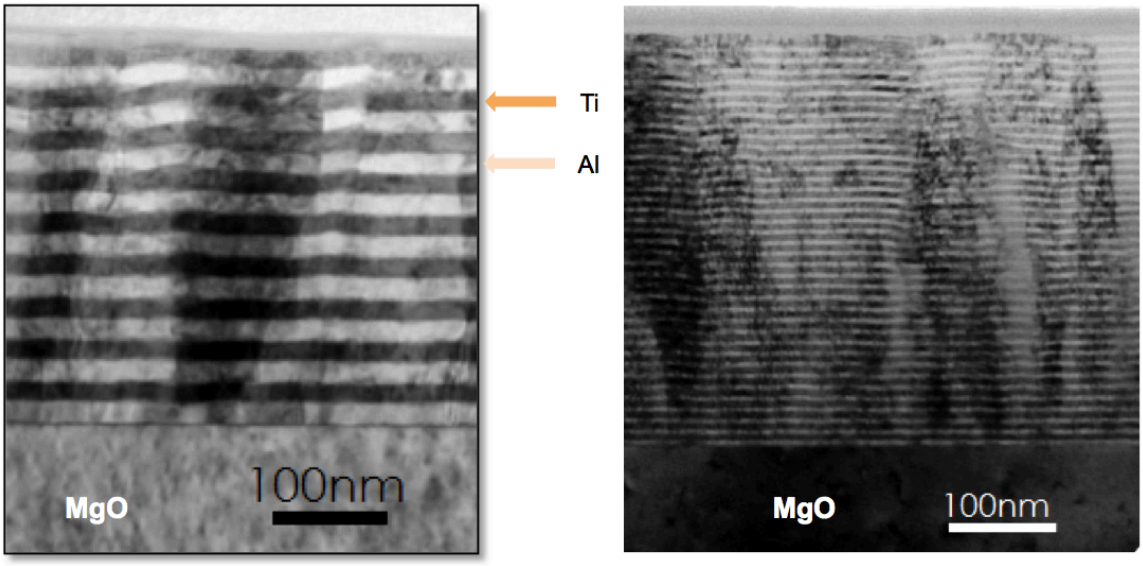

(a) (b)

Figure 2. Cross-section TEM images of sputtered Al/Ti nanolayered films on MgO. In (a) the layers are 20-nm thick for a bilayer period of 40-nm and in (b) the layers are 5-nm thick or 10-nm bilayer period.

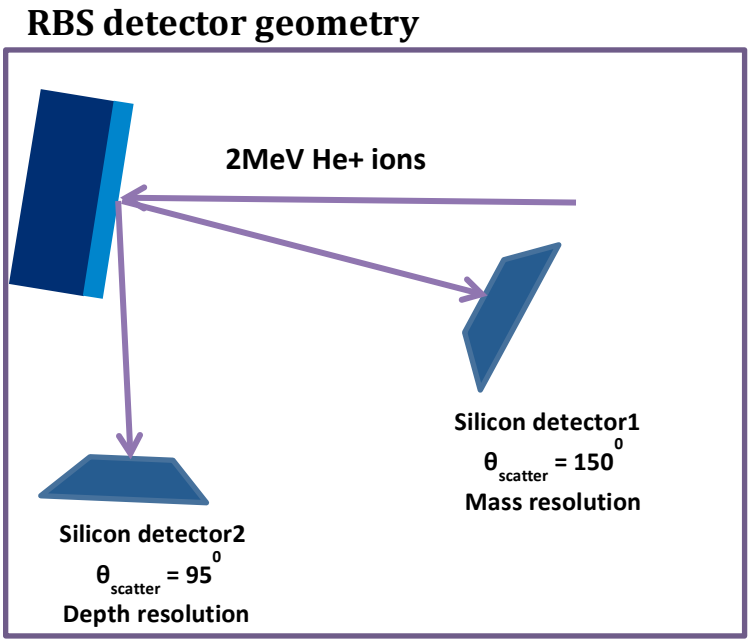

Figure 3. A schematic of the RBS method using 2 MeV He^+ ions and the scattering geometries employed.

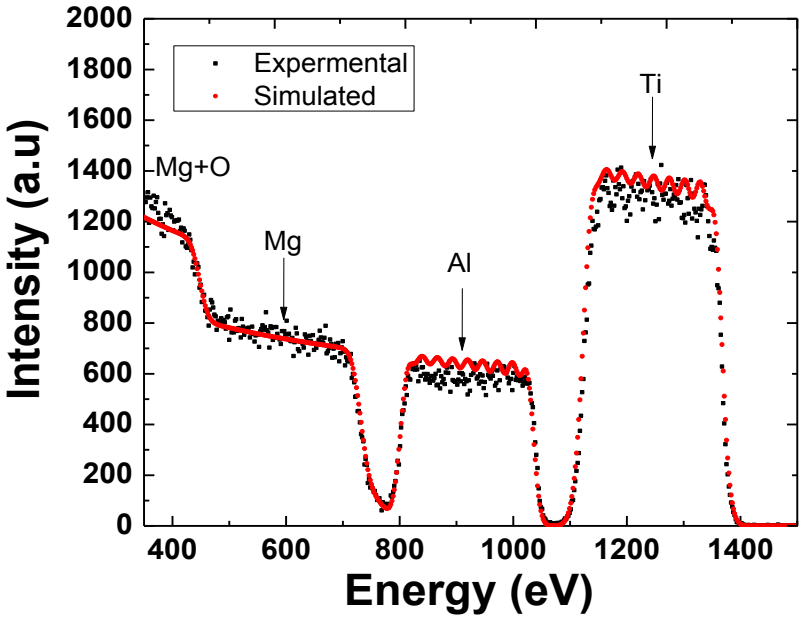

Figure 4. RBS data showing the resolution of the separate Al and Ti layers for the 20-nm thick nanolayered film. The layer thickness calculated was 20 nm for the Al layers and 18 nm for the Ti layers, which agrees well with the TEM images in Fig. 2.

The use of APT was restricted to the early phases of this project to demonstrate that the thin films could be examined for compositional profiles but the APT data was not as useful for the irradiated films. For these examinations, high-resolution TEM was still the best option. Therefore, initial APT results were reported in the first annual review in 2011 but were not repeated.

This task was very successful in preparing thin nanolayered films of Al/Ti for this study. The sputter deposition process worked quite well on either Si or MgO and produced all the materials necessary for the three-year study. The films with 5-nm layers or 10-nm bilayer period were the thinnest layers produced and films up to 80-nm thick layers in a tri-layer Al/Ti/Al arrangement were produced.

4. Ion irradiation and He implantation studies

Various Al/Ti films were ion irradiated using Au ions and films were implanted using He ions. The Au ion irradiations were too severe and little useful information was generated by this method. In contrast, the He ion implantation using the HIM proved to be very useful in understanding the damage processes in Al/Ti films and proved to be the key in our understanding of the damage asymmetry issues in nanolayered thin film materials in general.

Figure 5 shows the results of irradiating a tri-layer Al/Ti/Al film with 1 MeV Au ions. The Au ions pass through the tri-layer film causing radiation damage in the form of small voids (bright dots in the TEM image) but leaving the layered structure intact. The dose was 1 x 10^{17} Au/cm^2 at room temperature, which corresponds to about 80 dpa at the peak of the Au damage range in the Si substrate.

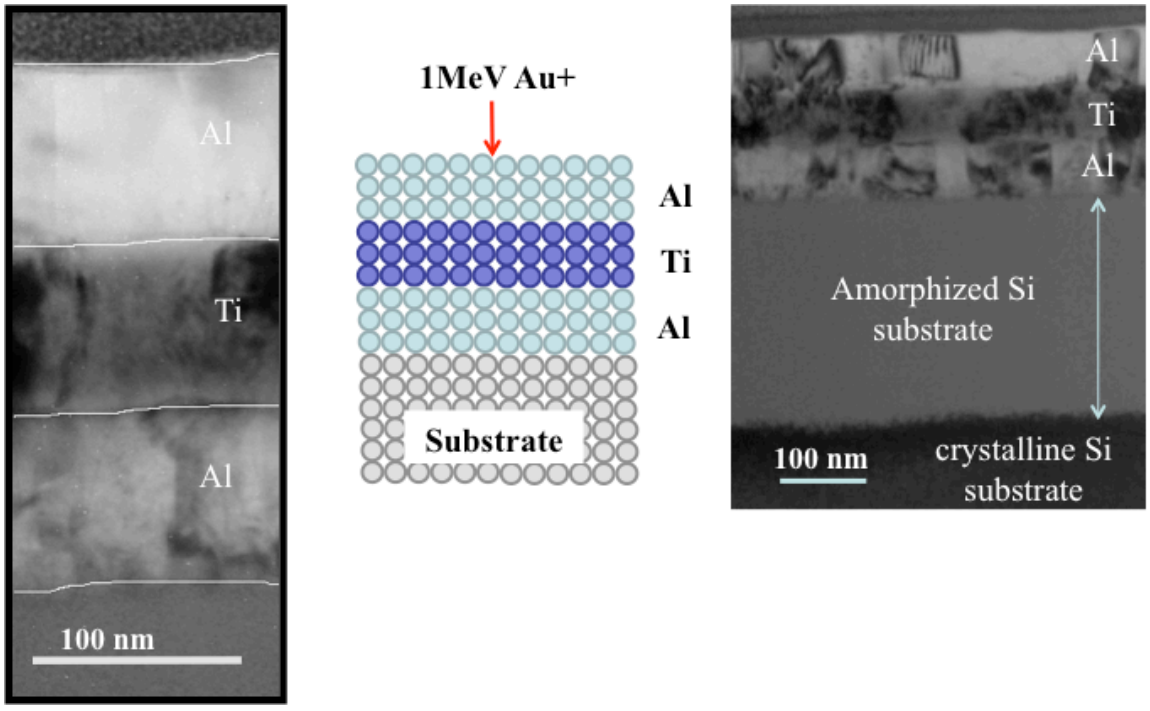

(a) (b) (c)

Figure 5. TEM images of Au ion irradiated tri-layer film in (a) and (c) with a schematic of the irradiation geometry shown in (b). The Au ions pass through the tri-layer film and stop in the Si substrate causing a crystalline to amorphous phase transition in the Si substrate. Small voids can be seen in the Al and Ti layers in (a) as the small bright dots in the image.

Figures 6 and 7 shows the results of a series of Au ion irradiations on the 20-nm and 5-nm nanolayered films where the films are irradiated at ambient temperature and imaged in the TEM in cross-section. The layered structure for both nanolayered films is gradually destroyed and replace by an amorphous region with Ti_3Al crystalline regions located at the top of the film and at the interface between the film and the substrate. These doses and dose rates are too high to learn much about the films ability to demonstrate radiation damage tolerance. 1 $x10^{17}$ Au ions/cm^2 is about 80 dpa and the dose rate was about 5 x 10^{-3} dpa/s, which is very high. These Al/Ti films cannot handle that dose rate. Thus, the ion irradiation portion of this study was not as useful as it could have been if lower dose rates and lighter ions had been used to produce more gradual damage. Also, very little differences are observed between the two films even though there is a factor of 4 difference in bilayer period.

These results did not contribute to our understanding of the effect of layer thickness on damage accumulation in Al/Ti nanolayered films. However, the results do represent a significant learning opportunity for the post-docs and students working on the project and illustrate how to improve these experiments in the future.

After this realization, we began to perform more detailed experiments using our HIM to implant He ions at 30 keV into nanolayered films. Others were doing this in this community and we immediately found a significant result that was directly corroborated by our modeling efforts.

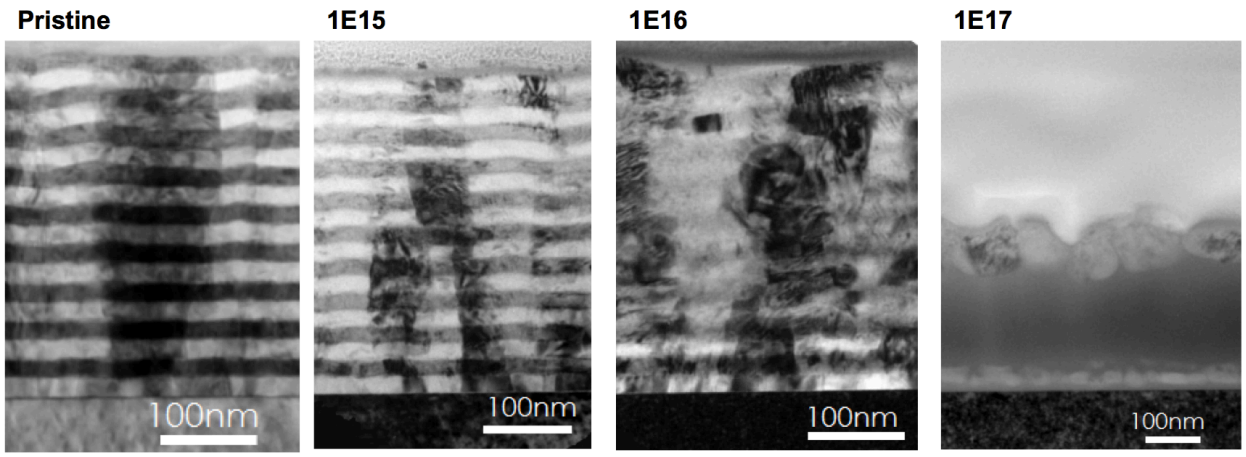

(a) (b) (c) (d)

Figure 6. TEM images of 20-nm thick or 40-nm bilayer period Al/Ti films with (a) as-deposited, (b) after 1 x 10^{15} Au ions/cm^2, (c) 1 x 10^{16} Au ions/cm^2, and (d) 1 x 10^{17} Au ions/cm^2. The layered structure gradually disappears and is replaced with an amorphous region with Ti_3Al crystallites.

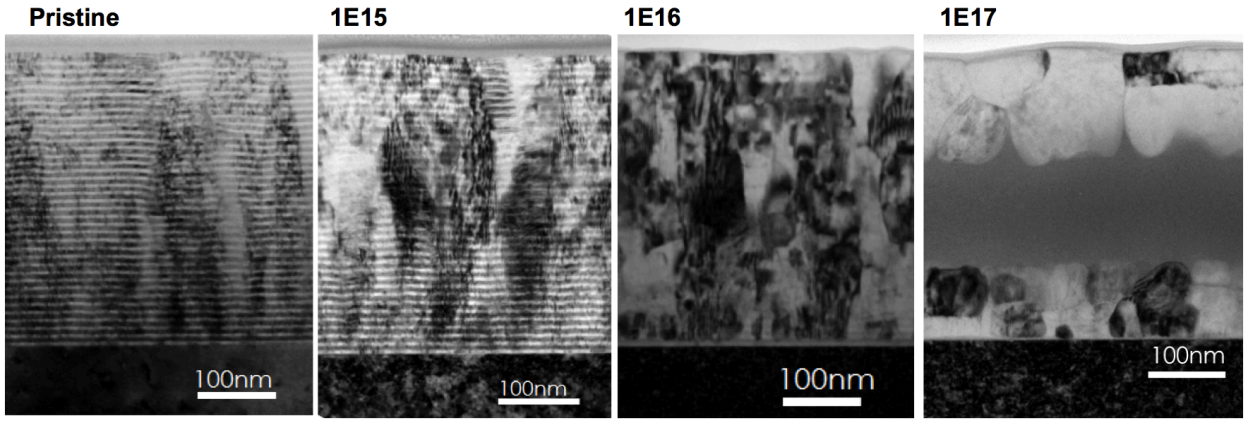

(a) (b) (c) (d)

Figure 7. TEM images of 5-nm thick or 10-nm bilayer period Al/Ti films with (a) as-deposited, (b) after 1 x 10^{15} Au ions/cm^2, (c) 1 x 10^{16} Au ions/cm^2, and (d) 1 x 10^{17} Au ions/cm^2. The layered structure gradually disappears and is replaced with an amorphous region with Ti_3Al crystallites.

Figure 8 shows the setup in the HIM using an image obtained in a focused ion beam (FIB) scanning electron microscope (SEM). A small area (volume) of the 10-nm bilayer Al/Ti films was irradiated in the HIM using 30 keV He ions to a dose of 1 x 10^{16} He ions/cm^2 at ambient temperature. This region plus an undamaged adjacent region was prepared for cross-section TEM imaging in the FIB-SEM by ion milling. A Pt cap is placed over the region and the entire milled sample is lifted out for TEM examination. The irradiated region is then imaged in cross-section in the TEM at high resolution and small He bubbles are observed. The key to our new understanding of damage processes in these Al/Ti foils comes from the observation that the He bubbles are contained only within the Ti layers and no He bubbles are visible in the Al layers.

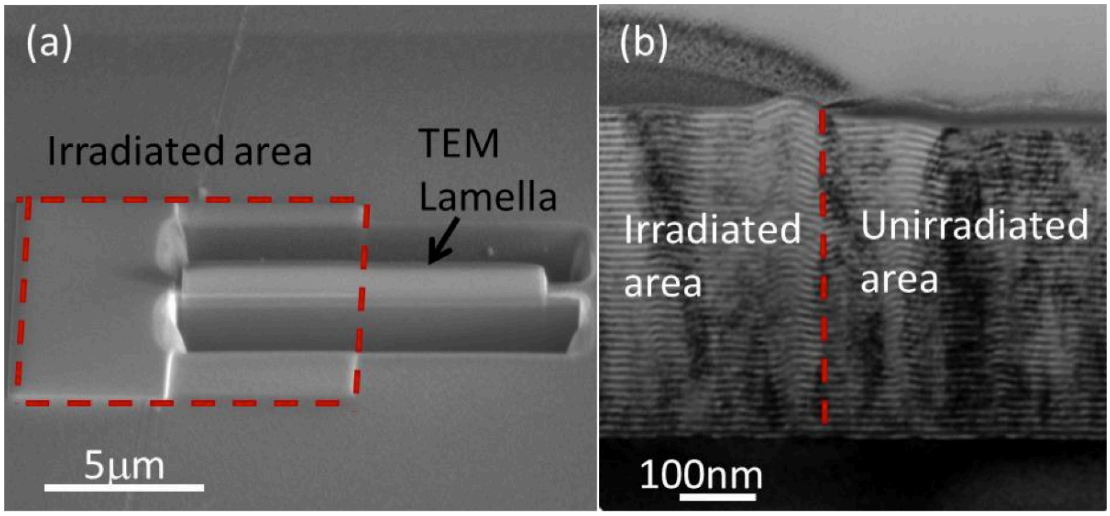

(a) (b)

Figure 8. FIB-SEM image of He implanted region in (a) and a cross-section TEM image of the FIB sample after liftout. The irradiated area in (b) is shown at higher magnification and in both overfocused and underfocused condition in Figure 9.

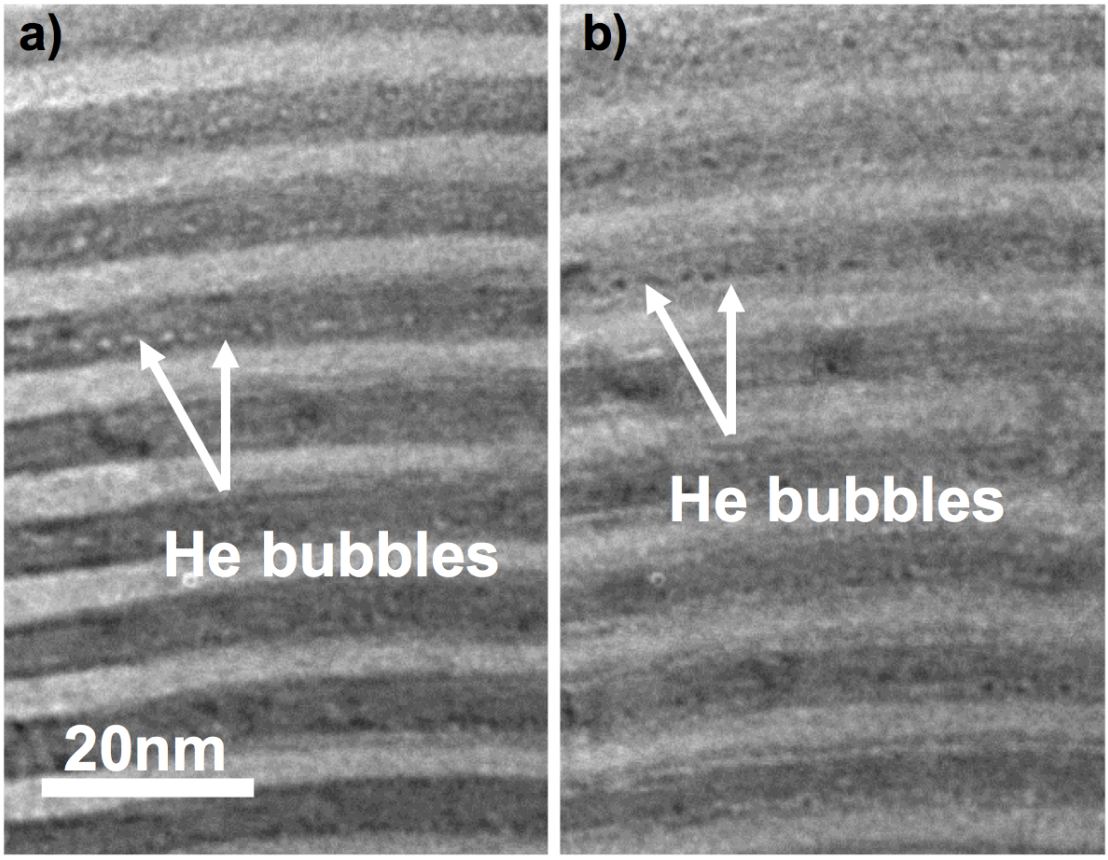

Figure 9. High-resolution TEM images in cross-section of the He-ion damaged region of the 10-nm bilayer period Al/Ti film shown in Fig. 8. Small He bubbles are imaged in the foil but are contained only in the Ti layers, which are the darker layers in these images. The bubbles are bright in the over-focused image in (a) and dark in the under-focused image in (b) as expected.

The use of low energy He ion implantation to study ion beam mixing and radiation damage in nanolayered thin films is useful since He damage rates are reduced compared to heavy ions, the ranges are appropriate for thin films, and the effects of He accumulation are relatively easily observed compared to point defect clustering as a measure of radiation damage. It is understood that He bubble formation proceeds from vacancy (V) accumulation and He-V binding. Thus, observing He bubbles is a surrogate for observing V clustering in these thin film materials. Höchbauer et al. [1] were the first to study He accumulation as bubbles in Cu-Nb nanolayered materials. They observed preferential He bubble formation at Cu-Nb interfaces and columnar grain boundaries following 33 keV He implantation. Demkowicz et al. [2] concluded that He also accumulates along Cu-Nb interfaces and that these interfaces act as fast diffusing pathways for He escape during annealing.

Zhang et al. [3] observed that He bubbles were not resolvable in Cu-Nb 2.5-nm layered foils, whereas identical 33 keV He implantation produced TEM visible bubbles in pure Cu, pure Nb, and Cu-Nb 100-nm layered materials. This was assumed to be evidence that Cu-Nb 2.5-nm layered materials exhibited enhanced recombination of radiation-induced point defects and, thus, much smaller He bubbles, less than about 1 nm in diameter. Zhernenkov et al. used neutron reflectometry to study He locations in implanted Cu-Nb foils and concluded that He was likely being stored as interstitial He in the dissimilar interfaces until a critical concentration is reached, after which He bubbles are formed [4]. Perhaps the best evidence comes from ^{3}He implantations and using nuclear reaction analysis (NRA) to study He concentrations as a function of implantation depth together with TEM to determine He concentrations where He bubbles form [5]. Similar conclusions were reached by Bhattacharyya et al. using TEM and NRA to study ^{3}He-implanted Cu-Nb foils [6]. Interface structure appears to play a critical role in the amount of He that can be stored before bubbles form [7]. Recent MD studies are consistent with this understanding and demonstrate atomic storage mechanisms for He in certain interfaces [8, 9].

However, once this critical concentration of He is reached then He bubbles can nucleate and grow in these layered materials just as in bulk metals. A key difference, though, is that He bubble morphologies and locations vary from layer to layer and, above a certain dose, appear to depend on some intrinsic property of the layer material rather than the interfaces [10]. Hattar et al. [11] observed He bubbles in both the Cu and Nb layers of a Cu-Nb 5 to 6-nm layered foil after high doses of 33 keV He ion implantation at 763 K. However, He bubbles in the Cu layer spanned the thickness of the entire layer and were approximately 5 to 6 nm in diameter, whereas He bubbles in the Nb layer were about 1 to 2 nm in diameter. Similar observations of He bubble suppression compared to bulk or 100-nm layered materials are observed in Cu-V nanolayered foils [12] and in Cu-Mo nanolayered foils [13], where a slight size difference between He bubbles in Cu (larger) compared to Mo layers was noted. Wei et al. [14] observed bubble size differences in Ag-V nanolayered materials somewhere between the Cu-Nb size differences and those observed for Cu-V, with the larger bubbles contained in the Ag layer. Fu et al. nicely summarize dose effects in Cu-V nanolayered systems and discuss He effects, radiation hardening, and both mixing and demixing effects observed in other systems [15].

One trend that appears to be consistent in these nanolayered studies is the observation that a certain level of asymmetry develops with regard to He bubble morphologies at increased He doses. Bubble sizes are non-uniform after a certain dose and the evidence is not clear that this asymmetry does not develop earlier in the radiation damage regime. He storage at the dissimilar interface does not destroy the symmetry of the system, although, asymmetric swelling amounts are often noted [4, 10-12], along with asymmetric He bubble sizes [11]. These become serious issues with dealing with nanolayered failure mechanisms due to radiation damage, perhaps from delamination or other mechanical failures due to differential responses.

One shortcoming in the current literature and that is addressed in this research is the lack of understanding of point defects in nanolayered systems at low energies where ion beam mixing and demixing effects do not occur readily. In particular, displacement thresholds have not been studied for any of these layered systems to help understand or predict if some part of the response asymmetry may be due to displacement threshold effects. There is no reason to expect that defect generation or fates are symmetric within nanolayered materials made up of dissimilar metals. Under asymmetric defect generation the ability of the system to avoid damage accumulation via enhanced recombination may be compromised. One layer may accumulate an excess of one kind of point defect or defect cluster over time. The differential He bubble size observed in Cu-Nb suggests that this type of damage cannot be overlooked or ignored.

This leads directly to our modeling task, which was the most successful task once the He ion irradiation data was discovered.

5. Computational Modeling and Simulation

Several key contributions to the science and technology of nanolayered foils (films) were made in this task and each will be described. First, it was noted that during the Al/Ti synthesis work that intermixing was observed in all of the films that were made regardless of sputtering rate or deposition conditions. Second, a search of the literature revealed that there was no threshold data for radiation damage in multilayered materials and that this would be a strong contribution to the field, as well as provide us with valuable information for other simulations. Third, there was a surprising lack of MD simulations of radiation damage in nanolayered materials and we performed some of the most comprehensive MD studies of this in the Al/Ti system and learned important things that are generalizable to other systems with some caveats.

The simulations start with a good interatomic potential and that was supplied by Zope et al [16] in the Al-Ti system. We modified the potential for short-range interactions using the well-known ZBL form [17] with the interactions computed using ab initio methods for improved accuracy. This modified potential has been made available for others to use. This allowed us to start to study Al/Ti films for this project. This short-range modification is shown in Figure 10.

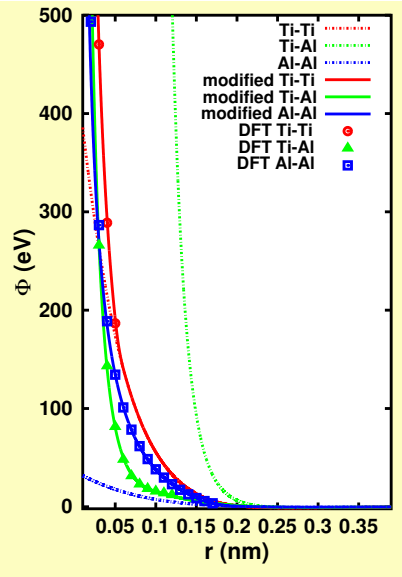

Figure 10. The ZBL short-range interaction portion of the Al-Ti EAM potential modified to perform MD simulations of radiation damage.

Figure 11 illustrates our first significant computation. We observed sputtered Al/Ti layered films were characterized by rough interfaces and that some roughness was apparently unavoidable. We simulated the vapor deposition of Al on Ti and Ti on Al as shown schematically in Fig. 11. There were MD results and demonstrated that when Ti atoms are deposited on an Al surface that the heat of adsorption was enough to cause the Ti atoms to dislodge the Al atoms on the surface and cause some degree of mixing regardless of the incoming Ti energy. Thus, Al/Ti films will have a certain amount of roughness that cannot be prevented. Fig 11(b) shows this in data as a function of adatom incident energy. The Ti on Al(111) curve lies far above the other curves and shows the predicted trends.

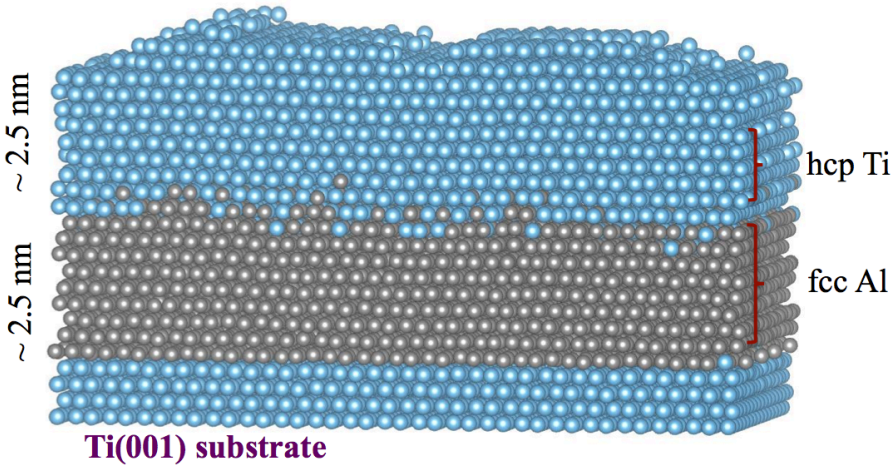

(a)

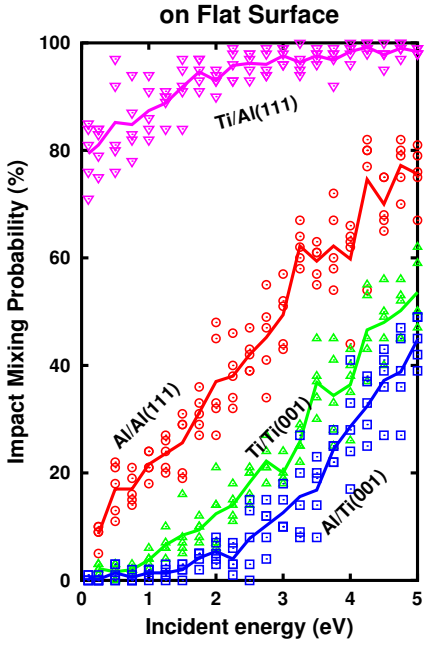

(b)

Figure 11. Shown in (a) is an atomic model of Al/Ti film after deposition. The Ti/Al interface roughness is distinct. In (b) is the roughness data in terms of layer intermixing probability as a function of adatom energy for the Ti-Al system. Ti on Al will always result in some intermixing.

The second major contribution to nanolayered thin films and radiation damage was to use the modified Al-Ti potential to compute the damage threshold for the Al/Ti layered system, although for only one layered configuration. A computational method was developed and evaluated for this work and the results are in the process of being published. Compared to bulk Al or bulk Ti, a nanolayered Al/Ti system has higher damage thresholds but similar angular dependencies. One observation that was made here and will be significant later is that within a single elemental layer there are threshold differences depending on the location within the layer, the center of the layer being different compared to the interfaces. The threshold data is summarized in Figure 12 using an Al atom as the primary knock-on atom (PKA) in this case.

The major difference between a multilayer thin film and bulk materials is that the threshold is more complex and can also be a function of location within the nanolayered film whereas it is not a function of location within a single crystal of bulk material. The relative peaks are similar and are dictated by crystallographic considerations. The peak magnitudes likely have to do with local lattice strain.

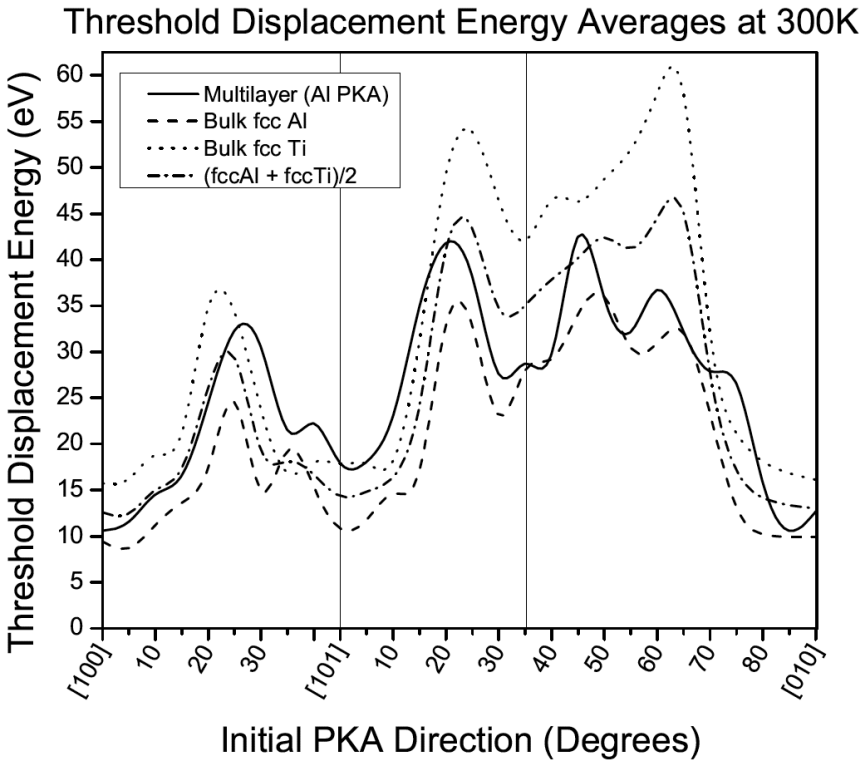

Figure 12. Summary plot of threshold displacement energies in eV for Al/Ti multilayer thin film with cube-on-cube orientation as a function of initial PKA direction. The multilayer data is the first of its kind (solid line) and indicates subtle differences between these calculations and similar bulk material calculations. In general the multilayer system lies between that for bulk fcc Ti and bulk fcc Al.

The third, and by far the most important finding of this computational task, is that there is a large asymmetry in the radiation damage production, which was first noticed in the threshold calculations, and a large asymmetry in the residual defects within individual nanolayers that depends in a complex may on the local environment. The main effect of this is that non-uniform radiation damage is extremely deleterious to nanolayered film performance with increasing radiation dose such that eventual system failure is almost assured. In other words, the system cannot compensate for this damage asymmetry even by decreasing the rate of defect

accumulation through enhanced recombination via interfacial design. Gradually, the non-uniform defect accumulation causes irreversible damage in one layer compared to the other layer commensurate with the ratio of defect accumulation in the layers. We will illustrate this effect with our calculations in the Al/Ti system but similar effects can be discerned from the literature on the Cu/Nb system as well.

In terms of nanolayered system, the Cu/Nb system is the prototypical immiscible materials combination with superior radiation damage resistance below a certain threshold dose, as will be seen, while the Al/Ti system could be considered the prototypical miscible system. The immiscibility adds to the damage resistance by either demixing atoms the cross the interface or by acting to maintain a sharp biomaterial interface. The Cu/Nb system is further characterized by a complex and defected interface that effectively stores point defects and He atoms [1, 18].

Our work began by constructing a series of possible Al/Ti nanolayered systems and initiating a low energy collision cascade randomly in the system. However, even with random cascades the initial PKA begins within a certain layer and the damage peak occurs within a certain layer so that the damage can be delineated by layer type. This will be done when we examine the results.

LAMMPS software was used to perform the MD simulations. Periodic boundary conditions (PBCs) were employed in all dimensions. Before the displacement cascade was initiated, each structure was thermalized at 300 K and zero pressure for 30 ps. To obtain a proper canonical distribution of velocity, the thermalization was performed using a thermostat with a time step of 0.5 fs and a 1-ps damping parameter. To initiate the collision cascade, a random primary-knock-on atom (PKA) was chosen and was assigned an initial velocity normal to the stacking direction. Throughout this study, the PKA was given an initial kinetic energy of 1.5 keV. This PKA energy is sufficient to cause damage across most of the interfaces in the multilayer and yet small enough to avoid overlaps of damage regions due to PBCs.

The total simulation time was approximately 55.5 ps. For each structure, 20 runs were performed. In multilayer structures, ten runs with Al PKA and ten runs with Ti PKA were done. Within each system, only one initial thermalization run was performed. All damage cascades in this system were started from the same thermalization restart file. For defect counting analysis, a reference configuration was generated with molecular static energy minimization in each system. Voronoi cells were then constructed using these reference sites. Unoccupied cells were identified as vacancies and the number of vacancies was taken as the number of Frenkel pairs.

Five multilayer families (systems) were investigated: M_{fcc}, M_{hcp}, M_{100}, M_{cp} and M_{cpic}. Within each system, four multilayers were constructed with different film thickness: three, six, 12 and 24 layers per film. In this study, the keyword film refers to Al film or Ti film. The multilayer systems are designated as the following. $M_{fcc}L_3$ represents stacking of face-centered-cubic (fcc) {111} close-packed layers of Al and Ti with three layers per film. $M_{hcp}L_6$ represents stacking of hexagonal close-packed (hcp) {0001} layers of Al and Ti with six layers per film. $M_{100}L_{12}$ represents stacking of fcc {100} layers of Al and Ti with 12 layers per film. $M_{cp}L_{24}$ represents stacking of fcc close-packed layers of Al and hcp close-packed layers of Ti with 24 layers per film. M_{fcc}, M_{hcp}, M_{100} and M_{cp} are multilayers with coherent interfaces. M_{cpic} multilayers are similar to M_{cp} only with incommensurate interfaces. See Table 1 for nanolayer thin film information.

Table 2: Dimensions of Al-Ti multilayers and bulk Al and Ti structures at 300 K. V_{vor} represents the average Voronoi volume per atom. d_z denotes the average Voronoi thickness of a layer in each film. The strains are calculated relative to the constituent bulk structure of Al or Ti in the multilayers (e.g. in Mfcc system the bulk structures are fccAl and fccTi while in Mcp system they are fccAl and hcpTi). $\Delta V = V_{vor} - V$, where V denotes the average atomic volume in the constituent bulk structures.

	L_x (Å)	$\bar{d}_z^{Al}$ (Å)	$\bar{d}_z^{Ti}$ (Å)	V_{vor}^{Al} (Å^3)	V_{vor}^{Ti} (Å^3)	$\epsilon_x^{Al}(\%)$	$\epsilon_x^{Ti}(\%)$	$\bar{\epsilon}_z^{Al}(\%)$	$\bar{\epsilon}_z^{Ti}(\%)$	$\frac{\Delta V}{V}^{Al}(\%)$	$\frac{\Delta V}{V}^{Ti}(\%)$
M100L3	24×4.218	1.825	1.983	16.244	17.645	3.65	1.52	-10.25	-4.55	-3.60	-1.60
M100L6	24×4.142	1.950	2.061	16.730	17.686	1.79	-0.30	-4.19	-0.80	-0.71	-1.38
M100L12	24×4.129	1.986	2.078	16.925	17.707	1.45	-0.63	-2.40	0.01	0.45	-1.26
M100L24	24×4.120	2.053	2.102	17.430	17.844	1.25	-0.83	0.91	1.18	3.45	-0.49
MfccL3	32×2.906	2.287	2.376	16.742	17.393	1.00	-1.08	-2.65	-0.94	-0.64	-3.01
MfccL6	32×2.913	2.304	2.393	16.933	17.587	1.23	-0.85	-1.95	-0.26	0.49	-1.93
MfccL12	32×2.914	2.323	2.395	17.084	17.613	1.26	-0.82	-1.14	-0.18	1.39	-1.78
MfccL24	32×2.919	2.279	2.425	16.829	17.900	1.45	-0.64	-2.98	1.07	-0.12	-0.18
MhcpL3	32×2.896	2.359	2.398	17.144	17.422	1.68	-1.98	-3.91	1.81	-0.66	-2.16
MhcpL6	32×2.904	2.388	2.390	17.445	17463	1.97	-1.70	-2.75	1.51	-1.08	-1.93
MhcpL12	32×2.909	2.403	2.382	17.612	17.458	2.14	-1.54	-2.12	1.16	2.05	-1.96
MhcpL24	32×2.918	2.343	2.387	17.281	17.605	2.46	-1.22	-4.57	1.36	0.13	-1.13
McpL3	32×2.906	2.304	2.375	16.841	17.362	0.97	-1.66	-1.95	0.85	-0.05	-2.49
McpL6	32×2.917	2.305	2.375	16.983	17.496	1.35	-1.29	-1.89	0.84	0.79	-1.74
McpL12	32×2.922	2.318	2.368	17.136	17.508	1.54	-1.11	-1.33	0.57	1.70	-1.68
McpL24	32×2.925	2.294	2.386	16.999	17.682	1.64	-1.01	-2.37	1.32	0.88	-0.70

Mcpic	L_1	L_2	$\bar{d}_z^{Al}$	$\bar{d}_z^{Ti}$	V_{vor}^{Al}	V_{vor}^{Ti}	$\epsilon_1^{Al}(\%)$	$\epsilon_1^{Ti}(\%)$	$\epsilon_2^{Al}(\%)$	$\epsilon_2^{Ti}(\%)$	$\bar{\epsilon}_z^{Al}(\%)$	$\bar{\epsilon}_z^{Ti}(\%)$	$\frac{\Delta V}{V}^{Al}(\%)$	$\frac{\Delta V}{V}^{Ti}(\%)$
L3	97.055	94.608	2.332	2.370	16.455	17.770	-0.80	-0.46	-0.36	0.05	-0.74	0.65	-2.34	-0.20
L6	97.332	94.666	2.347	2.362	16.644	17.801	-0.52	-0.18	-0.30	0.11	-0.13	0.30	-1.22	-0.03
L12	97.473	94.710	2.355	2.357	16.753	17.820	-0.37	-0.03	-0.25	0.16	0.21	0.10	-0.57	-0.08
L24	97.510	94.717	2.355	2.356	16.772	17.835	-0.34	0.01	-0.24	0.17	0.21	0.06	-0.46	0.16
	fccAl	fccTi	hcpAl	hcpTi										
a(Å)	4.069	4.155	2.848	2.955										
c/a	1.000	1.000	1.724	1.594										

All of the displacement cascade simulations were initiated with a 1.5 keV PKA. The evolution of damage production (the number of Frenkel pairs) from the simulations was plotted in Figure 13a. The plotted quantities are the average values from the 20 runs. Different colors represent different systems. In each multilayer system, different film thickness was plotted with a different symbol, namely L_3 (triangle), L_6 (square), L_{12} (diamond) and L_{24} (circle). The number of produced Frenkel pairs rises quickly within sub-pico second timespan and reaches maximum N_{max} at approximately 0.3 ps. Following this stage, most of the displaced atoms quickly recover to the lattice sites within several pico seconds. Ti (black curve) exhibits the fastest recovery rate, followed by M_{fcc}, (M_{cpic}, M_{cp}, M_{100}), M_{hcp}, and finally Al. Figure 14a shows the N_{max} for all the systems. It appears that the recovery rate is correlated with N_{max}, i.e. the rate increases as N increases. Since one may think of N_{max} as a measure of the size of the damage region, the correlation may be simply a consequence of a fact that it takes longer for atoms to recover a larger damage volume.

One cause of the defect asymmetry is the defect production rate, which has at its root the differences in energy absorption in each layer due to collisional processes, as well as the different thresholds. Figure 15 shows the ratio between energy absorption ratio, χ, in the Ti and Al layers as a function of layer period.

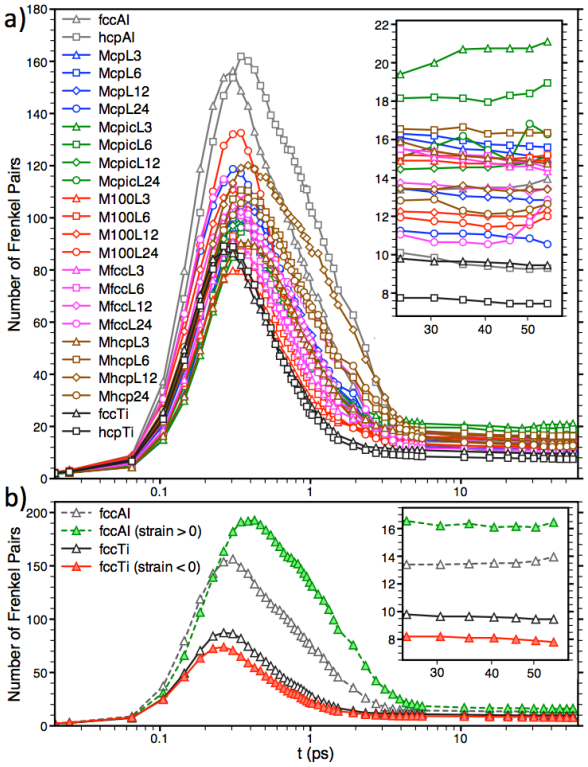

Figure 13. Shown in (a) is the evolution of damage production as a function of time in ps for the various systems showing that the defect production asymptotes to a final value after about 55 ps for each layered system and that there is a very similar evolutionary history independent of layer stacking sequence. In (b) is shown the same data for bulk Al and Ti including strained bulk lattices.

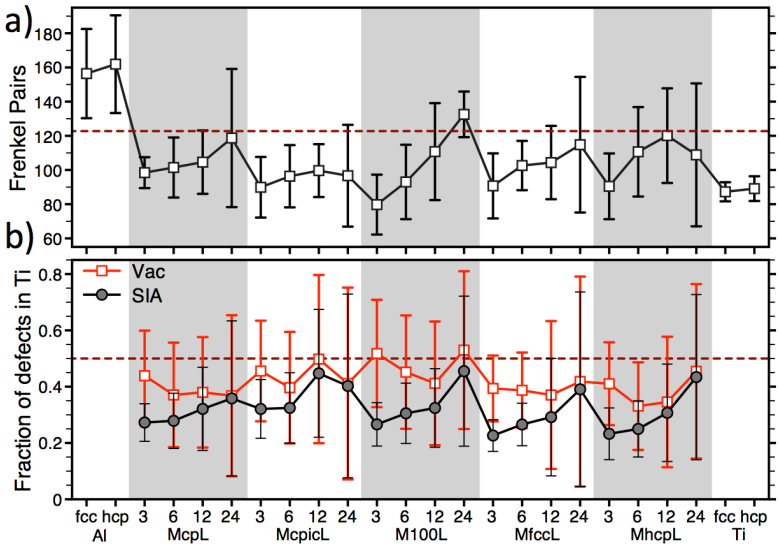

Figure 14. The total number of Frenkel pairs as a function of layer type and layer period at the peak of the damage production near 0.3 ps. Shown in (a) is the trend as a function of layer period (thickness) indicating that thinner layers accumulate fewer defects as expected. In (b) is shown the defect partitioning the depends on the layer elemental type. Here the Ti layer is storing less than half the total defects implying that the Al layer is storing more than half.

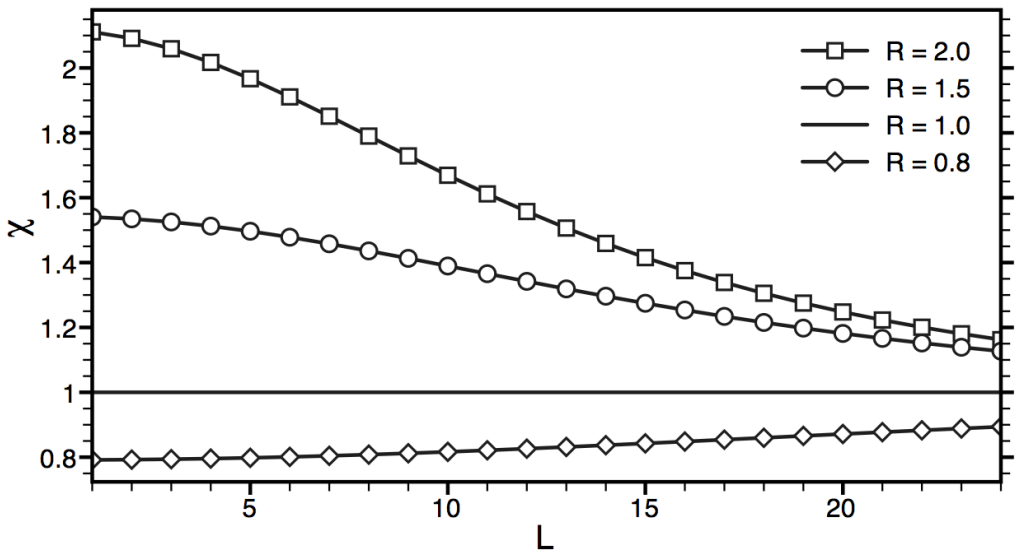

Figure 15. The ratio of deposited energy χ for various values of R equal to f_{Ti}/f_{Al}, or the energy deposited in Ti to the energy deposited in Al. As the layers become thinner, χ increases indicating that the Ti layer is dominating the stopping and energy deposition.

We realize that in multilayers, the absorption coefficient for each layer varies even within the same film due to the different atomic environments and strain field experienced by each layer. Moreover, determining the value of f_{Ti} and f_{Al} of each layer is not straightforward. However, we believe that the underlying physics captured in the model sufficiently describes the observed trend of N_{max} vs. L, at least qualitatively. In other words, in a multilayer system, even though the proportion of the constituent materials is kept the same, the response of the system can be driven closer to the more dominant materials by reducing the thickness of each film. In this case, N_{max} in L3 is the closest to that in Ti.

The number of surviving defects at the end of simulations (N_{end}) was plotted in Figure 16a. The values for the bulk structures are $N_{end,fccAl} \sim 14$ and $N_{end,hcpTi} \sim 7$. The dashed line at 10.5 marks the average bulk value $N_{end,bulk} = (N_{end,fccAl} + N_{end,hcpTi})/2$. In all of the multilayers, even though $N_{max} < N_{max,bulk}$, the surviving number of defects is larger than $N_{end,bulk}$. This indicates that the vacancy-interstitial recombination in these multilayers is suppressed. The defect spatial distribution, defect cluster morphology as well as the strain field may contribute in altering the defect recombination process.

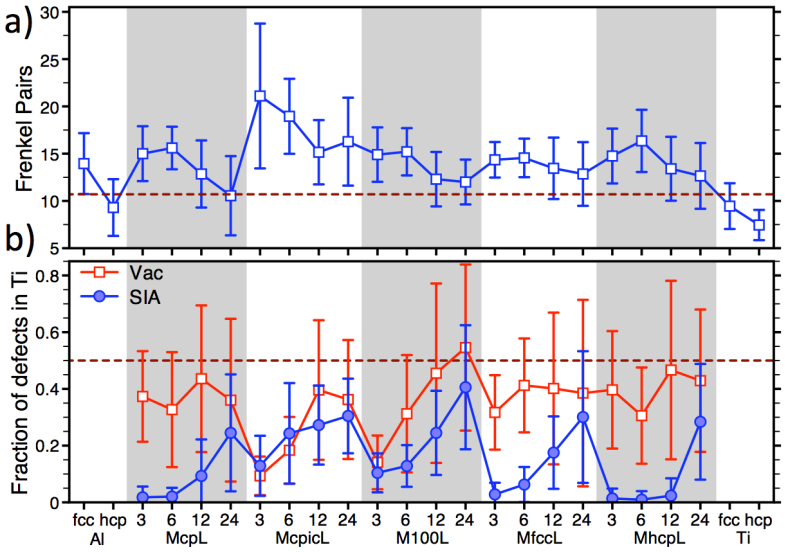

Figure 16. The total number of Frenkel pairs as a function of layer type and layer period at the end of the damage production at 55 ps. Shown in (a) is the trend as a function of layer period (thickness) indicating that layer thickness is not playing the same role as for the peak damage regime in Fig. 14. In (b) is shown the defect partitioning that depends on the layer elemental type. Here the Ti layer is storing less than half the total defects implying that the Al layer is storing more than half. The difference between vacancies and interstitials is quite dramatic. Here the layer thickness effects do emerge.

To better understand how defects are distributed in the multilayer, we present the analysis of defect distribution at the maximum damage production regime as well as at the end of the simulations. The defect distribution near the maximum damage production is presented in Figure 14b. The plotted quantities are the fractions of vacancies (square marks) and self-interstitial atoms SIAs (circles) in the Ti film. The plot shows that there are fewer vacancies in Ti film than in Al film. This is understood from the larger E_t of Ti film. There are also fewer interstitials in the Ti film than in Al film. In fact, in the Ti film the number of interstitials is even smaller than the number of vacancies. This indicates that there is an imbalance flux of displaced atoms from Ti film to Al film. The degree of imbalance systematically increases as the film thickness decreases (the number of interfaces is increased). Near the interface, we observed that displacing a Ti atom from Ti film to the Al region is energetically favorable than the opposite process. This was caused by the fact that it is easier for the heavier Ti atom to displace a lighter Al atom whose E_t is also smaller than otherwise. Hence, the interface has induced a preferential drift of SIAs from the Ti to the Al film causing imbalance population of SIAs relative to vacancies in a particular film. We refer this phenomenon as "partitioning" effect. It is expected then that the partitioning effect inhibits the defect recombination in multilayers.

Figure 16b shows the vacancy-SIA fraction imbalance in the Ti film at the end of the simulations. Unlike the imbalance curve near the maximum damage production (Fig. 14b), the imbalance at the end of simulation shows two different characteristics depending on the multilayer system. Firstly, in Mcp, Mfcc and Mhcp, the imbalance is still evident, in fact it is more pronounced due to the much smaller fraction of SIAs that survives in the Ti film. As the result of the partitioning effect, in the Ti film the number of vacancies is more than what is needed for the recombination, while in the Al film there are more SIAs than the available vacancies to recombine. The second characteristic of the imbalance curve is observed in Mcpic and M100. In the M100, even though the fraction of vacancies in the Ti film is still larger than the fraction of SIAs, the difference diminishes towards L3. In the Mcpic, the fraction of vacancies in the Ti film

becomes comparable to that of SIAs. In this case, it appears that a portion of SIAs in the Al film recombine with vacancies in the Ti film particularly those at the interface, mostly during the early stages of recovery. The different characteristic of fraction imbalance at the end of simulation between Mcp-Mfcc-Mhcp and M100-Mcpip may be related to the strain in the film. From Table 1, in the first group of multilayers, Ti film is compressed in both basal directions ($\varepsilon_{x,Ti} = \varepsilon_{y,Ti} < 0$) and the compressive strain increases as film thickness decreases. The opposite case occurs in the second group of multilayers: in the M100 $\varepsilon_{x,Ti}$ gradually becomes > 0 at L3, while in Mcpic even though $\varepsilon_{1,Ti}$ is slightly < 0, $\varepsilon_{2,Ti}$ is > 0. In addition, unlike in all other systems in which Al film is under tensile, Al film in the Mcpic is slightly compressed. We believe that the reduction of the exclusivity of compressive strain in the Ti film (on one hand) and tensile strain in the Al film (on the other hand) in the M100 and Mcpic multilayers plays a role in reducing the vacancy-SIA fraction imbalance by allowing a portion of the SIAs in the Al film to recombine with vacancies in the Ti film near the interface during the recovery process.

Besides the defect distribution (partitioning effect), the different strain levels that are experienced by each layer in the film can significantly affect defect migration. The SIAs may either preferentially migrate to the interface or to the middle of the film away from the interface. To study defect migration, the number of surviving vacancies and interstitials at the end of the simulations in each layer along the stacking is calculated. Figure 17 shows the result for L6 in each multilayer (other film thicknesses show similar distribution). In Fig. 17 the vacancies are plotted with hollow marks while interstitials are presented as filled marks. In all systems, the multilayer starts with Al film at the bottom (gray) followed by Ti film (blue). The stacking sequence is included in the plot for clarity. As has been discussed, the majority of the defects are found in the Al films. Fig. 17 also reveals that in all multilayers except the M100, the SIAs are preferentially found at the interface layer in the Al film. Meanwhile, for M100, the interstitials preferentially migrate to the middle of the Al films. The interstitials in Ti film in M100 also migrate to the middle of the Ti film even though the number is much smaller than in Al films.

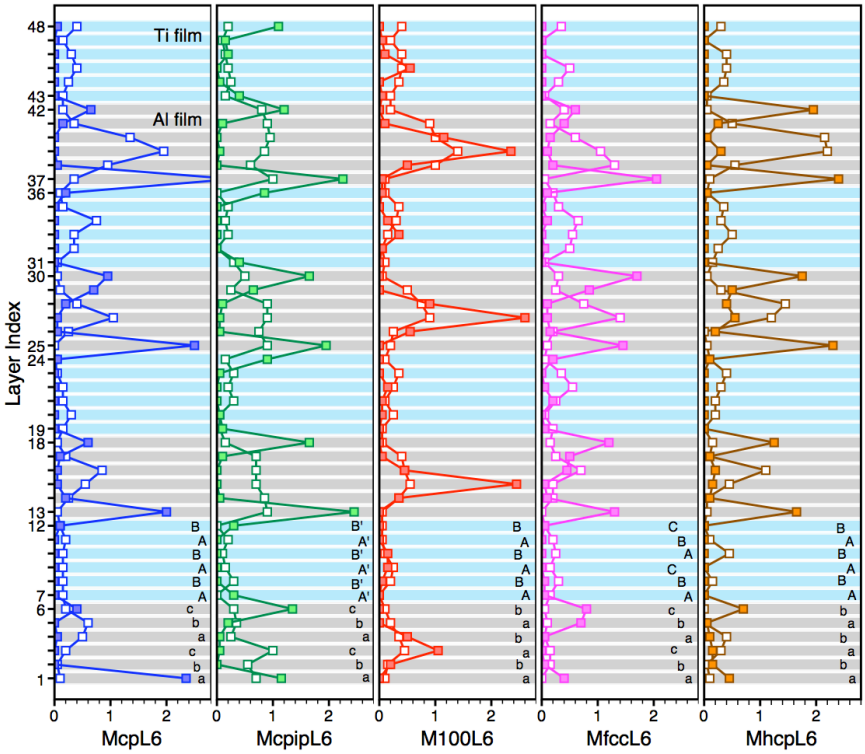

Figure 17. Distribution of vacancies (hollow) and interstitials (filled) at the simulation end (55 ps).

To understand why the interstitials in the Al films migrate to the middle of the film in M100 while they migrate to the interface layer in all the close-packed multilayers, formation energies of dumbbells in McpL6 (to represent the multilayers of close-packed layers) and M100L6 were calculated. A single interstitial was added to the system and the atoms were relaxed via energy minimization. The results are presented in Table 2.

Table 2: Dumbbell configuration and formation energy E_f in McpL6 and M100L6 multilayer. Layer indexing in the stacking starts from bottom to top: Al-1→Al-6→Ti-7→Ti- 12. The * indicates that a dumbbell stabilizes in a different layer than its initial position during relaxation. All Miller indices are with respect to a cubic system.

Layer	dumbbell	E_f (eV)	bond (Å)
McpL6			
Al-1	$[11\bar{2}]$ (Al-Al)	1.27	2.27
Al-2	$[11\bar{2}]$ (Al-Al)	1.68	2.26
Al-3	[100] (Al-Al)	1.82	2.35
Al-4	[100] (Al-Al)	1.84	2.35
Al-5	$[11\bar{2}]$ (Al-Al)	1.82	2.26
Al-6	$[10\bar{1}]$ (Al-Al)	1.64	2.27
Ti-7*	$[10\bar{1}]$ (Al-Al) in Al-6	1.07	2.27
Ti-8	$[11\bar{2}]$ (Ti-Ti)	3.31	2.26
Ti-9	$[11\bar{2}]$ (Ti-Ti)	3.28	2.32
Ti-10	$[11\bar{2}]$ (Ti-Ti)	3.27	2.26
Ti-11*	$[11\bar{2}]$ (Al-Al) in Al-13	0.59	2.26
Ti-12*	$[11\bar{2}]$ (Al-Al) in Al-13	0.59	2.26
M100L6			
Al-1*	[001] (Al-Al) in Al-2	2.03	2.29
Al-2*	[001] (Al-Al) in Al-3	1.84	2.34
Al-3	[100] (Al-Al)	1.78	2.36
Ti-7*	[001] (Ti-Ti) in Ti-8	3.04	2.32
Ti-8*	[001] (Ti-Ti) in Ti-9	2.91	2.33
Ti-9	[100] (Ti-Ti)	2.88	2.34

These results have great significance in understanding the He implantation data. Figure 9a shows the cross-section image of Al-Ti multilayer sample with thickness of 5 nm per film (~21 layers) obtained with underfocused TEM. The image was taken after He irradiation with dose 10^{16} atoms/cm^2 at room temperature. In this image, Ti films appear darker than Al due to atomic number contrast. In the Ti films, bright spots can be seen that represent He bubbles. The diameter of the bubbles is ~1 nm. This result is intriguing for a reason that due to a lower displacement threshold energy of Al compared to Ti, the nucleation of small bubbles via a kickout mechanism (a cluster of He atoms displacing a host atom from its lattice site) would be expected to occur in Al films. As a reference, to create a 1-nm bubble, ~56 Ti atoms or ~59 Al atoms would need to be displaced.

The fact that the bubbles are found in the Ti films suggests that the distribution of He atoms during the irradiation plays a major role in determining the morphology and location of the bubbles. It is possible that the larger stopping power of Ti films has caused the He atoms to be stopped and contained in the Ti films more effectively than in Al films. In this scenario, the necessary space needed for the bubbles is created not via kickout mechanism but rather during collision cascade itself. In this stopping process, the impinged Ti atoms may remain in the Ti film or displaced to the Al film. If the impinged Ti atoms can be displaced to the Al film, this process will greatly favor the creation of the necessary excess volume for the He atoms to form small bubbles in Ti films. The defect imbalance that is observed in the simulations provides a clear proof that displacing Ti atoms from Ti film to Al film is indeed easier than vice versa.

In Figure 9a, the He bubbles are arranged in a row with a somewhat regular spacing between the bubbles. More importantly, the bubbles are located near the interface towards the Al film below the Ti film where they reside, i.e. the location of the bubbles is biased towards the direction of the irradiation. This provides another clue that the small bubbles formation in Ti film is associated with the preferential flux of SIAs from Ti films to Al films during the irradiation as described above.

In the Cu/Nb system, even though it is an immiscible system, we observe similar results from the higher He dose images from the paper by Hattar [11] where the He bubbles in the Cu layers have grown much larger than those in the Nb layers. This is indicative of the defect partitioning operating in this system as well. See Figure 18, which is Fig. 3 from the Hattar paper.

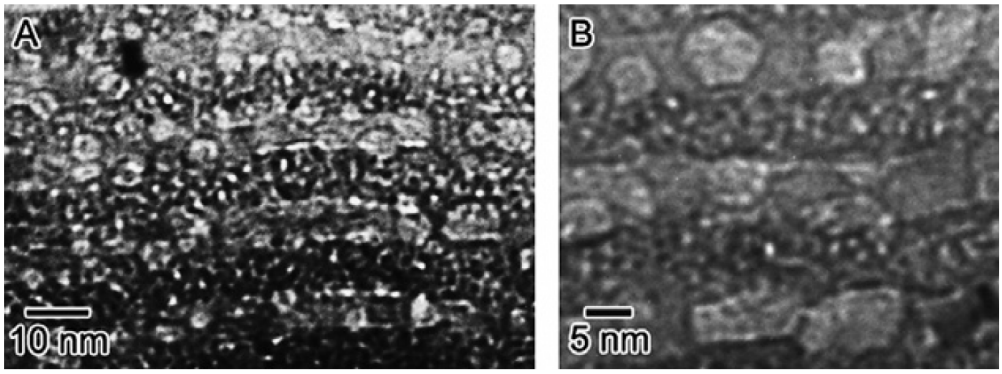

Figure 3. (A) He bubbles in Cu–Nb with 5 nm as-deposited layer thicknesses. Only 1–2 nm diameter bubbles are seen in Nb, while larger bubbles with a broader size distribution are present in Cu layers. (B) The maximum bubble size in Cu is limited by the Cu layer thickness.

Figure 18. Fig. 3 from the paper by Hattar et al. [11] showing large He bubbles in the Cu layers and smaller He bubbles in the Nb layers. This type of defect partitioning is unfavorable for the survival of these nanolayered materials in radiation fields.

6. Conclusion

This work has revealed several important properties of Al/Ti nanolayers in response to radiation damage. During maximum damage production initiated with 1.5-keV PKA, asymmetry in the point defects creation between the two dissimilar materials Al or Ti is observed with ~60% of vacancies are created in Al films while ~70% of interstitials are created in Al films. The excess interstitials in the Al films is a direct consequence of the preferential flux of displaced atoms in this nanolayered system. He irradiation experiments at a low dose of 10^{16} atoms/cm^2 and at room temperature were performed to investigate the interface effects on radiation damage. The experimental data shows a formation of ~1-nm diameter bubbles in the Ti films near the interface. The results from the simulations and experiments seem to suggest that the bubbles formation is associated with the preferential flux of SIAs during the irradiation in that the He atoms impinge on the Ti films and displace the Ti atoms into the Al films. This is further supported by the location of the bubbles being near the interface and biased towards the direction of the irradiation.

In all of the interface models in this study, the number of Frenkel pairs created during maximum damage production is smaller than the bulk average of the constituent materials. This discrepancy is amplified towards thinner films. This is understood using a phenomenological model that Ti exhibits a larger stopping power than Al and that the fraction of energy deposited

in Ti films increases as the films are made thinner. On the other hand, the number of surviving Frenkel pairs at the end of simulations is larger than the bulk average. The difficulty for anti-defect recombination is caused by defect partitioning in which in Al films there are too many interstitials than the available vacancies while the opposite applies in Ti films. This defect partitioning increases with the increasing number of interfaces (thinner films) resulting in more than 90% of surviving interstitials are located in the Al films for nanolayers with <= 6 layers per film.

This research has reached some surprising conclusions that were unexpected at the beginning of the research. We were unaware of this defect-partitioning problem until we performed our MD simulations of damage in the Al/Ti nanolayered system as reported here. This is surprising and, unfortunately, bad news for the use of these dissimilar materials in radiation fields to high damage doses. The hope for a radiation damage tolerant material based on nanolayered materials is not well founded based on our results. Perhaps more important than complex interfaces and immiscible material system is the need for a layered system that has similar damage thresholds and energy absorption rates. This would argue for materials with nearly equal atomic masses and similar crystal structures. Such research could be fruitful.

What opportunities for training and professional development has the project provided?

Graduate students, undergrads or post-docs supported.

- Dr. Arun Devaraj joined PNNL on May 17th. He is a materials scientist from Univ. of North Texas. He is full-time on this project.
    - **Post-Doc RA Dr. Arun Devaraj promoted to Scientist 3 at PNNL/EMSL.**
- Dr. Wahyu Setyawan joined PNNL on May 1. He is a computational materials scientist from Duke University. He is quarter-time on this project.
    - **Post-Doc RA Dr. Wahyu Setyawan promoted to Scientist 3 at PNNL.**
- Rama Vemuri (PhD Student intern from Univ. of Texas El Paso)
    - Al-Ti Multilayer Films: Synthesis, Characterization, and Radiation Damage Processes.
    - **PhD Student Rama Vemuri received PhD in 2014 and converted to Post-Doc RA.**
- Shravan Katakam (PhD Student intern from Univ. of North Texas)
    - Alternate Sponsored Fellow, Summer 2012 only.
- Matthew Gerboth (BSc Student intern from Washington State Univ.)
    - SULI Summer Intern with Paper – Radiation Damage in Al/Ti Multilayers.
    - Obtained BSc in December 2012. Returned to PNNL as Post-bac intern January 2013.
    - **Post-bachelor student Matt Gerboth accepted into PhD program at Vanderbilt Univ. studying radiation damage in scintillator materials.**
- Maria Quintero (high school student intern 2011-2012)
- Quinten Dicken (high school student intern 2012-2013)

How have the results been disseminated to communities of interest?

- **2 publications**
    - Setyawan, W., M. Gerboth, Y. Bo, C.H. Henager, A. Devaraj, V.R.S.R. Vemuri, S. Thevuthasan, and V. Shutthanandan, "Asymmetry of radiation damage properties in Al-Ti nanolayers," Journal of Nuclear Materials, 2014, 445(1-3), 261-71.
    - Gerboth, M., W. Setyawan, and C.H. Henager, Jr., "Displacement threshold energy and recovery in an Al-Ti nanolayered system with intrinsic point defect partitioning," Computational Materials Science, 2014, 85, 269-79.
- **2 invited talks, 4 contributed talks, 2 posters in conferences**
- **1 extended abstract to M&M2012:** V. Shutthanandan, A. Devaraj, R. S. Vemuri, C. M. Wang, T. Varga, CH. Henager Jr., S. Thevuthasan, "Site specific He ion irradiation damage studies in nanolayered thin films by cross-coupling Helium Ion Microscopy with TEM and APT", **Extended abstract, Microscopy and Microanalysis 2012.**
- **EMSL user proposal renewed**
- **INVITED TALK**: S. Thevuthasan, V. Shutthanandan, A. Devaraj, R. Vemuri, T. C. Kaspar, C.M. Wang, T. Varga, R. J. Kurtz and C. H. Henager, Jr. *"Radiation Effects at Metal/Oxide and Metal/Metal Interfaces"*, **MRS 2012, San Francisco, CA.**
- **INVITED TALK:** A. Devaraj, R. Colby, V. Shutthanandan, S. Thevuthasan, "*Three-dimensional characterization of Heavy ion irradiation effects using Atom Probe Tomography"*, **CAARI 2012, Fort Worth, TX.**
- A. Devaraj, R.S. Vemuri, T. Varga, V. Shutthanandan, S.V.N.T. Kuchibhatla, M. Engelhard, P. Nachimuthu, C. Henager, C.M. Wang, S. Thevuthasan. *"Three dimensional characterization of chemical intermixing in nano-layered radiation shielding metallic thin films",* **TMS 2012, Orlando, FL**.
- R.S. Vemuri, A. Devaraj, T. Varga, V. Shutthanandan, M. Engelhard, C. Henagar, C.M. Wang, S. Thevuthasan, C.V. Ramana. *"Heavy ion irradiation effects on Al/Ti multilayers"* **AVS 2011, Nashville, TN.**
- A. Devaraj, R.S. Vemuri, T. Varga, V. Shutthanandan, S. V. N. T. Kuchibhatla, M. Engelhard, C. H. Henagar Jr., C.M. Wang, S. Thevuthasan, *"Three dimensional characterization of chemical intermixing in nano-layered radiation shielding metallic thin films",* **MRS 2011, Boston, MA**.
- **POSTER:** A. Devaraj, R.S. Vemuri, T. Varga, V. Shutthanandan, S. V. N. T. Kuchibhatla, M. Engelhard, C. H. Henagar Jr., C.M. Wang, S. Thevuthasan, "Heavy ion effects on multilayer thin films", **MRS 2012, San Francisco, CA.**
- **POSTER:** R.S. Vemuri, A. Devaraj, T. Varga, V. Shutthanandan, S.V.N.T. Kuchibhatla, M. Engelhard, P. Nachimuthu, C. Henager, C.M. Wang, S. Thevuthasan and C.V. Ramana, "Heavy ion irradiation effects on Ti/Al multilayer thin films", **PNWAVS 2011, Portland, OR.**

7. References

1. Hochbauer, T., A. Misra, K. Hattar, and R.G. Hoagland, "Influence of interfaces on the storage of ion-implanted He in multilayered metallic composites," Journal of Applied Physics, 2005, 98(12), 1-7.
2. Demkowicz, M.J., Y.Q. Wang, R.G. Hoagland, and O. Anderoglu, "Mechanisms of He escape during implantation in CuNb multilayer composites," Nuclear Instruments and Methods in Physics Research, Section B: Beam Interactions with Materials and Atoms, 2007, 261(Compendex), 524-528.
3. Zhang, X., N. Li, O. Anderoglu, H. Wang, J.G. Swadener, T. Hochbauer, A. Misra, and R.G. Hoagland, "Nanostructured Cu/Nb multilayers subjected to helium ion-irradiation," Nuclear Instruments and Methods in Physics Research, Section B: Beam Interactions with Materials and Atoms, 2007, 261(1-2 SPEC. ISS.), 1129-1132.
4. Zhernenkov, M., M.S. Jablin, A. Misra, M. Nastasi, W. Yongqiang, M.J. Demkowicz, J.K. Baldwin, and J. Majewski, "Trapping of implanted He at Cu/Nb interfaces measured by neutron reflectometry," Applied Physics Letters, 2011, 98(24), 241913 (3 pp.).
5. Demkowicz, M.J., D. Bhattacharyya, I. Usov, Y.Q. Wang, M. Nastasi, and A. Misra, "The effect of excess atomic volume on He bubble formation at fcc-bcc interfaces," Applied Physics Letters, 2010, 97(16).
6. Bhattacharyya, D., M.J. Demkowicz, Y.Q. Wang, R.E. Baumer, M. Nastasi, and A. Misra, "A Transmission Electron Microscopy Study of the Effect of Interfaces on Bubble Formation in He-implanted Cu-Nb Multilayers," Microscopy and Microanalysis, 2012, 18(1), 152-61.
7. Demkowicz, M.J., A. Misra, and A. Caro, "The role of interface structure in controlling high helium concentrations," Current Opinion in Solid State and Materials Science, 2012, 16(3), 101-108.
8. McPhie, M.G., L. Capolungo, A.Y. Dunn, and M. Cherkaoui, "Interfacial trapping mechanism of He in Cu-Nb multilayer materials," Journal of Nuclear Materials, 2013, 437(1-3), 222-228.
9. Kashinath, A., A. Misra, and M.J. Demkowicz, "Stable storage of helium in nanoscale platelets at semicoherent interfaces," Physical Review Letters, 2013, 110(8).
10. Li, N., M. Nastasi, and A. Misra, "Defect structures and hardening mechanisms in high dose helium ion implanted Cu and Cu/Nb multilayer thin films," International Journal of Plasticity, 2012, 32-33, 1-16.
11. Hattar, K., M.J. Demkowicz, A. Misra, I.M. Robertson, and R.G. Hoagland, "Arrest of He bubble growth in Cu-Nb multilayer nanocomposites," Scripta Materialia, 2008, 58(7), 541-544.
12. Fu, E.G., J. Carter, G. Swadener, A. Misra, L. Shao, H. Wang, and X. Zhang, "Size dependent enhancement of helium ion irradiation tolerance in sputtered Cu/V nanolaminates," Journal of Nuclear Materials, 2009, 385(Compendex), 629-632.
13. Li, N., J.J. Carter, A. Misra, L. Shao, H. Wang, and X. Zhang, "The influence of interfaces on the formation of bubbles in He-ion-irradiated Cu/Mo nanolayers," Philosophical Magazine Letters, 2011, 91(1), 19-29.
14. Wei, Q.M., Y.Q. Wang, M. Nastasi, and A. Misra, "Nucleation and growth of bubbles in He ion-implanted V/Ag multilayers," Philosophical Magazine, 2011, 91(4), 553-573.
15. Fu, E.G., H. Wang, J. Carter, L. Shao, Y.Q. Wang, and X. Zhang, "Fluence-dependent radiation damage in helium (He) ion-irradiated Cu/V multilayers," Philosophical Magazine, 2013, 93(8), 883-898.

16. Zope, R.R. and Y. Mishin, "Interatomic potentials for atomistic simulations of the Ti-Al system," Physical Review B (Condensed Matter and Materials Physics), 2003, 68(2), 24102-1.
17. Ziegler, J.F., J.P. Biersack, and U. Littmark, Stopping and range of ions in solids. 1985, New York, NY, USA: Pergamon Press. 321.
18. Demkowicz, M.J. and R.G. Hoagland, "Structure of Kurdjumov-Sachs interfaces in simulations of a copper-niobium bilayer," Journal of Nuclear Materials, 2008, 372(Compendex), 45-52.

Journal of Nuclear Materials 445 (2014) 261–271

Contents lists available at ScienceDirect

Journal of Nuclear Materials

journal homepage: www.elsevier.com/locate/jnucmat

Asymmetry of radiation damage properties in Al–Ti nanolayers

Wahyu Setyawan [a,*], Matthew Gerboth [a], Bo Yao [a], Charles H. Henager [a], Arun Devaraj [b], Venkata R.S.R. Vemuri [b], Suntharampillai Thevuthasan [b], Vaithiyalingam Shutthanandan [b]

[a] Pacific Northwest National Laboratory, Richland, WA 99354, USA
[b] Environmental Molecular Sciences Laboratory, Richland, WA 99354, USA

ARTICLE INFO

Article history:
Received 24 July 2013
Accepted 11 November 2013
Available online 23 November 2013

ABSTRACT

Molecular dynamics (MD) simulations were employed with empirical potentials to study the effects of multilayer interfaces and interface spacing in Al–Ti nanolayers. Several model interfaces derived from stacking of close-packed layers or face-centered cubic {100} layers were investigated. The simulations reveal significant and important asymmetries in defect production with ~60% of vacancies created in Al layers compared to Ti layers within the Al–Ti multilayer system. The asymmetry in the creation of interstitials is even more pronounced. The asymmetries cause an imbalance in the ratio of vacancies and interstitials in films of dissimilar materials leading to >90% of the surviving interstitials located in the Al layers. While in the close-packed nanolayers the interstitials migrate to the atomic layers adjacent to the interface of the Al layers, in the {100} nanolayers the interstitials migrate to the center of the Al layers and away from the interfaces. The degree of asymmetry and defect ratio imbalance increases as the layer spacing decreases in the multilayer films. Underlying physical processes are discussed including the interfacial strain fields and the individual elemental layer stopping power in nanolayered systems. In addition, experimental work was performed on low-dose (10^{16} atoms/cm^2) helium (He) irradiation on Al/Ti nanolayers (5 nm per film), resulting in He bubble formation ~1 nm in diameter in the Ti film near the interface. The correlation between the preferential flux of displaced atoms from Ti films to Al films during the defect production that is revealed in the simulations and the morphology and location of He bubbles from the experiments is discussed.

Published by Elsevier B.V.

1. Introduction

Radiation damage in solids from collision cascades formed during high-energy particle irradiation, ions or neutrons, is extremely costly and, perhaps, the single most complex and challenging technological problem facing nuclear material scientists, reactor designers, and regulatory agencies desiring long-lived engineering structures, low operational costs, and safety. The search for and development of materials with improved radiation damage tolerance requires a more or less complete understanding of defect production, transport, evolution, and recovery in complex alloy or composite systems that are undergoing irradiation and transitions far from equilibrium on picosecond time scales at the atomic level to decade-long microstructural and thermo-physical property changes as either structural or functional materials. These properties undergo unavoidable time-, temperature-, and fluence-dependent degradation and, usually, irreversible changes [1] such that replacement or costly mitigation is required to satisfy operational safety concerns at critical fluence levels. There is a strong scientific and technological interest in studying and developing radiation damage tolerant materials.

Structural materials can achieve radiation damage tolerance via two basic mechanisms. Some materials intrinsically have a damage tolerant crystal structure with high damage thresholds, such as SiC in the zinc-blende structure, or they possess a high tolerance for atomic disorder as evidenced by certain oxides, such as disordered fluorites [2]. Unfortunately, most metallic and structural alloys possess low damage tolerance from close-packed crystal structures that can accommodate a wide variety of low lying defect states and that have low damage thresholds. Thus, they do not possess intrinsic damage tolerance, although bcc materials are more damage tolerant compared to fcc or hcp structures [1].

The second basic mechanism relies on enhanced damage recovery mechanisms typically via increased recombination rates of radiation-induced defects at defect sinks within a material. These sink sites range from grain boundary denuded zones observed in many materials to engineered materials containing nano-spaced interfaces, including nano-featured ferritic alloys and nanolayered materials. The general concept of point defect recombination at internal interfaces is not a new idea but has achieved recent significance from work with oxide dispersion strengthened (ODS) alloys [3–8], nano-featured alloys [9,10], and nano-layered composites

* Corresponding author. Tel.: +1 5093717692.
E-mail address: wahyu.setyawan@pnnl.gov (W. Setyawan).

0022-3115/$ - see front matter Published by Elsevier B.V.
http://dx.doi.org/10.1016/j.jnucmat.2013.11.012

[11–13] specifically designed to achieve high strength and enhanced defect recombination at closely spaced sinks for vacancies and self-interstitials. Capture and immobilization of helium (He) is also of keen interest for fusion reactor materials where He can be produced at levels approaching a few atomic percent [14–18].

Specifically, nanolayered materials based on dissimilar materials arranged in closely spaced layered structures with high interfacial areal fractions are considered developmental radiation tolerant materials. The specific details of the damage tolerance are still being studied and evaluated but it is considered that enhanced defect recombination at the dissimilar interfaces is occurring that reduces the overall damage accumulation relative to bulk materials. However, some specific trends are noted and discussed in the literature, namely, that immiscible systems behave differently compared to miscible systems under irradiation [19]. Miscible systems, including Al–Ti reported here, intermix under irradiation and would not be expected to demonstrate radiation damage tolerance at high doses. Immiscible systems are stable against mixing and do demonstrate enhanced radiation damage tolerance to some level of damage [19]. With regard to mixing of layered materials, but not specifically nanolayered films, there are phenomenological models built on the assumption that the mixing occurs via interdiffusion during high-energy collision cascades at low temperatures where the ion beam supplies sufficient energy that a locally melted region develops (thermal spike region) and phase transitions are possible [20]. These models and the thermodynamics of mixing can partly explain the improved damage tolerance of the immiscible systems compared to miscible ones.

However, many collisions are lower in energy than considered for the interdiffusion mixing models and in this regime a systematic study of nanolayered materials and their response to radiation damage has been lacking. At lower energies we can partly avoid the complications of ion beam mixing and study more carefully the effects of displacement damage. In this respect we find that there has been a lack of theoretical studies in this regime and this paper focuses on this aspect of the problem for a specific layered system that can be arranged in atomic models in a wide variety of stable structures, namely, the Al–Ti system. We also include some preliminary He-ion implantation studies of sputtered nanolayered Al–Ti films that demonstrate agreement with the theoretical models studied here.

The use of low energy He ion implantation to study ion beam mixing and radiation damage in nanolayered thin films is useful since He damage rates are reduced compared to heavy ions, the ranges are appropriate for thin films, and the effects of He accumulation are relatively easily observed compared to point defect clustering as a measure of radiation damage. It is understood that He bubble formation proceeds from vacancy (V) accumulation and He–V binding. Thus, observing He bubbles is a surrogate for observing V clustering in these thin film materials. Höchbauer et al. [21] were the first to study He accumulation as bubbles in Cu–Nb nanolayered materials. They observed preferential He bubble formation at Cu–Nb interfaces and along columnar grain boundaries following 33 keV He implantation. Demkowicz et al. [22] concluded that He also accumulates along Cu–Nb interfaces and that these interfaces act as fast diffusing pathways for He escape during annealing.

Zhang et al. [23] observed that He bubbles were not resolvable in Cu–Nb 2.5-nm layered foils, whereas identical 33 keV He implantation produced TEM visible bubbles in pure Cu, pure Nb, and Cu–Nb 100-nm layered materials. This was assumed to be evidence that Cu–Nb 2.5-nm layered materials exhibited enhanced recombination of radiation-induced point defects and, thus, much smaller He bubbles, less than about 1 nm in diameter. Zhernenkov et al. used neutron reflectometry to study He locations in implanted Cu–Nb foils and concluded that He was likely being stored as interstitial He in the dissimilar interfaces until a critical concentration was reached, after which He bubbles were formed [18]. Perhaps the best evidence comes from ^{3}He implantations and using nuclear reaction analysis (NRA) to study He concentrations as a function of implantation depth together with TEM to determine He concentrations where He bubbles form [24]. Similar conclusions were reached by Bhattacharyya et al. using TEM and NRA to study ^{3}He-implanted Cu–Nb foils [25]. Interface structure appears to play a critical role in the amount of He that can be stored before bubbles form [17]. Recent MD studies are consistent with this understanding and demonstrate atomic storage mechanisms for He in certain interfaces [16,26].

However, once a critical concentration of He is reached then He bubbles can nucleate and grow in these layered materials just as in bulk metals. A key difference, though, is that He bubble morphologies and locations vary from layer to layer and, above a certain dose, appear to depend on some intrinsic property of the layer material rather than the interfaces [27]. Hattar et al. [28] observed He bubbles in both the Cu and Nb layers of a Cu–Nb 5 to 6-nm layered foil after high doses of 33 keV He ion implantation at 763 K. However, He bubbles in the Cu layers spanned the thickness of the entire layer and were approximately 5–6 nm in diameter, whereas He bubbles in the Nb layers were about 1–2 nm in diameter. Similar observations of He bubble suppression compared to bulk or 100-nm layered materials are observed in Cu–V nanolayered foils [29] and in Cu–Mo nanolayered foils [30], where a slight size difference between He bubbles in Cu layers (larger) compared to Mo layers was noted. Wei et al. [31] observed bubble size differences in Ag–V nanolayered materials somewhere between the Cu–Nb size differences and those observed for Cu–V, with the larger bubbles contained in Ag layers. Fu et al. nicely summarize dose effects in Cu–V nanolayered systems and discuss He effects, radiation hardening, and both mixing and demixing effects observed in other systems [19].

One trend that appears to be consistent in these nanolayered studies is the observation that a certain level of asymmetry develops with regard to He bubble morphologies at increased He doses. Bubble sizes are non-uniform after a certain dose and the evidence is not clear that this asymmetry does not develop earlier in the radiation damage regime. Helium storage at dissimilar interfaces does not destroy the symmetry of the system, although, asymmetric swelling amounts are often noted [18,27–29], along with asymmetric He bubble sizes [28]. These become serious issues in dealing with nanolayered failure mechanisms from radiation damage, perhaps from delamination or other mechanical failures due to differential responses.

One shortcoming in the current literature and that is addressed in this research is the lack of understanding of point defects in nanolayered systems at low energies where ion beam mixing and demixing effects do not occur readily. In particular, displacement thresholds have not been studied for any of these layered systems to help understand or predict if some part of the response asymmetry may be due to displacement threshold effects. There is no reason to expect that defect generation or fates are symmetric within nanolayered materials made up of dissimilar metals. Under asymmetric defect generation the ability of the system to avoid damage accumulation via enhanced recombination may be compromised. One layer may accumulate an excess of one kind of point defect or defect cluster over time. The differential He bubble size observed in Cu–Nb suggests that this type of damage cannot be overlooked or ignored. An analogy to the Kirkendall effect and the resultant porosity and interface motion during interdiffusion of binary diffusion couples may be helpful.

This study performs a series of MD simulations in the Al–Ti system, which is one that has not been studied in terms of radiation damage response. The choice of this system was motivated by

the availability of a high-quality EAM potentials and by the flexibility of this system, although it is extremely reactive and miscible, to adopt a variety of possible interfaces, namely fcc–fcc at small size scales and fcc–hcp at larger size scales. In addition, this system is readily synthesized using magnetron sputtering. In a separate publication we set out a method and data for displacement thresholds for the Al–Ti nanolayered system and see systematic differences between computed thresholds for bulk metals and nanolayered metals. We make use of this information here but the research reported here studies the radiation response of the Al–Ti system arranged in a variety of possible structures. Finally, we have some preliminary data on He-implanted Al–Ti layers using low energy He ions using a He ion microscope and with characterization in cross-section using FIB and TEM.

2. Methods

2.1. Computational details

2.1.1. Interatomic potentials: modification

As mentioned above, one motivation in choosing Al–Ti systems was the recent availability of the high quality Al–Ti embedded-atom (EAM) potentials developed by Zope and Mishin [32]. The potentials were fitted to a large database of experimental as well as ab initio data. A comprehensive list of properties was reproduced accurately. Those that are particularly important for radiation damage in multilayers include the vacancy formation and migration energies, elastic moduli, stacking fault energies, and the formation energy of various bulk phases. In addition, the potentials yielded accurate coefficients of thermal expansion. Hence, isobaric-isothermal (*NPT*) simulations can be performed. In order to use the potentials for simulating radiation damage, the short-range parts need modification to accurately model the highly repulsive interactions that dominate the early stages of collision cascades. The modification was applied to the pair interactions of the EAM potentials.

For the short-range modification, ab initio energies of dimers Al–Al, Al–Ti and Ti–Ti at various bond lengths were calculated and used for fitting. VASP software was utilized to perform the first-principles calculations within the density-functional-theory (DFT) formalism using plane-wave bases [33,34]. Accurate projector-augmented-wave pseudopotentials with Perdew-Burke-Ernzerhof exchange correlations were used [35–37]. The plane-wave energy cutoffs were 240.30 and 178.33 eV for Al and Ti respectively. The number of electrons treated as valence electrons was three for Al and four for Ti. To simulate an isolated two-body system, Γ-point calculations were performed in a cubic box of side 15 Å. With this setup, the interactions between periodic images were verified to be negligible. The self-consistent loop was converged with a tolerance of 0.1 meV. To extract the two-body interaction potentials, the appropriate atomic energies were subtracted from the total energy. With these modifications, there were three regions of pair interactions based on the distance between two atoms r:

$$\phi = \begin{cases} \phi_{mod}, & r \leqslant r_{mod} \\ \phi_{sp}, & r_{mod} < r < r_{sp} \\ \phi_{zope}, & r_{sp} \leqslant r \end{cases} \quad (1)$$

$$\phi_{mod} = \frac{Z_1 Z_2}{r} \alpha e^{-\beta r/a} + \delta, \quad a = \frac{0.4683}{Z_1^{0.23} + Z_2^{0.23}} \quad (2)$$

$$\phi_{sp} = c_0 + c_1\lambda + c_2\lambda^2 + c_3\lambda^3, \quad \lambda = r - r_{mod} \quad (3)$$

In the above expressions, ϕ_{zope} denotes the original pair interaction, ϕ_{mod} denotes the part of pair interaction that is fitted to the ab initio data, and ϕ_{sp} represents a natural cubic spline interpolating ϕ_{zope} and ϕ_{mod} with Z the atomic number. The nonlinear-least-square fitted values of $r_{mod}, r_{sp}, \alpha, \beta$ and δ as well as the coefficients of the splines are presented in Table 1. The functional used in ϕ_{mod} (Eq. (2)) follows the usual Ziegler–Biersack–Littmark (ZBL) parameterization [38,39]. Fig. 1 shows the short-range part of the modified pair interactions along with the ab initio data points.

2.1.2. Multilayer construction

Five multilayer families (systems) were investigated: Mfcc, Mhcp, M100, Mcp and Mcpic. Within each system, four multilayers were constructed with different film thickness: three, six, 12 and 24 atomic layers per film. In this study, the keyword film refers to Al film or Ti film. The multilayer systems are designated as the following. MfccL3 represents stacking of face-centered-cubic (fcc) {1 1 1} close-packed layers of Al and Ti with three layers per film. MhcpL6 represents stacking of hexagonal close-packed (hcp) {0 0 0 1} layers of Al and Ti with six layers per film. M100L12 represents stacking of fcc {1 0 0} layers of Al and Ti with 12 layers per film. McpL24 represents stacking of fcc close-packed layers of Al and hcp close-packed layers of Ti with 24 layers per film. Mfcc, Mhcp, M100 and Mcp are multilayers with coherent interfaces. Mcpic multilayers are similar to Mcp only with incommensurate interfaces. Note that in an experimental work [40], fcc Ti grows epitaxially on Al (1 0 0) up to six layers, beyond which the axial alignment with the substrate is only partially preserved and off-normal alignment is lost, however the exact structure is unknown. On Al (1 1 1), Ti was experimentally determined to form a two-dimensional hcp overlayer up to two monolayers with an incommensurate interface, followed by three-dimensional island growth [41].

For the Mcp systems, the ground state stacking was determined via energy minimization with the conjugate-gradient technique as implemented in LAMMPS software [42]. The repeat unit was found to be abcABAbacBAB for the McpL3 and abcabcABABAB for the McpL6 (a lower or upper case denotes Al or Ti layer, respectively). The McpL12 and McpL24 multilayers are simply extensions of the McpL6. The stacking in Mcpic system follows that in Mcp. For comparison, four bulk structures were constructed: fccAl, hcpAl, fccTi and hcpTi. The lattice vectors of the simulation cells are denoted as $\mathbf{L}_1$ and $\mathbf{L}_2$ spanning the basal dimensions and $\mathbf{L}_3$ along the stacking direction. For all the coherent multilayers, cubic or nearly-cubic orthorhombic cells were used containing 55,296 atoms arranged in 48 layers, with $\mathbf{L}_1$, $\mathbf{L}_2$ and $\mathbf{L}_3$ along x, y, and z axes, respectively. The Mcpic systems were generated as follows. Starting from the ground state fcc Al and hcp Ti, the Al film was constructed using lattice vectors $\mathbf{a}_1 = [2.8636, 0, 0]$, $\mathbf{a}_2 = 2.8636 \times [\frac{1}{2}, \frac{1}{2}\sqrt{3}, 0]$ and $\mathbf{a}_3 = [0, 0, 2.3386]$ while the Ti film was constructed using lattice vectors $\mathbf{b}_1 = [2.9529, 0, 0]$, $\mathbf{b}_2 = 2.9529 \times [\frac{1}{2}, \frac{1}{2}\sqrt{3}, 0]$ and $\mathbf{b}_3 = [0, 0, 2.3402]$. Each Al layer was generated from 34×33 supercell (1122 atoms per atomic layer), while 33×32 supercell was done for Ti (1056 atoms per atomic layer). The total number of atoms in the Mcpic system was 52,272 (48 layers). The basal dimensions for the simulation cell were taken from the Al supercell, i.e. $\mathbf{L}_1 = 34 \times \mathbf{a}_1$ and $\mathbf{L}_2 = 33 \times \mathbf{a}_2$. Note that, even though the misfit was greatly minimized by such supercell sizes, it cannot be eliminated due to the incommensurability. Unlike in the coherent multilayers in which the Al film is exclusively under tensile (while Ti is exclusively compressed) in all basal directions, the Mcpic so constructed with an unequal length of basal vectors was thought to minimize such an exclusive strain in a particular film and to better model an unconstrained incommensurate system. The dimensions of all the structures and the strains in each layer at 300 K are presented in Table 2.

Table 1
Fitted parameters for the short-range part of the pair interactions modified from the original Al–Ti embedded-atom potentials [32].

	r_{mod} (Å)	r_{sp} (Å)	α (eV Å)	β (Å^{-1})	δ (eV)	c_0 (eV)	c_1 (eV Å^{-1})	c_2 (eV Å^{-2})	c_3 (eV Å^{-3})
Al–Al	1.65096	1.97712	0.617098	0.082469	−17.271753	4.85758	−27.43908	57.31412	−39.24883
Al–Ti	1.00066	2.62203	0.868468	0.476070	10.274221	15.26817	−24.51782	13.02075	−2.41210
Ti–Ti	0.50706	0.60457	0.485486	0.167387	−35.530090	185.50781	−755.59674	3877.36020	−10709.64591

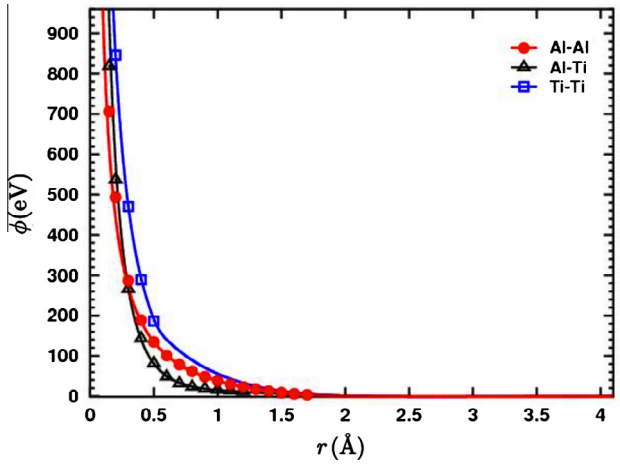

Fig. 1. Short-range part of the pair interactions modified from the original Al–Ti embedded-atom potentials [32]. The data points denote the ab initio energies used for fitting.

2.1.3. Molecular dynamics simulations setup

LAMMPS software was used to perform the MD simulations employing periodic boundary conditions (PBCs) in all dimensions. Before a displacement cascade was initiated, each structure was thermalized at 300 K and zero pressure (*NPT*) for 30 ps. To obtain a proper canonical distribution of velocity, the thermalization was performed using Nosé-Hoover thermostat with a time step of 0.5 fs and a 1-ps damping parameter [43,44]. To initiate a collision cascade, a random primary-knock-on atom (PKA) was chosen and was assigned an initial velocity normal to the stacking direction. Throughout this study, the PKA was given an initial kinetic energy of 1.5 keV. This PKA energy is sufficient to cause damage across most of the interfaces in the constructed multilayers and yet small enough to avoid overlaps of damage regions due to PBCs. The displacement cascade and damage recovery processes were simulated in five stages:

1. *Early collision* (0.025 ps): fix fixnve all nve; reset_timestep 0; timestep 0.005E−3; run 5000.
2. *Creation of thermal-spike regions* (1 ps): timestep 0.02E−3; run 50,000.
3. *Cooling of thermal-spike regions* (0.5 ps): timestep 0.05E−3; run 10,000.
4. *Main recovery* (4 ps): timestep 0.2E−3; run 20,000.
5. *Migration and final thermalization* (50 ps): unfix fixnve; fix fixnvt all nvt temp 300.0 300.0 1.0; timestep 0.5E−3; run 100,000.

Stages 1 → 4 were performed in a constant-energy (*NVE*) condition. In stage 1, the timestep was so chosen that no atom moved beyond approximately 0.005 Å per time step. Throughout the simulation, the temperature of the system was below 509 K and at the end of stage 2 the temperature was typically 390 K. During the last stage, the temperature was thermalized to 300 K with a damping factor of 1 ps.

Table 2
Dimensions of Al–Ti multilayers and bulk Al and Ti structures at 300 K. V_{vor} represents the average Voronoi volume per atom. $\bar{d}_z$ denotes the average Voronoi thickness of a layer in each film. The strains are calculated relative to the constituent bulk structure of Al or Ti in the multilayers (e. g. in Mfcc system the bulk structures are fccAl and fccTi while in Mcp system they are fccAl and hcpTi). $\Delta V = V_{vor} - V$, where V denotes the average atomic volume in the constituent bulk structures.

	L_x (Å)	$\bar{d}_z^{Al}$ (Å)	$\bar{d}_z^{Ti}$ (Å)	V_{vor}^{Al} (Å^3)	V_{vor}^{Ti} (Å^3)	ϵ_x^{Al} (%)	ϵ_x^{Ti} (%)	$\bar{\epsilon}_z^{Al}$ (%)	$\bar{\epsilon}_z^{Ti}$ (%)	$\frac{\Delta V}{V}^{Al}$ (%)	$\frac{\Delta V}{V}^{Ti}$ (%)
M100L3	24 × 4.218	1.825	1.983	16.244	17.645	3.65	1.52	−10.25	−4.55	−3.60	−1.60
M100L6	24 × 4.142	1.950	2.061	16.730	17.686	1.79	−0.30	−4.19	−0.80	−0.71	−1.38
M100L12	24 × 4.129	1.986	2.078	16.925	17.707	1.45	−0.63	−2.40	0.01	0.45	−1.26
M100L24	24 × 4.120	2.053	2.102	17.430	17.844	1.25	−0.83	0.91	1.18	3.45	−0.49
MfccL3	32 × 2.906	2.287	2.376	16.742	17.393	1.00	−1.08	−2.65	−0.94	−0.64	−3.01
MfccL6	32 × 2.913	2.304	2.393	16.933	17.587	1.23	−0.85	−1.95	−0.26	0.49	−1.93
MfccL12	32 × 2.914	2.323	2.395	17.084	17.613	1.26	−0.82	−1.14	−0.18	1.39	−1.78
MfccL24	32 × 2.919	2.279	2.425	16.829	17.900	1.45	−0.64	−2.98	1.07	−0.12	−0.18
MhcpL3	32 × 2.896	2.359	2.398	17.144	17.422	1.68	−1.98	−3.91	1.81	−0.66	−2.16
MhcpL6	32 × 2.904	2.388	2.390	17.445	17463	1.97	−1.70	−2.75	1.51	−1.08	−1.93
MhcpL12	32 × 2.909	2.403	2.382	17.612	17.458	2.14	−1.54	−2.12	1.16	2.05	−1.96
MhcpL24	32 × 2.918	2.343	2.387	17.281	17.605	2.46	−1.22	−4.57	1.36	0.13	−1.13
McpL3	32 × 2.906	2.304	2.375	16.841	17.362	0.97	−1.66	−1.95	0.85	−0.05	−2.49
McpL6	32 × 2.917	2.305	2.375	16.983	17.496	1.35	−1.29	−1.89	0.84	0.79	−1.74
McpL12	32 × 2.922	2.318	2.368	17.136	17.508	1.54	−1.11	−1.33	0.57	1.70	−1.68
McpL24	32 × 2.925	2.294	2.386	16.999	17.682	1.64	−1.01	−2.37	1.32	0.88	−0.70

Mcpic	L_1	L_2	$\bar{d}_z^{Al}$	$\bar{d}_z^{Ti}$	V_{vor}^{Al}	V_{vor}^{Ti}	ϵ_1^{Al}(%)	ϵ_1^{Ti}(%)	ϵ_2^{Al}(%)	ϵ_2^{Ti}(%)	$\bar{\epsilon}_z^{Al}$(%)	$\bar{\epsilon}_z^{Ti}$(%)	$\frac{\Delta V}{V}^{Al}$(%)	$\frac{\Delta V}{V}^{Ti}$(%)
L3	97.055	94.608	2.332	2.370	16.455	17.770	−0.80	-0.46	-0.36	0.05	−0.74	0.65	−2.34	-0.20
L6	97.332	94.666	2.347	2.362	16.644	17.801	−0.52	-0.18	-0.30	0.11	−0.13	0.30	−1.22	-0.03
L12	97.473	94.710	2.355	2.357	16.753	17.820	−0.37	-0.03	-0.25	0.16	0.21	0.10	−0.57	-0.08
L24	97.510	94.717	2.355	2.356	16.772	17.835	−0.34	0.01	-0.24	0.17	0.21	0.06	−0.46	0.16
	fccAl	fccTi	hcpAl	hcpTi										
a (Å)	4.069	4.155	2.848	2.955										
c/a	1.000	1.000	1.724	1.594										

The total simulation time was approximately 55.5 ps. For each structure, 20 runs were performed. In multilayer structures, ten runs with an Al PKA and ten runs with a Ti PKA were done. Within each system, only one initial thermalization run was performed. All damage cascades in this system were started from the same thermalization restart file. For defect counting analysis, a reference configuration was generated with molecular static energy minimization in each system. Voronoi cells were then constructed using these reference sites. Unoccupied cells were identified as vacancies and the number of vacancies was taken as the number of Frenkel pairs.

2.2. Experimental techniques

An Al/Ti multilayer thin film stack for a total thickness of 400 nm with individual layer thickness of 5 nm was fabricated on a cleaned silicon (100) substrate using direct current magnetron sputter deposition. The base pressure of the sputter deposition system was 5×10^{-8} Torr. Individual layers of Ti and Al were deposited at cathode powers of 180 and 240 W, respectively, with 2 mTorr argon process gas pressure. Helium implantation (30 kV) to a dose of 10^{16} ions/cm^2 was performed using a He ion microscope on an area of 10×10 μm^2. The total thickness of the stack was chosen in such a way that maximum damage is located in the center of the stack. The damage profile and maximum ion range were estimated using Stopping Range of Ions in Matter (SRIM) simulation (shown in Fig. 8c) [38,45,46]. For a He ion fluence of 10^{16} ions/cm^2, the estimated peak damage was 0.375 dpa, which is located approximately at a depth of 180-nm from the surface.

After He implantation, a cross sectional transmission electron microscopy (TEM) lamella sample was fabricated using site specific FIB lift-out process. TEM imaging was performed using a JEOL 2010F TEM. Overfocused and underfocused TEM imaging was performed to image the He bubbles. Helium bubbles show bright contrast in underfocused TEM images and darker contrast in overfocused images. The TEM images of the region between the top surface and peak helium implantation dose are shown in Fig. 8. In the underfocused image, the bubbles can be clearly seen to be preferentially segregated to the darker contrast Ti layers. Furthermore, a spatial distribution of He bubbles within the Ti layer closer to the interface of Ti/Al is also observed. Surprisingly the Al layer did not appear to have any bubbles or the bubble size is below the TEM resolution, which is estmated to be about 1-nm.

3. Results and discussion

3.1. Simulation results

All of the displacement cascade simulations were initiated with a 1.5 keV PKA, either Al or Ti. The evolution of damage production (the number of Frenkel pairs) from the simulations is plotted in Fig. 2a. The plotted quantities are the average values from the 20 cascade simulations. Different colors represent different systems. In each multilayer system, different film thicknesses are plotted with a different symbol, namely L3 (triangle), L6 (square), L12 (diamond) and L24 (circle). The number of produced Frenkel pairs rises quickly within sub-pico second timespans and reaches maximum N_{max} at approximately 0.3 ps. Following this stage, most of the displaced atoms quickly recover to lattice sites within several pico seconds. Ti (black curve) exhibits the fastest recovery rate, followed by Mfcc, (Mcpic, Mcp, M100), Mhcp, and finally Al. Fig. 3a shows the N_{max} for all the systems. It appears that the recovery rate is correlated with N_{max}, i.e. the rate increases as N_{max} increases. Since one may think of N_{max} as a measure of the size of the damage

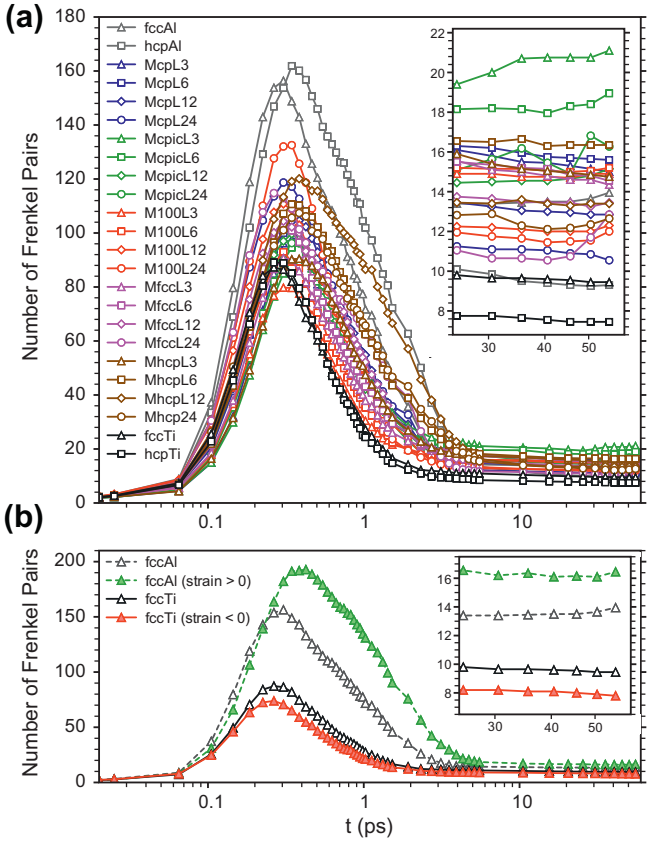

Fig. 2. (a) Evolution of the damage production initiated with a 1.5 keV primary-knock-on atom. (b) Effect of isotropic strain on defect production in fcc Al ($\epsilon_{iso} = 2.11\%$) and in fcc Ti ($\epsilon_{iso} = -2.07\%$).

region, the correlation may be simply a consequence of a fact that thermal recovery takes longer for atoms for larger damage volumes.

To study the effect of strain on the damage production, simulations on fcc Al and fcc Ti with reverse lattice constants were performed. We note that this study serves only to illustrate the effect of strain. This is because the actual strain tensor in the multilayer cannot be accurately predicted only from the bulk lattice parameters. The complexity of the strain behavior in multilayer is evident from strain table given in Table 2. For the sake of illustration, fcc Ti was chosen instead of hcp Ti to be compared with fcc Al so that the strain effect may be seen in the absent of crystal structure effect. At 300 K, the lattice constant of fcc Al is 4.069 Å while fcc Ti is 4.155 Å. Systems with a reverse lattice constant: fcc Al with 4.155 Å and fcc Ti with 4.069 Å correspond to isotropically strained systems with $\epsilon_{iso} = 2.11\%$ for Al and $\epsilon_{iso} = -2.07\%$ for Ti. Fig. 2b shows the effect of strain on the defect production and recovery rate. The given tensile strain on fcc Al increases N_{max} by (192.8–156.4)/156.4 = 23% and reduces the recovery rate. On the other hand, the compressive strain on fcc Ti decreases N_{max} by (87.6–73.9)/87.6 = 16% and increases the recovery rate.

It is worth noting that we have performed simulations to investigate the effect of the PKA direction on the damage evolution curve. Simulations on fcc Al with a PKA initially along [111] compared to [100] yield remarkably similar curves. Tests on M100L6 and McpL6 with PKA direction normal vs. tangential to the stacking also produced very similar damage behaviors. This indicates that 1.5 keV used in this study was sufficient to smear out any orientation effect that would otherwise be significant for energies close to the displacement threshold energy E_t (the minimum kinetic energy required to create at least one stable Frenkel pair). Note that E_t

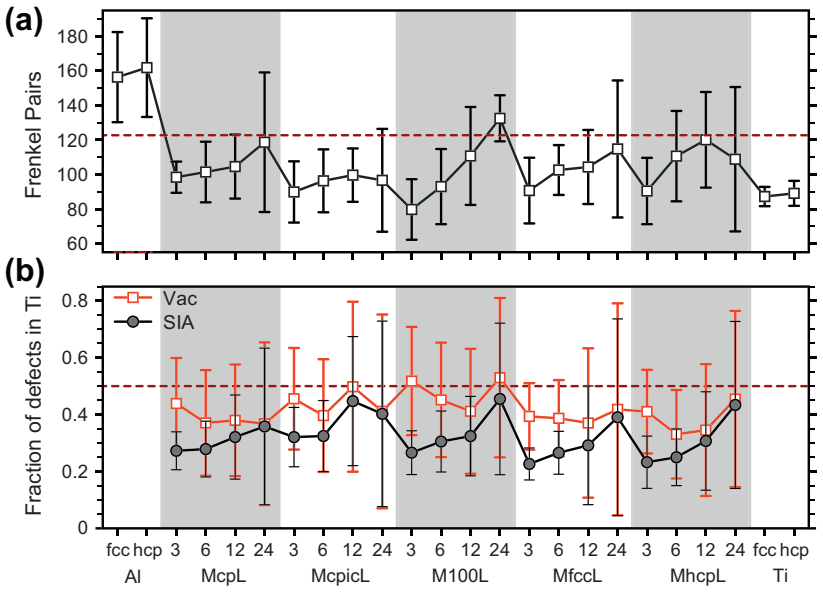

Fig. 3. (a) Number of Frenkel pairs and (b) fraction of vacancies and interstitials in the Ti films at maximum damage production near 0.3 ps. The dashed line in (a) marks the average between the value of fccAl and hcpTi.

varies with the crystallographic direction. We have determined that the average E_t are 20.9 eV (fcc Al), 20.5 eV (hcp Al), 35.4 eV (fcc Ti) and 33.3 eV (hcp Ti).

Fig. 3a shows the maximum number of Frenkel pairs during the cascades near 0.3 ps. The error bars represent the standard deviation from the 20 runs. During this period, a trend of maximum damage production as a function of film thickness was observed within each multilayer system, i.e. N_{max} decreases as the film thickness in each multilayer decreases. This characteristic is particularly pronounced in M100. Note that the value for L24 of Mcpic and Mhcp is smaller than that for the corresponding L12, however the observed trend was still valid within the standard deviation. Within the error bars, N_{max} in all multilayers falls in between that of bulk Al (at the higher end of $N_{max,fccAl} \sim 156$ pairs) and bulk Ti (at the lower end of $N_{max,hcpTi} \sim 89$ pairs). What is interesting is that N_{max} in the multilayers is less than the average bulk value $N_{max,bulk} = (N_{max,fccAl} + N_{max,hcpTi})/2$ (dashed line in Fig. 3a). The difference between N_{max} and $N_{max,bulk}$ diminishes as L increases, as expected. Hence the first finding is that the number of displaced atoms during maximum damage production is suppressed in the nanolayered systems and the effect is amplified as the constituent films are made thinner. This finding is generally consistent with both experimental observations [19], although the research reported here appears to be the first comprehensive simulation study to demonstrate this for point defects (no He atoms).

To understand the trend of N_{max} as a function of L, we constructed a phenomenological model based on the absorption coefficient of a film in slowing down the energetic atoms. Due to its higher E_t, it is logical to assume that Ti has a larger absorption coefficient than Al. The reduction of N_{max} as L is decreased may be a consequence of an increased fraction of PKA energy being absorbed in the Ti than in the Al films as L is reduced. Increasing the portion of deposited energy in the Ti films would increase the effective E_t in the multilayer and consequently suppress damage production. With a hypothesis that changing the number of partitions (film interfaces) in the multilayer alters the fraction of energy deposited in the Ti film, the phenomenological model was developed as the following: Let f_{Ti} and f_{Al} be the fraction of energy loss due to (absorbed by) a Ti and Al layer respectively. If we start with a Ti PKA in the first Ti layer and the collision proceeds towards the second Ti layer and so forth, the fraction of energy deposited in the first and second Ti layer is respectively

$$\chi_{Ti,1} = f_{Ti} \tag{4}$$

$$\chi_{Ti,2} = f_{Ti}(1 - f_{Ti}), \tag{5}$$

and the total fraction deposited in the Ti and Al film in the first pair of Ti–Al film containing L layers each is respectively

$$\chi_{Ti}^{p=1} = \sum_{i=1}^{L} f_{Ti}(1 - f_{Ti})^{i-1} \tag{6}$$

$$\chi_{Al}^{p=1} = \sum_{i=1}^{L} f_{Al}(1 - f_{Al})^{i-1}(1 - f_{Ti})^{L} \tag{7}$$

Similarly, if we start with an Al PKA, the loss fraction in the first L-layer Ti and L-layer Al is

$$\chi_{Ti}^{p=1} = \sum_{i=1}^{L} f_{Ti}(1 - f_{Ti})^{i-1}(1 - f_{Al})^{L} \tag{8}$$

$$\chi_{Al}^{p=1} = \sum_{i=1}^{L} f_{Al}(1 - f_{Al})^{i-1} \tag{9}$$

Hence, the average loss fraction in the Ti film in the p-th pair due to Ti PKA and Al PKA is

$$\chi_{Ti}^{p} = \frac{1}{2}[(1 - f_{Ti})(1 - f_{Al})]^{L(p-1)} \times \sum_{i=1}^{L} f_{Ti}(1 - f_{Ti})^{i-1}(1 + (1 - f_{Al})^{L}) \tag{10}$$

and finally, the ratio of the energy deposited in the Ti film relative to that in Al from all 48 layers as a function of film thickness is

$$\chi(L) = \sum_{p=1}^{24/L} \chi_{Ti}^{p} \Big/ \sum_{p=1}^{24/L} \chi_{Al}^{p} \tag{11}$$

Fig. 4 shows χ as a function of L for the case of $f_{Al} = 0.1$ for several $R = f_{Ti}/f_{Al}$ ratios: 0.8, 1.0, 1.5 and 2.0. All χ curves approach unity in the limit of infinite L. For $f_{Ti} > f_{Al}$ case, it can be seen that

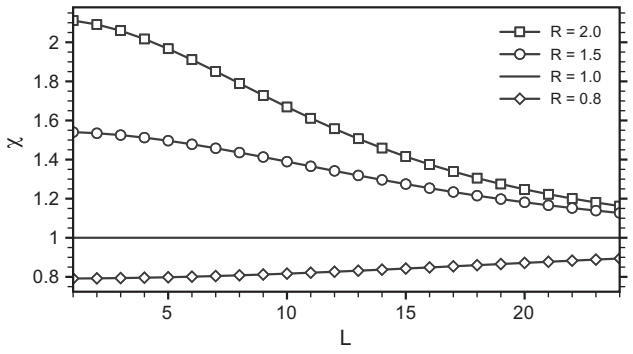

Fig. 4. Ratio between energy deposited in the Ti film and in the Al film (χ) as a function of the number of layers per film L for the case of $f_{Al} = 0.1$ for several $R = f_{Ti}/f_{Al}$ where f denotes the fraction of energy deposited per layer.

χ increases as L is decreased confirming the hypothesis that an increased fraction of the PKA energy is deposited in the Ti films as the film thickness is reduced.

We realize that in multilayers, the absorption coefficient for each layer varies even within the same film due to the different atomic environments and strain fields experienced by each layer. Moreover, determining the value of f_{Ti} and f_{Al} of each layer is not straightforward. However, we believe that the underlying physics captured in the model sufficiently describes the observed trend of N_{max} vs. L, at least qualitatively. In other words, in a multilayer system, even though the proportion of the constituent materials is kept the same, the response of the system can be driven closer to the more dominant materials by reducing the thickness of each film. In this case, N_{max} in L3 is the closest to that in pure bulk Ti.

The number of surviving defects at the end of simulations (N_{end}) is plotted in Fig. 5a. The values for the bulk structures are $N_{end,fccAl} \sim 14$ and $N_{end,hcpTi} \sim 7$. The dashed line at 10.5 marks the average bulk value $N_{end,bulk} = (N_{end,fccAl} + N_{end,hcpTi})/2$. In all of the multilayers, even though $N_{max} < N_{max,bulk}$, the surviving number of defects is larger than $N_{end,bulk}$. This indicates that the vacancy-interstitial recombination in these multilayers is inhibited. The defect spatial distribution, defect cluster morphology as well as the strain field may contribute to altering the defect recombination process.

To better understand how defects are distributed in the multilayer, we present an analysis of defect distribution at the maximum damage production regime as well as at the end of the simulations. The defect distribution near the maximum damage production is presented in Fig. 3b. The plotted quantities are the fractions of vacancies (square marks) and self-interstitial atoms SIAs (circles) in the Ti films. The plot shows that there are fewer vacancies in Ti films than in Al films. This is understood from the larger E_t of Ti. There are also fewer interstitials in the Ti films than in Al films. In fact, in the Ti films the number of interstitials is even smaller than the number of vacancies. This indicates that there is an imbalance flux of displaced atoms from Ti films to Al films. The degree of imbalance systematically increases as the film thickness decreases (as the number of interfaces is increased). Near the interface, we observe that displacing a Ti atom from a Ti film to the Al region is energetically favorable compared to the opposite process. This was caused by the fact that it is easier for heavier Ti atoms to displace lighter Al atoms whose E_t is also smaller than otherwise. Hence, the interface has induced a preferential drift of SIAs from the Ti to the Al films causing imbalance population of SIAs relative to vacancies in a particular film. We refer to this phenomenon as "partitioning" effect. It is expected then that the partitioning effect inhibits defect recombination in multilayers relative to multilayer systems that do not experience such defect partitioning. However, based on the varied and generic observations by many others on the asymmetry of damage in many of the multilayered systems studied to date, both miscible and immiscible, we expect that this is an important result that emerged from this study that has wide-ranging implications for multilayer radiation damage tolerance. In general, defect partitioning contributes to multilayer degradation and failure since it directly leads to damaging differential response.

Fig. 5b shows the vacancy-SIA fraction imbalance in the Ti films at the end of the simulations. Unlike the imbalance curve near the maximum damage production (Fig. 3b), the imbalance at the end of simulation shows two different characteristics depending on the multilayer system. Firstly, in Mcp, Mfcc and Mhcp, the imbalance is still evident, in fact it is more pronounced due to the much

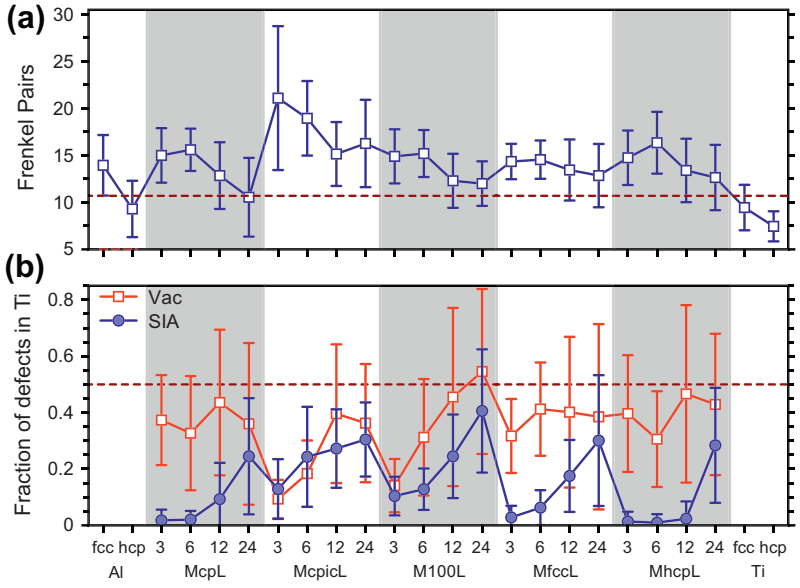

Fig. 5. (a) Number of Frenkel pairs and (b) fraction of vacancies and interstitials in the Ti films at the end of simulation after 55.5 ps. The dashed line in (a) marks the average between the value of fccAl and hcpTi.

smaller fraction of SIAs that survives in the Ti films. As the result of the partitioning effect, in the Ti films the number of vacancies is more than what is needed for the recombination, while in the Al film there are more SIAs than the available vacancies to recombine. The second characteristic of the imbalance curve is observed in Mcpic and M100. In the M100, even though the fraction of vacancies in the Ti films is still larger than the fraction of SIAs, the difference diminishes towards L3. In the Mcpic, the fraction of vacancies in the Ti films becomes comparable to that of SIAs. In this case, it appears that a portion of SIAs in the Al films recombine with vacancies in the Ti films, particularly those at the interface, mostly during the early stages of recovery. The different characteristic of fraction imbalance at the end of simulation between Mcp–Mfcc–Mhcp and M100-Mcpip may be related to the strain in the film. From Table 2, in the first group of multilayers, Ti films are compressed in both basal directions ($\epsilon_x^{Ti} = \epsilon_y^{Ti} < 0$) and the compressive strain increases as film thickness decreases. The opposite case occurs in the second group of multilayers: in the M100 ϵ_x^{Ti} gradually becomes >0 at L3, while in Mcpic even though ϵ_1^{Ti} is slightly <0, ϵ_2^{Ti} is >0. In addition, unlike in all other systems in which Al films are under tension, Al film in the Mcpic is slightly compressed. We believe that the reduction of the exclusivity of compressive strain in the Ti films (on one hand) and tensile strain in the Al films (on the other hand) in the M100 and Mcpic multilayers plays a role in reducing the vacancy-SIA fraction imbalance by allowing a portion of the SIAs in the Al film to recombine with vacancies in the Ti film near the interface during the recovery process.

Besides the differential defect distribution (partitioning effect), the different strain levels that are experienced by each layer in the film can significantly affect defect migration. The SIAs may either preferentially migrate to the interface or to the middle of the film away from the interface. To study defect migration, the number of surviving vacancies and interstitials at the end of the simulations in each layer along the multilayer stacking direction is calculated. Fig. 6 shows the result for L6 in each multilayer (other film thicknesses show similar distributions). In Fig. 6 the vacancies are plotted with hollow marks while interstitials are presented as filled marks. In all systems, the multilayer starts with Al film at the bottom (gray) followed by Ti film (blue). The stacking sequence is included in the plot for clarity. As has been discussed, the majority of the defects are found in the Al films. Fig. 6 also reveals that in all mutilayers except the M100, the SIAs are preferentially found at the interface layer in the Al film. Meanwhile, for M100, the interstitials preferentially migrate to the middle of the Al films. The interstitials in Ti film in M100 also migrate to the middle of the Ti film even though the number is much smaller than in Al films.

To understand why the interstitials in the Al films migrate to the middle of the film in M100 while they migrate to the interface layer in all the close-packed multilayers, formation energies of dumbbells in McpL6 (to represent the multilayers of close-packed layers) and M100L6 were calculated. A single interstitial was added to the system and the atoms were relaxed via energy minimization. The results are presented in Table 3.

In McpL6, the preferred location for the Al–Al dumbbell is at the interface layer of Al films with [11$\bar{2}$] orientation (in plane with the close-packed layer) with a formation energy of 1.27 eV. Note that Miller indices used to describe the dumbbell orientation are with respect to a cubic system. In the middle of the Al films, the preferred Al–Al dumbbell orientation is [100] with a formation energy of 1.84 eV (~0.6 eV higher than that at the interface layer). The

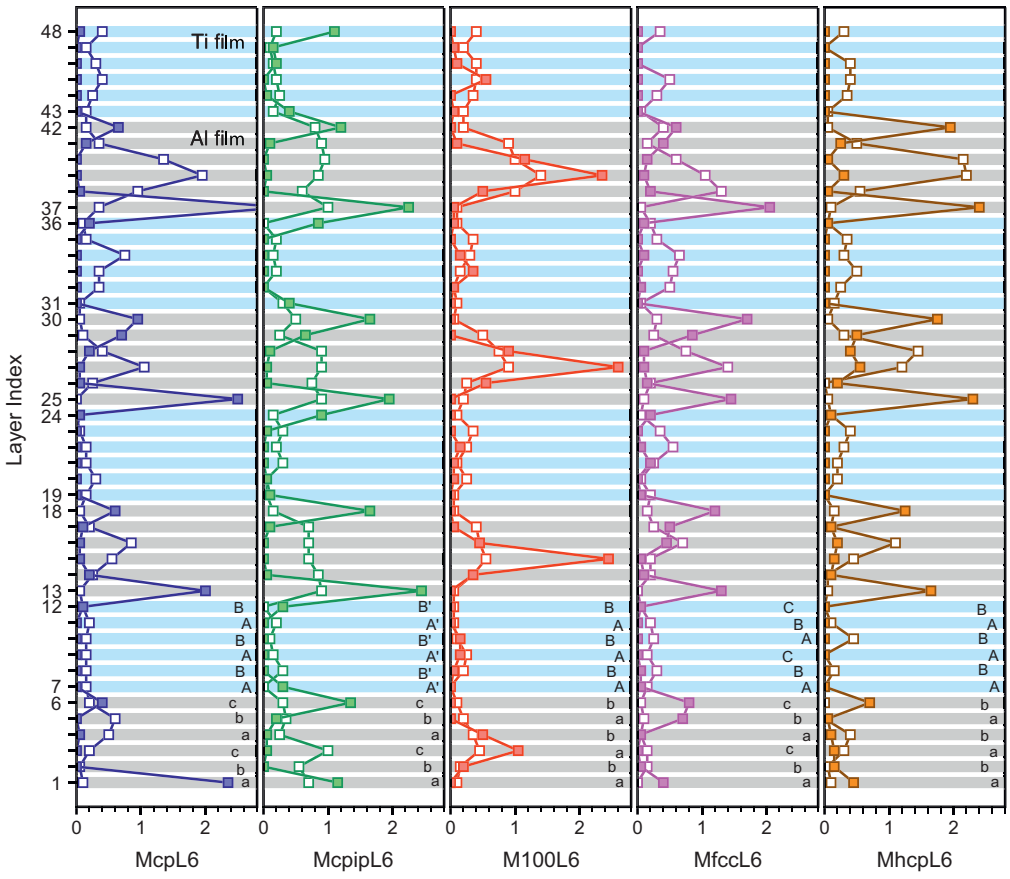

Fig. 6. Distribution of vacancies (hollow squares) and interstitials (filled squares) at the end of simulation after 55.5 ps.

Table 3
Dumbbell orientation and formation energy E_f in McpL6 and M100L6 multilayer. Layer indexing in the stacking starts from bottom to top: Al-1 → Al-6, Ti-7 → Ti-12 and so on. The * indicates that a dumbbell stabilizes in a different layer than its initial position during relaxation. All Miller indices are with respect to a cubic system.

Layer	Dumbbell	E_f (eV)	Bond (Å)
McpL6			
Al-1	$[11\bar{2}]$ (Al–Al)	1.27	2.27
Al-2	$[11\bar{2}]$ (Al–Al)	1.68	2.26
Al-3	[100] (Al–Al)	1.82	2.35
Al-4	[100] (Al–Al)	1.84	2.35
Al-5	$[11\bar{2}]$ (Al–Al)	1.82	2.26
Al-6	$[10\bar{1}]$ (Al–Al)	1.64	2.27
Ti-7*	$[10\bar{1}]$ (Al–Al) in Al-6	1.07	2.27
Ti-8	$[11\bar{2}]$ (Ti–Ti)	3.31	2.26
Ti-9	$[11\bar{2}]$ (Ti–Ti)	3.28	2.32
Ti-10	$[11\bar{2}]$ (Ti–Ti)	3.27	2.26
Ti-11*	$[11\bar{2}]$ (Al–Al) in Al-13	0.59	2.26
Ti-12*	$[11\bar{2}]$ (Al–Al) in Al-13	0.59	2.26
M100L6			
Al-1*	[001] (Al–Al) in Al-2	2.03	2.29
Al-2*	[001] (Al–Al) in Al-3	1.84	2.34
Al-3	[100] (Al–Al)	1.78	2.36
Ti-7*	[001] (Ti–Ti) in Ti-8	3.04	2.32
Ti-8*	[001] (Ti–Ti) in Ti-9	2.91	2.33
Ti-9	[100] (Ti–Ti)	2.88	2.34

situation in the Ti films is even more pronounced, if a Ti interstitial is found in the middle layer of a Ti film, it forms a $[11\bar{2}]$ dumbbell with formation energy of 3.28 eV. If the Ti interstitial is placed in the Ti layers 11 or 12 (interface layer), it initiates a sequence of relaxations so that one Ti atom occupies a lattice site in the Al films leaving an Al interstitial in Al layer 13 (interface layer) forming an Al–Al $[11\bar{2}]$ dumbbell with formation energy of only 0.59 eV. The opposite trend of dumbbell formation energy is found in M100L6. In this case, the Al–Al dumbbells are most stable in the middle of Al films forming in [100] orientation with formation energy of 1.78 eV compared to 2.03 eV for [001] dumbbell found at the interface layer. Within the Ti films, the middle layer also provides the stable location for Ti–Ti dumbbell forming in [100] orientation with formation energy of 2.88 eV compared to 3.04 eV for [001] dumbbell found at the interface. Hence, it is clear why in the close-packed multilayers, the SIAs migrate to the interface while in the M100 system they migrate away from the interface to the middle of the film. Fig. 7 illustrates the migration process of an Al interstitial initially placed in the Al interface layer (red atom) that results in the formation of a [100] dumbbell in Al middle layer (gray).

3.2. Experimental results

Fig. 8a shows the cross-section image of Al–Ti multilayer sample with thickness of 5 nm per film (~21 layers) obtained with underfocused TEM. The image was taken after He irradiation with dose 10^{16} atoms/cm^2 at room temperature. In this image, Ti films appear darker than Al due to atomic number contrast. In the Ti films, bright spots can be seen that represent He bubbles. The diameter of the bubbles is ~1 nm. This result is intriguing for a reason that due to a lower displacement threshold energy of Al compared to Ti, the nucleation of small bubbles via a kickout mechanism (a cluster of He atoms displacing a host atom from its lattice site) would be expected to occur in Al films. As a reference, to create a 1-nm bubble, ~56 Ti atoms or ~59 Al atoms would need to be displaced.

The fact that the bubbles are found in the Ti films suggests that the distribution of He atoms during the irradiation plays a major role in determining the morphology and location of the bubbles. It is possible that the larger stopping power of Ti films has caused the He atoms to be stopped and contained in the Ti films more effectively than in Al films. In this scenario, the necessary space needed for the bubbles is created not via a kickout mechanism but rather during the collision cascade itself. In this stopping process, the impinged Ti atoms may remain in the Ti films or be displaced to the Al films. If the impinged Ti atoms can be displaced to the Al films, this process will greatly favor the creation of the necessary excess volume for the He atoms to form small bubbles in Ti films. The defect imbalance that is observed in the simulations

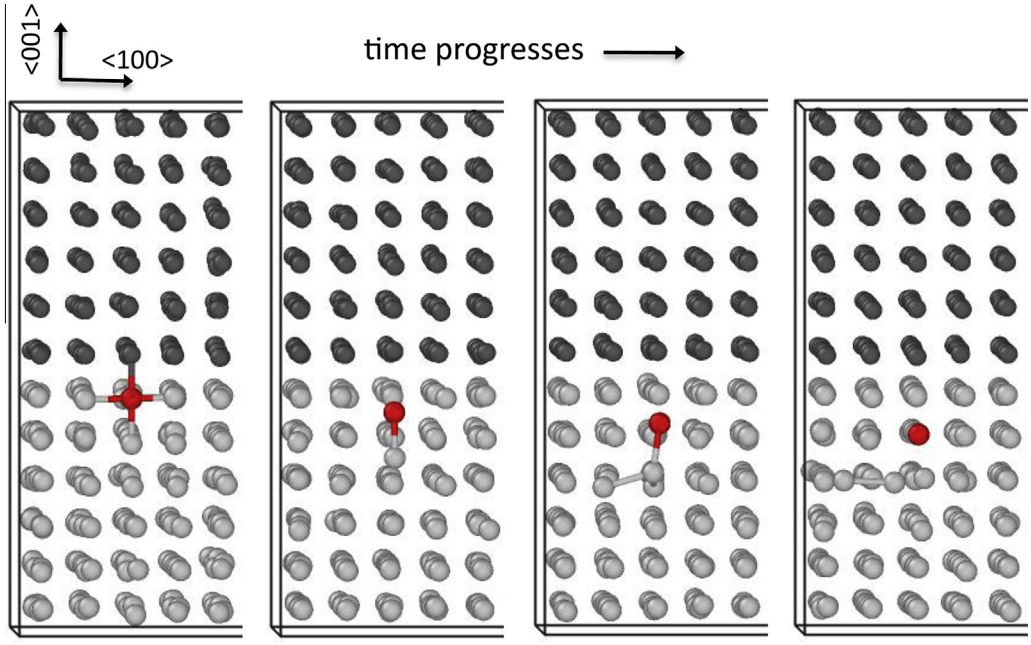

Fig. 7. Migration pathway of an Al atom (red) initially at octahedral interstitial site in M100L6 resulting in the formation of a [100] dumbbell in the middle layer of Al film (light gray). (For interpretation of the references to color in this figure legend, the reader is referred to the web version of this article.)

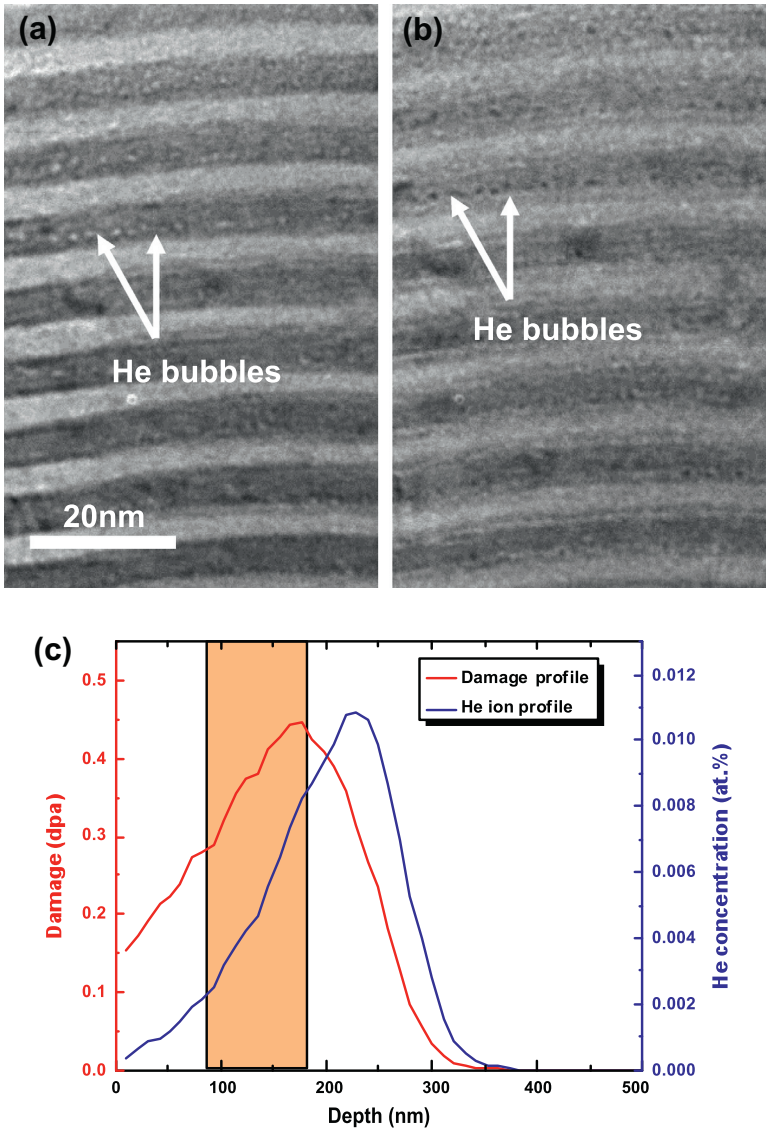

Fig. 8. (a) Underfocused and (b) overfocused TEM images showing the location of Helium bubbles in the upper middle region of the Ti/Al multilayer sample 5 nm per film. In the underfocused image the He bubbles appear bright and in overfocused image He bubbles have dark contrast. The bubbles are preferentially segregated to the darker contrast Ti layers. (c) SRIM simulation showing He ion profile and damage profile.

provides a clear proof that displacing Ti atoms from Ti films to Al films is indeed easier than the reverse.

In Fig. 8a, the He bubbles are arranged in a row with a somewhat regular spacing between the bubbles. More importantly, the bubbles are located near the interface towards the Al films below the Ti films where they reside, i.e. the location of the bubbles is biased towards the direction of the irradiation. This provides another clue that He bubble formation in the Ti films is associated with a preferential flux of SIAs from Ti films to Al films during the irradiation as described above.

Fig. 8c shows the He ion profile and the damage profile obtained with SRIM simulations. The rectangular block represents the region of Al–Ti sample that was imaged. The damage profile corresponds to the distribution of the vacancies.

4. Conclusion

This work has revealed several important properties of Al/Ti nanolayers in response to radiation damage, the most important finding being the observation of strong defect partitioning during collision cascades that imparts a strong asymmetry in radiation damage. During maximum damage production initiated with 1.5-keV PKA, asymmetry in point defect creation between the two dissimilar materials Al or Ti is observed with ~60% of vacancies are created in Al films while ~70% of interstitials are created in Al films. The excess interstitials in the Al films are a direct consequence of the preferential flux of displaced atoms in this nanolayered system. He irradiation experiments at a low dose of 10^{16} atoms/cm^2 and at room temperature were performed to investigate the interface effects on radiation damage. The experimental data shows a formation of ~1-nm diameter bubbles in the Ti films near the interface. The results from the simulations and experiments seem to suggest that the He bubble formation is associated with the preferential flux of SIAs during the irradiation in that the He atoms impinge on Ti films and displace Ti atoms into the Al films. This is further supported by the location of the bubbles being near the interface and biased towards the direction of the irradiation.

In all of the interface models in this study, the number of Frenkel pairs created during maximum damage production is smaller than the bulk average of the constituent materials. This difference is amplified for thinner films in accordance with experimental observations on other multilayer systems. This observation is understood using a phenomenological model that Ti exhibits a larger stopping power than Al and that the fraction of energy deposited in Ti films increases as the films are made thinner. On the other hand, the number of surviving Frenkel pairs at the end of simulations is larger than the bulk average. The difficulty for anti-defect recombinations is caused by defect partitioning in which in Al films there are too many interstitials than the available vacancies while the opposite applies in Ti films. This defect partitioning increases with the increasing number of interfaces (thinner films) resulting in more than 90% of surviving interstitials located in the Al films for nanolayers with $\leqslant$6 layers per film.

These simulation results, when considering all the other experimental and modeling results for nanolayered systems, suggest that, in addition to interface structure and chemical mixing, we add degree of defect partitioning to the list of desirable system properties in the design of radiation tolerant material systems. Differential material responses that grow with increased radiation dose are not a recipe for stable damage tolerant material systems.

Acknowledgments

This research was supported by the award BRCALL08-Per4-E-1-0062 from Defense Threat Reduction Agency (DTRA). A portion of this research was performed using Olympus supercomputer at EMSL (#44724), a national scientific user facility sponsored by the Department of Energy's Office of Biological and Environmental Research and located at Pacific Northwest National Laboratory. We thank Dr. Tamas Varga for fruitful discussions.

References

[1] G. Was, Fundamentals of Radiation Materials Science, 1st ed., Springer-Verlag, 2007.
[2] K.E. Sickafus, R.W. Grimes, J.A. Valdez, A. Cleave, M. Tang, M. Ishimaru, S.M. Corish, C.R. Stanek, B.P. Uberuaga, Nature Materials 6 (2007) 217.
[3] M.L. Lescoat, J. Ribis, A. Gentils, O. Kaitasov, Y. deCarlan, A. Legris, Journal of Nuclear Materials 428 (2012) 176.
[4] P. He, M. Klimenkov, R. Lindau, A. Moslang, Journal of Nuclear Materials 428 (2012) 131.
[5] L. Hsiung, M. Fluss, S. Tumey, J. Kuntz, B. El-Dasher, M. Wall, B. Choi, A. Kimura, F. Willaime, Y. Serruys, Journal of Nuclear Materials 409 (2011) 72.
[6] M.K. Miller, K.F. Russell, D.T. Hoelzer, Journal of Nuclear Materials 351 (2006) 261.
[7] S. Ukai, S. Ohtsuka, Energy Materials 2 (2007) 26.
[8] R. Lindau, A. Moslang, M. Rieth, M. Klimiankou, E. Materna-Morris, A. Alamo, A.A.F. Tavassoli, C. Cayron, A.M. Lancha, P. Fernandez, N. Baluc, R. Schaublin, E. Diegele, G. Filacchioni, J.W. Rensman, B. Schaaf, E. Lucon, W. Dietz, Fusion Engineering and Design 75 (2005) 989.
[9] G.R. Odette, M.J. Alinger, B.D. Wirth, Annual Review of Materials Research 38 (2008) 471.
[10] Y. Wu, E.M. Haney, N.J. Cunningham, G.R. Odette, Acta Materialia 60 (2012) 3456.
[11] H.L. Heinisch, F. Gao, R.J. Kurtz, Journal of Nuclear Materials 329 (2004) 924.
[12] A. Misra, M.J. Demkowicz, X. Zhang, R.G. Hoagland, JOM 59 (2007) 62.
[13] X. Zhang, E.G. Fu, N. Li, A. Misra, Y.Q. Wang, L. Shao, H. Wang, Journal of Engineering Materials and Technology, Transactions of the ASME 134 (2012) 041010.
[14] P.D. Edmondson, C.M. Parish, Y. Zhang, A. Hallen, M. Miller, Scripta Materialia 65 (2011) 731.
[15] G.R. Odette, D.T. Hoelzer, JOM 62 (2010) 84.
[16] A. Kashinath, A. Misra, M.J. Demkowicz, Physical Review Letters 110 (2013) 086101.
[17] M. Demkowicz, A. Misra, A. Caro, Current Opinion in Solid State and Materials Science 16 (2012) 101.
[18] M. Zhernenkov, M.S. Jablin, A. Misra, M. Nastasi, Y. Wang, M.J. Demkowicz, J.K. Baldwin, J. Majewski, Applied Physics Letters 98 (2011) 241913.
[19] E. Fu, H. Wang, J. Carter, L. Shao, Y. Wang, X. Zhang, Philosophical Magazine 93 (2013) 883.
[20] Y.-T. Cheng, Materials Science Reports 5 (1990) 45.
[21] T. Höchbauer, A. Misra, K. Hattar, R.G. Hoagland, Journal of Applied Physics 98 (2005) 123516.
[22] M. Demkowicz, Y. Wang, R. Hoagland, O. Anderoglu, Nuclear Instruments and Methods in Physics Research Section B: Beam Interactions with Materials and Atoms 261 (2007) 524.
[23] X. Zhang, N. Li, O. Anderoglu, H. Wang, J. Swadener, T. Höchbauer, A. Misra, R. Hoagland, Nuclear Instruments and Methods in Physics Research Section B: Beam Interactions with Materials and Atoms 261 (2007) 1129.
[24] M.J. Demkowicz, D. Bhattacharyya, I. Usov, Y.Q. Wang, M. Nastasi, A. Misra, Applied Physics Letters 97 (2010) 161903.
[25] D. Bhattacharyya, M. Demkowicz, Y. Wang, R. Baumer, M. Nastasi, A. Misra, Microscopy and Microanalysis 18 (2012) 152.
[26] M. McPhie, L. Capolungo, A. Dunn, M. Cherkaoui, Journal of Nuclear Materials 437 (2013) 222.
[27] N. Li, M. Nastasi, A. Misra, International Journal of Plasticity 32 (2012) 1.
[28] K. Hattar, M. Demkowicz, A. Misra, I. Robertson, R. Hoagland, Scripta Materialia 58 (2008) 541.
[29] E. Fu, J. Carter, G. Swadener, A. Misra, L. Shao, H. Wang, X. Zhang, Journal of Nuclear Materials 385 (2009) 629.
[30] N. Li, J. Carter, A. Misra, L. Shao, H. Wang, X. Zhang, Philosophical Magazine Letters 91 (2011) 18.
[31] Q. Wei, Y. Wang, M. Nastasi, A. Misra, Philosophical Magazine 91 (2011) 553.
[32] R.R. Zope, Y. Mishin, Physical Review B 68 (2003) 024102.
[33] G. Kresse, J. Hafner, Physical Review B 47 (1993) 558.
[34] G. Kresse, J. Furthmüller, Physical Review B 54 (1996) 11169.
[35] P.E. Blöchl, Physical Review B 50 (1994) 17953.
[36] G. Kresse, D. Joubert, Physical Review B 59 (1999) 1758.
[37] J.P. Perdew, K. Burke, M. Ernzerhof, Physical Review Letters 77 (1996) 3865.
[38] J.F. Ziegler, J.P. Biersack, U. Littmark, The Stopping and Range of Ions in Solids, Pergamon, New York, 1985.
[39] M. Hossain, J. Freund, H. Johnson, Nuclear Instruments and Methods in Physics Research Section B: Beam Interactions with Materials and Atoms 267 (2009) 1061.
[40] A.A. Saleh, V. Shutthanandan, N.R. Shivaparan, R.J. Smith, T.T. Tran, S.A. Chambers, Physical Review B 56 (1997) 9841.
[41] Y.W. Kim, G.A. White, N.R. Shivaparan, M.A. Teter, R.J. Smith, Surface Review and Letters 06 (1999) 775.
[42] S. Plimpton, Journal of Computational Physics 117 (1995) 1.
[43] S. Nose, The Journal of Chemical Physics 81 (1984) 511.
[44] W.G. Hoover, Physical Review B 31 (1985) 1695.
[45] J. Biersack, L. Haggmark, Nuclear Instruments and Methods 174 (1980) 257.
[46] J.F. Ziegler, 2013. <http://www.srim.org>.

Computational Materials Science 85 (2014) 269–279

Contents lists available at ScienceDirect

Computational Materials Science

journal homepage: www.elsevier.com/locate/commatsci

Displacement threshold energy and recovery in an Al–Ti nanolayered system with intrinsic point defect partitioning

Matthew Gerboth, Wahyu Setyawan *, Charles H. Henager Jr.

Pacific Northwest National Laboratory, Richland, WA 99352, USA

ARTICLE INFO

Article history:
Received 10 July 2013
Received in revised form 26 November 2013
Accepted 7 January 2014
Available online 1 February 2014

Keywords:
Radiation damage
Nanostructured multilayers
Displacement threshold energy
Pseudo-random direction

ABSTRACT

A method is established and validated using molecular dynamics (MD) to determine the displacement threshold energies as E_d in nanolayered, multilayered systems of dissimilar metals. The method is applied to specifically oriented nanolayered films of Al–Ti where the crystal structure and interface orientations are varied in atomic models and E_d is calculated. Methods for defect detection are developed and discussed based on prior research in the literature and based on specific crystallographic directions available in the nanolayered systems. These are compared and contrasted to similar calculations in corresponding bulk materials, including fcc Al, fcc Ti, hcp Al, and hcp Ti. In all cases, the calculated E_d in the multilayers are intermediate to the corresponding bulk values but exhibit some important directionality. In the nanolayer, defect detection demonstrated systematic differences in the behavior of E_d in each layer. Importantly, collision cascade damage exhibits significant defect partitioning within the Al and Ti layers that is hypothesized to be an intrinsic property of dissimilar nanolayered systems. This type of partitioning could be partly responsible for observed asymmetric radiation damage responses in many multilayered systems. In addition, a pseudo-random direction was introduced to approximate the average E_d without performing numerous simulations with random directions.

Published by Elsevier B.V.

1. Introduction

Radiation damage in solids from collision cascades formed during high-energy particle irradiation, ions or neutrons, is extremely costly and, perhaps, the single most complex and challenging technological problem facing nuclear material scientists, reactor designers, and regulatory agencies desiring long-lived engineering structures, low operational costs, and safety. The search for and development of materials with improved radiation damage tolerance requires a more or less complete understanding of defect production, transport, evolution, and recovery in complex alloy or composite systems that are undergoing irradiation and transitions far from equilibrium on picosecond time scales at the atomic level to decade-long microstructural and thermo-physical property changes as either structural or functional materials. These properties undergo unavoidable time-, temperature-, and fluence-dependent degradation and are, usually, irreversible processes [1] such that replacement or costly mitigation is required to satisfy operational safety concerns at certain fluence levels. Therefore, there is a strong scientific and technological interest in studying and developing radiation damage tolerant materials.

One proven mechanism relies on enhanced damage recovery mechanisms via increased recombination rates of radiation-induced defects at defect sinks within a material. These sink sites range from grain boundary denuded zones observed in many materials to engineered materials containing nano-spaced interfaces, including nano-featured ferritic alloys and nanolayered materials. The general concept of point defect recombination at internal interfaces is not a new idea but has achieved recent significance from work with oxide dispersion-strengthened (ODS) alloys [2–7], nano-featured alloys [8,9], and nano-layered composites [10–12] specifically designed to achieve high strength and enhanced defect recombination at closely spaced sinks for vacancies and self-interstitials. Capture and immobilization of helium (He) is also of keen interest for fusion reactor materials where He can be produced at levels approaching a few atomic percent [13–17].

Specifically, nanolayered materials based on dissimilar materials arranged in closely spaced layered structures with very high interfacial areal fractions are considered to be developmental radiation tolerant materials. The specific details of the damage tolerance are still being studied and evaluated but it is considered that enhanced defect recombination at the dissimilar interfaces is occurring that reduces the overall damage accumulation relative to bulk materials. However, some specific trends are noted and discussed in the literature, namely, that asymmetric behavior begins to be noticed after certain irradiation doses using He ion

* Corresponding author. Tel.: +1 (509)371 7692; fax: +1 (509)375 3033.
E-mail address: wahyu.setyawan@pnnl.gov (W. Setyawan).

0927-0256/$ - see front matter Published by Elsevier B.V.
http://dx.doi.org/10.1016/j.commatsci.2014.01.008

implantation. These asymmetries include He bubble morphologies in Cu–Nb and differential swelling in Cu–Nb multilayers [17,18].

The use of low energy He ion implantation to study ion beam mixing and radiation damage in nanolayered thin films is useful since He damage rates are reduced compared to heavy ions, the ranges are appropriate for thin films, and the effects of He accumulation are relatively easily observed compared to point defect clustering as a measure of radiation damage. It is understood that He bubble formation proceeds from vacancy (V) accumulation and He–V binding. Thus, observing He bubbles is a surrogate for observing V clustering in these thin film materials. Höchbauer et al. [19] were the first to study He accumulation as bubbles in Cu–Nb nanolayered materials. They observed preferential He bubble formation at Cu–Nb interfaces and columnar grain boundaries following 33 keV He implantation. Demkowicz et al. [20] concluded that He also accumulates along Cu–Nb interfaces and that these interfaces act as fast diffusing pathways for He escape during annealing. Zhernenkov et al. used neutron reflectometry to study He locations in implanted Cu–Nb foils and concluded that He was likely being stored as interstitial He in the dissimilar interfaces until a critical concentration is reached, after which He bubbles are formed [17]. Perhaps the best evidence comes from 3He implantations and using nuclear reaction analysis (NRA) to study He concentrations as a function of implantation depth together with transmission electron microscopy (TEM) to determine He concentrations where He bubbles form [21]. Similar conclusions were reached by Bhattacharyya et al. using TEM and NRA to study 3He-implanted Cu–Nb foils [22]. Interface structure appears to play a critical role in the amount of He that can be stored before bubbles form [16]. Recent MD studies are consistent with this understanding and demonstrate atomic storage mechanisms for He in certain interfaces [15,23].

However, once this critical concentration of He is reached then He bubbles can nucleate and grow in these layered materials just as in bulk metals. A key difference, though, is that He bubble morphologies and locations vary from layer to layer and, above a certain dose, appear to depend on some intrinsic property of the layer material rather than the interfaces [24]. Hattar et al. [18] observed He bubbles in both the Cu and Nb layers of a Cu–Nb 5 to 6-nm layered foil after high doses of 33 keV He ion implantation at 763 K. However, He bubbles in the Cu layer spanned the thickness of the entire layer and were approximately 5–6 nm in diameter, whereas He bubbles in the Nb layer were about 1–2 nm in diameter. Similar observations of He bubble suppression compared to bulk or 100-nm layered materials are observed in Cu–V nanolayered foils [25] and in Cu–Mo nanolayered foils [26], where a slight size difference between He bubbles in Cu (larger) compared to Mo layers was noted. Wei et al. [27] observed bubble size differences in Ag–V nanolayered materials somewhere between the Cu–Nb size differences and those observed for Cu–V, with the larger bubbles contained in the Ag layer. Fu et al. nicely summarize dose effects in Cu–V nanolayered systems and discuss He effects, radiation hardening, and both mixing and demixing effects observed in other systems [28].

One trend that appears to be consistent in these nanolayered studies is the observation that a certain level of asymmetry develops with regard to He bubble morphologies at increased He doses. Bubble sizes are non-uniform after a certain dose and the evidence is not clear that this asymmetry does not develop earlier in the radiation damage regime. Helium storage at the dissimilar interface does not destroy the symmetry of the system, although, asymmetric swelling amounts are often noted [17,24,18,25], along with asymmetric He bubble sizes [18]. These become serious issues with dealing with nanolayered failure mechanisms due to radiation damage, perhaps from delamination or other mechanical failures due to differential responses. The source of this asymmetry, which will eventually lead to failure, is not discussed in the current studies. In this respect we find that there has been a lack of theoretical studies on nanolayered radiation damage and this paper focuses on one aspect of the problem for a specific layered system that can be arranged in atomic models in a wide variety of stable structures, namely, the Al–Ti system.

One shortcoming in the current literature and that is addressed in this research is the lack of understanding of point defects in nanolayered systems at low energies where ion beam mixing and demixing effects do not occur readily. In particular, displacement thresholds have not been studied for any of these layered systems to help understand or predict if some part of the response asymmetry may be due to displacement threshold effects. There is no reason to expect that defect generation or fates are symmetric within nanolayered materials made up of dissimilar metals. Under asymmetric defect generation the ability of the system to avoid damage accumulation via enhanced recombination may be compromised. One layer may accumulate an excess of one kind of point defect or defect cluster over time. The differential He bubble size observed in Cu–Nb suggests that this type of damage cannot be overlooked or ignored.

2. Methods

2.1. Interatomic potentials

Zope et al. recently developed a high-quality interatomic potential for Al–Ti systems [29]. The embedded-atom method (EAM) was used to fit the potential to density-functional-theory (DFT) data. Among the bulk properties that were able to reproduce, those particularly important for radiation damage in the form of atomic displacements and defects include point defects formation and migration energies and stacking fault energies. On the other hand, the potential was found to be too soft at short ranges as it was not designed for radiation damage. Therefore, we modified the pair interactions Al–Al, Al–Ti and Ti–Ti to better model the short range repulsions using DFT data.

Since in the early stages of atomic collisions the repulsions would involve mostly binary collisions, it is reasonable to use ab initio energies of Al–Al, Al–Ti and Ti–Ti dimers as a function of bond length. The DFT calculations were performed using the VASP code [30,31]. We used the projector-augmented-wave pseudopotentials [32,33] as implemented in the code with Perdew–Burke–Ernzerhof exchange correlations [34]. The plane-wave energy cutoffs were 240.30 and 178.33 eV for Al and Ti, respectively. To simulate a dimer, a convergence study with respect to the cell size was performed. It was found that a cubic cell of size 15 Å or larger was necessary to render the effect of periodic boundaries negligible. Throughout the calculations, the self-consistent loop was converged within 0.1 meV.

The pair interactions ϕ were modified so that $\phi = \phi_{mod}$ for $r \leqslant r_{mod}$ and given by:

$$\phi_{mod} = \frac{Z_1 Z_2}{r}\alpha e^{-\beta r/a} + \delta, \quad a = \frac{0.4683}{Z_1^{0.23} + Z_2^{0.23}} \tag{1}$$

The first term of ϕ_{mod} in the above functional was adopted from the standard Ziegler–Biersack–Littmark (ZBL) formula [35,36] with Z_i being the atomic number of element i. These modified interactions were joined to the original forms via cubic splines ϕ_{sp} so that $\phi = \phi_{sp}$ for $r_{mod} < r \leqslant r_{sp}$ and given by:

$$\phi_{sp} = c_0 + c_1\lambda + c_2\lambda^2 + c_3\lambda^3, \lambda = r - r_{mod} \tag{2}$$

Table 1 contains the fitted values of $r_{mod}, r_{sp}, \alpha, \beta$ and δ as well as the coefficients of the cubic splines. Fig. 1 shows the short-range part of the modified pair interactions along with the ab initio data points.

Table 1
Fitted parameters for the short-range part of the pair interactions modified from the original Al–Ti embedded-atom potentials [29].

	r_{mod} (Å)	r_{sp} (Å)	α (eV Å)	β (Å^{-1})	δ (eV)	c_0 (eV)	c_1 (eV Å^{-1})	c_2 (eV Å^{-2})	c_3 (eV Å^{-3})
Al–Al	1.65096	1.97712	0.617098	0.082469	−17.271753	4.85758	−27.43908	57.31412	−39.24883
Al–Ti	1.00066	2.62203	0.868468	0.476070	10.274221	15.26817	−24.51782	13.02075	−2.41210
Ti–Ti	0.50706	0.60457	0.485486	0.167387	−35.530090	185.50781	−755.59674	3877.36020	−10709.64591

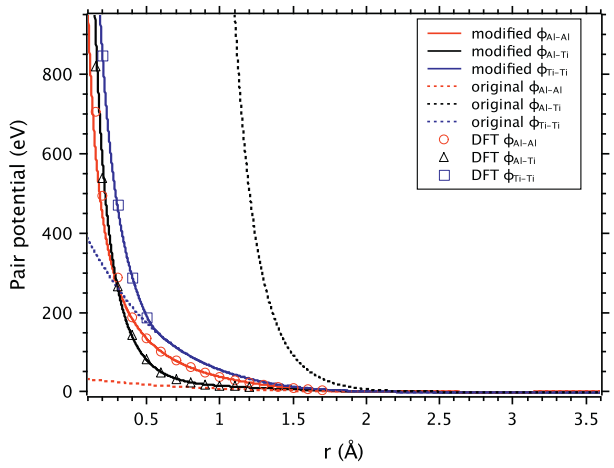

Fig. 1. Short-range part of the pair interactions modified from the original Al–Ti embedded-atom potentials [29]. The data points denote the ab initio energies used for fitting.

The original pair interactions are also shown as dashed curves. Significant improvements of the short-range part of the potentials with respect to ab initio data are evident from Fig. 1.

2.2. Simulation system

The primary system considered in this work is a multilayered system composed of alternating layers of Al and Ti. The Al–Ti multilayer was built with face-centered cubic (fcc) (001) layers stacked along the [001] direction. The simulation cell was composed of 4 alternating layers, each 5 atomic layers thick. Each layer was 12 × 12 unit cells. The simulation cell contained a total number of 5760 atoms (Fig. 2a). This was large enough such that, during the simulations, the cascades did not overlap themselves due to the periodic boundaries. For the multilayer, the directions [100], [010] and [001] were located along the x, y and z axes, respectively. The stacking direction was along the z axis.

Additionally, 4 bulk structures were constructed for comparison, namely fcc Al, fcc Ti, hexagonal close-packed (hcp) Al and hcp Ti. For the fcc structures, the orientation of the Miller indices is the same as that in the multilayer. The fcc Al contained 6912 atoms spanning 12 × 12 × 12 cubic unit cells. The fcc Ti was constructed with 5324 atoms (11 × 11 × 11 unit cells). The hcp structures were composed of an AB stacking of the close-packed layers along z. The primitive lattice vectors were oriented along $\mathbf{a}_1 = [a, 0, 0]$, $\mathbf{a}_2 = \left[\frac{a}{2}, \frac{a}{2}\sqrt{3}, 0\right]$ and $\mathbf{a}_3 = [0, 0, c]$ (at 300 K, $a = 2.849, c/a = 1.724$ for hcp Al and $a = 2.959, c/a = 1.586$ for hcp Ti). The Miller indices in the hcp structures were with respect to these $\mathbf{a}_1$, $\mathbf{a}_2$ and $\mathbf{a}_3$ vectors, hence the [1 1 0] direction is 30° from the x axis (see Fig. 2b). However, the simulation cell was constructed from an orthorhombic unit cell with lattice vectors $\mathbf{b}_1 = \mathbf{a}_1$, $\mathbf{b}_2 = 2\mathbf{a}_2 - \mathbf{a}_1 = [0, a\sqrt{3}, 0]$ and $\mathbf{b}_3 = \mathbf{a}_3$. The unit cell for the hcp systems is shown in Fig. 2b. The total number of atoms in the hcp systems was 9000 atoms spanning $15\mathbf{b}_1 \times 10\mathbf{b}_2 \times 15\mathbf{b}_3$.

2.3. Molecular dynamics simulation

The molecular dynamics simulations were performed using LAMMPS software with periodic boundary conditions (PBCs) in all directions [37]. Before each set of displacement cascade simulations was performed, the systems were thermalized at 300 K and zero-pressure (NPT) using a Nose–Hoover thermostat. Before thermalization some of the supercells were relaxed with energy minimization using the conjugate gradient method.

Searches for the displacement threshold energies were performed by simulating displacement cascades as follows. A random primary knock-on atom (PKA) was chosen and given an initial kinetic energy of 5 or 10 eV. Upsweeping was done by increasing the PKA energy with an interval equal to the initial energy (5 or 10 eV) until a defect was detected. Once a defect was detected, downsweeping was performed by decreasing the PKA energy by 1 eV until the defect was no longer detected. The lowest value at which a defect was detected is reported as the displacement

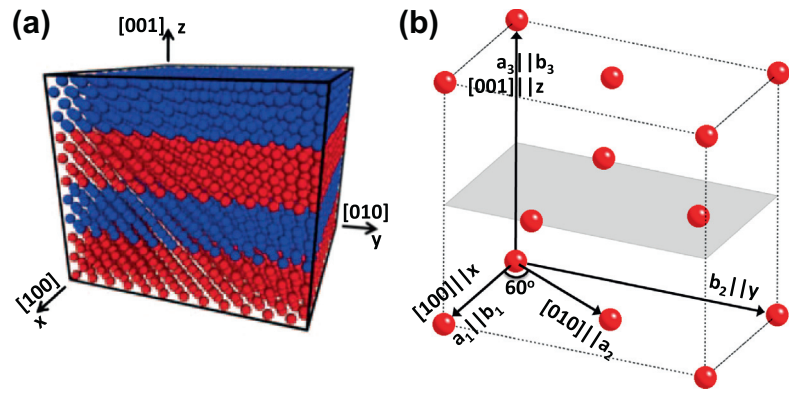

Fig. 2. (a) Al–Ti multilayer structure composed of fcc (001) layers of Ti (red) and Al (blue) stacked along the [001] direction. The atomic layers are numbered 1–20 starting from the base of the supercell. (b) The primitive lattice vectors $\mathbf{a}_1, \mathbf{a}_2, \mathbf{a}_3$ and unit cell lattice vectors $\mathbf{b}_1, \mathbf{b}_2, \mathbf{b}_3$ used to construct hcp structures (the Miller indices in hcp are with respect to the primitive vectors). (For interpretation of the references to color in this figure legend, the reader is referred to the web version of this article.)

threshold energy (E_d) for that trial. The PKAs were chosen randomly throughout the thermalized lattice, so that an average of the trials includes a broad range of thermal fluctuations. The simulations were followed for 7.5 ps with a timestep of 0.05 fs before point defect detection was performed. During the displacement cascade simulations, thermostating at 300 K and barostating were implemented using either the LAMMPS fix NPT or NVT. The choice of fix was based on the defect detection algorithms. For NPT, pressure was kept at zero.

2.4. Defect detection

In order to detect the defects produced during the simulations two algorithms were implemented as components of a pre/post-processing package. The first algorithm searched the lattice points and detected any lattice position that contained no atom within a radius of 0.8 Å of the site at the end of the simulation. These lattice points were considered vacancies. The lattice positions were taken from the initial thermalized state before the simulation. This algorithm required careful setting of the detection radius to account for thermal vibrations of atoms.

The second algorithm utilized Voronoi cells (also known as Wigner–Seitz cells) built around a reference configuration (the energy minimized supercell) in order to detect defects. Defects were detected based on the occupancy of the cell: cells containing no atoms were considered vacancy sites. This method improves the robustness against thermal motion. Nevertheless, with 0.8 Å detection radius, Algorithm 1 yielded the same defect counting as the Voronoi method.

2.5. Averages of displacement threshold energies

A value for E_d averaged over all directions is also useful in characterizing multilayer systems and the overall system behavior since initial PKA directions are typically not well defined crystallographic directions. In general the average E_d can be determined as a spherical average of the threshold as a function of the orientation (θ, ϕ) [38]:

$$E_{d,\mathrm{avg}} = \frac{\int_0^{2\pi}\int_0^{\pi} E_d(\theta,\phi) sin\theta \mathrm{d}\theta \mathrm{d}\phi}{\int_0^{2\pi}\int_0^{\pi} \sin\theta \mathrm{d}\theta \mathrm{d}\phi} \tag{3}$$

This average simplifies to an arithmetic mean when the data is evenly distributed in three-dimensional (3D) space. For unevenly distributed data, the average E_d was calculated using a binning method with interpolation. Bins were constructed in the first octant of the 3D space. A triangular shape was used to construct the spherical grids starting from a parent triangle with vertices at (1,0,0), (0,1,0), and (0,0,1) and iteratively dividing it into subsequent triangles. Due to the crystallographic symmetry of the systems, only one octant (+x, +y, +z) was needed with the other octants equivalent. Subdivision was accomplished by inserting new vertices at the mid-point of each edge, and then extrapolating the new vertices along their radial component to intersect the surface of the a sphere with radius one. The new vertices were then connected to form 4 new triangles, with the original triangle discarded. Subdivision was continued in this manner until the appropriate number of bins was achieved, which in this study was 64 bins.

Using these bins, the spherical average of the displacement threshold energy $E^{\mathrm{av}}_{d,\mathrm{sph}}$ was calculated as follows:

$$E^{\mathrm{av}}_{d,\mathrm{sph}} = \frac{1}{N}\sum_{i=1}^{N}\left(\frac{1}{n_i}\sum_{j=1}^{n_i} E_{d,ij}\right) \tag{4}$$

$$SE = \frac{1}{N}\sqrt{\sum_{i=1}^{N}\left[\left(\frac{1}{n_i}\sum_{j=1}^{n_i} E_{d,ij}\right) - E^{\mathrm{av}}_{d,\mathrm{sph}}\right]^2} \tag{5}$$

In the above, i is the bin index and j is the trial index. $E_{d,ij}$ is the threshold energy of trial j in bin i. N is the number of bins, and n_i is the number of trials in bin i. Note that the summation of j calculates the average threshold energy in each bin, while the summation over i calculates the final average over the bins. Therefore, the above formulation effectively transforms a non-uniform PKA orientation distribution into a uniform one.

If the random orientation sampling resulted in a set of data in which there were no trials in some bins, the values for the empty bins were linearly interpolated from the average E_d of the surrounding 3 bins, i.e., the ones that share a common edge with the current bin. This interpolation was performed only once and only if all neighbor bins were originally populated to avoid artificial smearing. All remaining empty bins were excluded from the averaging. The standard error (SE) reported for this average was calculated using Eq. (5). A software routine was written to preform the calculations as part of the pre/post-processing package.

In addition to the random orientation, the specific dependence of threshold energy on crystal orientation was investigated by systematically sweeping the PKA direction along high-symmetry crystal directions. The arithmetic average from this orientation-dependent sweep is denoted as $E^{\mathrm{av}}_{d,\mathrm{od}}$. This is acceptable as the trials were evenly distributed with equal numbers of trials at each point in a sweeping pattern. For $E^{\mathrm{av}}_{d,\mathrm{od}}$, the standard deviation was calculated as:

$$\sigma = \sqrt{\frac{\sum_{k=1}^{m}\left(E^{\mathrm{av}}_{k} - E^{\mathrm{av}}_{d,\mathrm{od}}\right)^2}{m}} \tag{6}$$

where m is the number of crystal orientations in the sweep and E^{av}_{k} is the average value of the trials at orientation k. This method of calculating the standard deviation captures the variation of the threshold for different directions. $E^{\mathrm{av}}_{d,\mathrm{od}}$ is not as robust an average as $E^{\mathrm{av}}_{d,\mathrm{sph}}$ since $E^{\mathrm{av}}_{d,\mathrm{od}}$ relies on the choice of directions included in the sweeping pattern. Therefore, in this paper, $E^{\mathrm{av}}_{d,\mathrm{sph}}$ will be regarded as the better estimate of the overall average of the displacement threshold energy.

2.6. Open-source analysis software

Software was written to perform the point defect detection, construction of the spherical grids, interpolation and calculation of the spherical average of the threshold energy $E^{\mathrm{av}}_{d,\mathrm{sph}}$. This software is available for free as supplemental materials in this paper. A short usage manual is given in Appendix A.

3. Results and discussion

3.1. Bulk materials

3.1.1. Random PKA directions

Using sets of simulations with randomly chosen initial PKA directions, $E^{\mathrm{av}}_{d,\mathrm{sph}}$ was calculated for the bulk materials using 200 PKAs per system. The directions were chosen within the first octant of the 3D space. Fig. 3 shows the colormap of the threshold energy spatial distribution. The plotted quantity is the average value in each bin. Note that later on, a systematic sweep along high-symmetry directions is presented, and the data from this systematic sweep has been included (in addition to 200 random trials) in the calculation of $E^{\mathrm{av}}_{d,\mathrm{sph}}$ (Table 2) and the spherical average map (Fig. 3) for statistical robustness.

In both fcc Al and fcc Ti, low values of E_d were found in the [100] and [110] directions, while the high values were located in regions in between those low-value directions. The low index directions lie along the close packed direction [110] for fcc and along the second nearest neighbor direction [100]. Along these directions, atoms are arranged in the shortest bonds providing easy

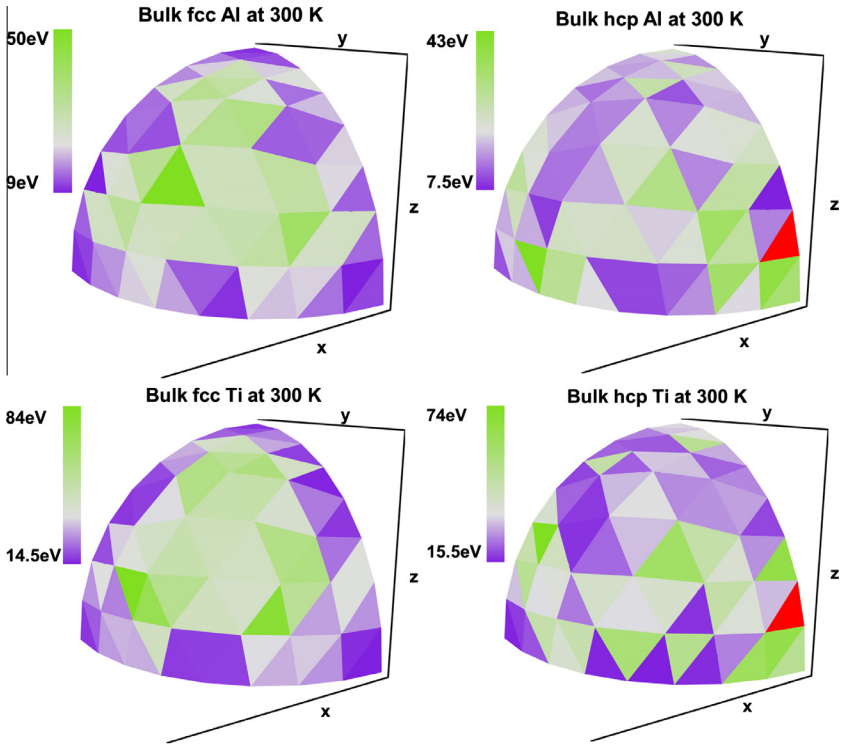

Fig. 3. Map showing the spherical distribution of the displacement threshold energy E_d obtained from trials with randomly directed PKAs in bulk materials at 300 K. Bins for which no trials were recorded are plotted in reds. (For interpretation of the references to color in this figure legend, the reader is referred to the web version of this article.)

Table 2
Spherical average of displacement threshold energy ($E^{av}_{d,sph}$) from randomly oriented PKAs and arithmetic average ($E^{av}_{d,od}$) from systematically-oriented PKAs along high-symmetry crystal directions in bulk structures and face-centered cubic {100} Al–Ti nanolayer with 5 atomic layers per elemental layer. for the systems. Data from the systematic sweeping has been included in the calculation of $E^{av}_{d,sph}$ for robustness. Binning statistics are included.

System	Bulk fcc Al	Bulk hcp Al	Bulk fcc Ti	Bulk hcp Ti	Multilayer (Al PKA)	Multilayer (Ti PKA)	Multilayer PKAs
$E^{av}_{d,sph}$ (eV)	20.9	20.5	35.4	33.3	25.2	22.4	23.8
Std. error (eV)	1.1	0.9	2.0	1.7	1.3	1.2	1.0
Empty bins/interpolated bins	1/1	4/3	0/0	1/0	7/1	2/2	0/0
$E^{av}_{d,od}$ (eV)	20.2	18.7	31.8	25.6	25.6		
σ	9.2	6.0	15.2	9.6	9.6		

collision replacement paths. The correlation between low values of E_d and a replacement path is also evident from the hcp structures along close-packed directions [100] (x-axis) and [010] (60° from x-axis in the xy-plane). Hence, the replacement path provides an easy mechanism for a displaced atom to become an interstitial, away from the initial PKA location.

The values of $E^{av}_{d,sph}$ for fcc Al, hcp Al, fcc Ti and hcp Ti are 20.9, 20.5, 35.4 and 33.3 eV, respectively. For a given element, the averages for fcc and hcp structures are remarkably similar (see Table 2). This similarity may be due to the fact that both are close-packed structures. In a comparative study of defect production among fcc, hcp and body-centered cubic (bcc) metals, it was indicated that there was no obvious correlation between crystal structure and the characteristics of the defect production curve as a function of PKA energy [39]. Note that in the cited reference, the energy of the PKA is typically $>100\times E^{av}_{d,sph}$. In such a regime of PKA energies, it is expected that the number of subsequent collisions is large enough and exhibit enough randomness to smear out any effect of the initial PKA direction. Therefore, it appears that $E^{av}_{d,sph}$ is more of an intrinsic property of the element and that the effect of crystal structure if any is minimal. However, this may not be the case in nanolayered structures where certain directionality is imposed for low-energy PKAs in particular.

The values of $E^{av}_{d,sph}$ calculated for the bulk materials were consistent with the values reported in the literature [1,40–42], however in general the $E^{av}_{d,sph}$ calculated were higher than those reported: between 20 and 30 eV for Ti and 16 and 20 eV for Al. The experimental determinations of threshold energies were preformed at temperatures between 6 and 21 K while the simulations were at 300 K. The lattice vibration provides more resistance for a displaced atom to escape the location where the PKA originates, effectively increasing the E_d. In this regards, the higher values from the simulations results are sensible.

3.1.2. Crystal orientation dependence

From the colormap distribution data of E_d, the low values were observed if the PKA was directed along the close-packed directions. To study more detail about the anisotropy of E_d, a systematic set of PKA directions was chosen. For the bulk fcc materials, the initial PKA directions were swept around the high-symmetry crystallographic directions $[100]\rightarrow[110]\rightarrow[111]\rightarrow[001]$ with 5° resolution. Ten trials were performed at each direction in Al, thirty in Ti. Fig. 4 shows the results for fcc Al and fcc Ti. The data points represent E_d from the trials. At each direction, an arithmetic average was calculated and a spline curve connecting these averages was plotted (solid line). Both fcc Al and fcc Ti reveal similar features.

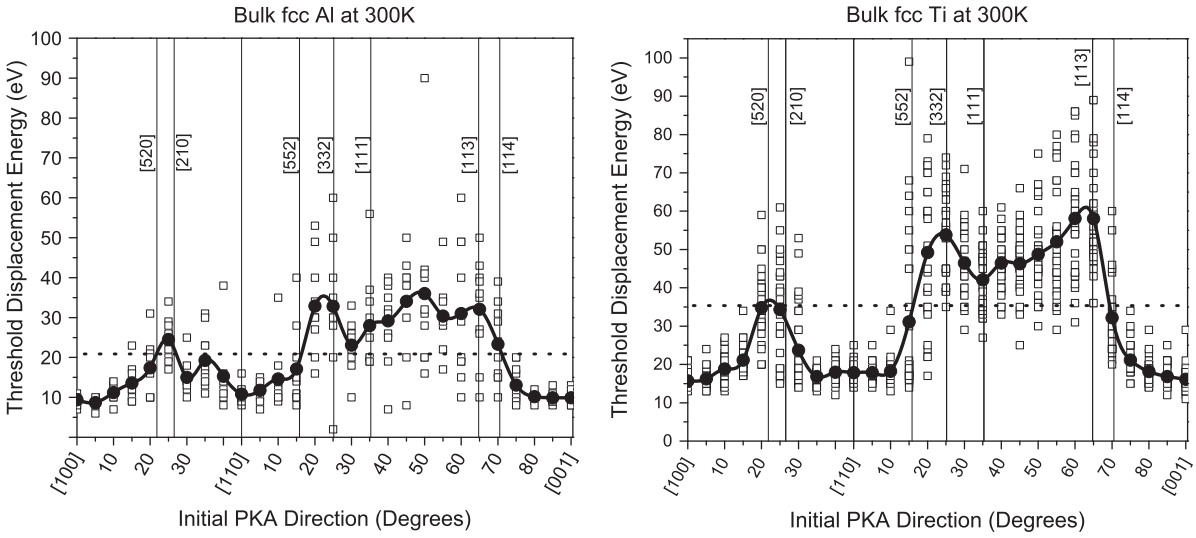

Fig. 4. Orientation dependence of the displacement threshold energy in bulk fcc materials. Hollow squares denote the value of E_d from an individual trial at the given direction. The solid curve and solid circles represent the trial average. The horizontal dashed line denotes the spherical average $E_{d,\mathrm{sph}}^{\mathrm{av}}$.

The easy directions for the displacement are clearly seen along [100], [110] and [001]. A local minimum is also found along [111]. On the other hand, the maxima are found midway between [100] and [110], 25° from [110] to [001] and 65° from [110] to [001]. These maxima correspond approximately to the [210], [332] and [113] directions.

The dashed line in Fig. 4 marks the spherical average $E_{d,\mathrm{sph}}^{\mathrm{av}}$ which will be used later in the discussion of pseudo-random direction. The values of $E_{d,\mathrm{od}}^{\mathrm{av}}$ were summarized in Table 2. In bulk fcc Al, the orientation dependence of E_d is consistent with other studies of the displacement threshold energy in fcc Al [43,44] and the value of $E_{d,\mathrm{od}}^{\mathrm{av}}$ is within 2% of the $E_{d,\mathrm{sph}}^{\mathrm{av}}$.

Similar to bulk fcc materials, the orientation dependence of E_d in hcp structures was investigated by sweeping along high-symmetry paths [100] → [110] → [001] → [100]. As previously noted, the Miller indices are with respect to the primitive lattice vectors, hence [100] and [010] are along the close-packed directions while the [001] is the c-axis. Twenty-five simulations were performed at each direction. The results are shown in Fig. 5.

As in the case of fcc materials, both hcp Al and hcp Ti exhibit the same general features as functions of crystal direction for E_d. Easy displacements are found along the close-packed direction [100] and along the [221] direction. The [221] direction represents a vector connecting an atom in layer A to the nearest atom in layer B in hcp AB stacking. The exact locations for the high values of E_d are more difficult to determine since they usually involve high Miller indices. Compared to the existing work on hcp Ti, the peak near [110] and the local minimum at [001] are consistent with the cited work [45]. Interestingly, in the case of hcp Al, a local minimum at [001] is not evident. A possible explanation is due to the difference in the c/a ratio in hcp Al (1.724) compared to that in hcp Ti (1.586). As a reference, the ideal c/a ratio is $\sqrt{8/3} = 1.633$. The c/a ratio difference may also explain the peak near [111] in hcp Ti which somewhat diminishes in hcp Al.

3.2. Multilayer system

One of the motivations in this work is to investigate the effect of interfaces in a nanolayered structure on the displacement thresh-

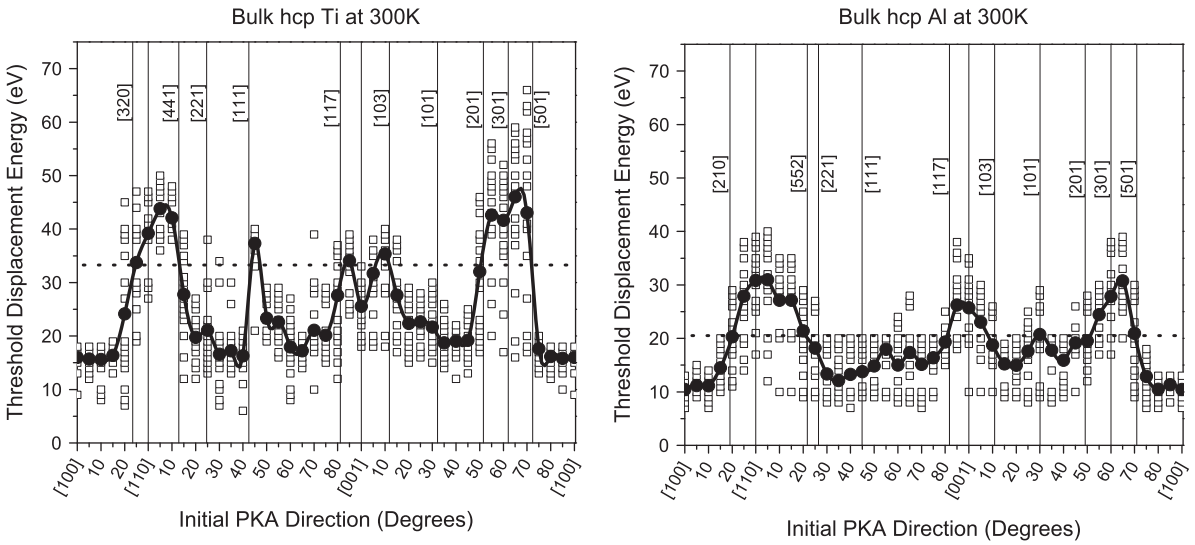

Fig. 5. Orientation dependence of the displacement threshold energy in the bulk hcp materials. Hollow squares denote the value of E_d from an individual trial at the given direction. The solid line and solid circles represent the trial average. The horizontal dashed line denotes the spherical average $E_{d,\mathrm{sph}}^{\mathrm{av}}$.

old energy. As for the bulk materials, the data is presented in two parts: random PKA directions and systematic sweeps of the crystal orientation.

3.2.1. Random PKA directions

In the multilayer system, the spherical average $E_{d,\mathrm{sph}}^{\mathrm{av}}$ was calculated using 200 random Al PKAs and 200 random Ti PKAs (total 400 PKAs) with randomly chosen initial directions. If the contribution from Al PKAs and Ti PKAs is separated, it is found that the $E_{d,\mathrm{sph}}^{\mathrm{av}}$ calculated from Al PKAs (25.2 eV) is increased compared to the $E_{d,\mathrm{sph}}^{\mathrm{av}}$ of bulk fcc Al (20.9 eV) and hcp Al (20.5 eV) structures. On the other hand, using Ti PKAs the value of $E_{d,\mathrm{sph}}^{\mathrm{av}}$ (22.4 eV) is reduced compared to that of bulk fcc Ti (35.4 eV) and hcp Ti (33.3 eV). Surprisingly, $E_{d,\mathrm{sph}}^{\mathrm{av}}$ of Ti PKAs is lower than that of Al PKAs. This is associated with defect partitioning in this nanolayered system which will be discussed later.

Fig. 6 shows the colormap spherical distribution of E_d in the multilayer. Comparing the map from Al PKAs in the multilayer to that of bulk fcc Al, one observes that the high values (green bins) in the multilayer case are distributed more toward higher z coordinate, i.e. towards the interface. A similar (albeit opposite) phenomenon occurs between the map from Ti PKAs and that from fcc Ti (note that the multilayer is fcc, consequently, fcc Ti is more appropriate than hcp Ti for comparison). In the latter case, the green bins in fcc Ti are purple in the multilayer with Ti PKAs towards high z coordinate, i.e. the displacement threshold from Ti PKAs directed towards the interface is lower than the corresponding direction in fcc Ti. The interesting thing is that the average value $E_{d,\mathrm{sph}}^{\mathrm{av}}$ in the multilayer (23.8 eV) is significantly smaller than the average values between that of fcc Al and fcc Ti ((20.9 + 35.4)/2 = 28.2 eV). Clearly, the presence of the interface in the multilayer affects the displacement threshold. The effects will be elucidated further in the later discussion about defect partitioning.

3.2.2. Crystal orientation dependence

In the multilayers, two sweeping patterns were used to determine the crystal orientation dependence of E_d. The first sweeping pattern covered directions $[100] \rightarrow [101] \rightarrow [010]$, the second set of directions was $[100] \rightarrow [010] \rightarrow [001]$. The first sweeping set is similar to that used for bulk fcc Al and fcc Ti, and is useful for comparison. Meanwhile, the second set of directions sweeps along the basal plane then towards the interface ([001] is normal to the interface), hence it helps elucidating the effects on E_d of PKAs directed towards the interface from PKAs directed parallel to the interface. For both sets, Al PKAs were randomly chosen from the multilayer, and 10 trials were performed for each direction of the sweeping pattern. The results are presented in Fig. 7. To be consistent with fcc Al and fcc Ti, the $E_{d,\mathrm{od}}^{\mathrm{av}}$ was calculated from the first sweeping pattern and given in Table 2.

First, we discuss the orientation dependence curve from the second set of sweeping directions (right panel in Fig. 7), as the two halves of the sweeping pattern (separated by a vertical line at [010]) differ only in their orientation with respect to the interfaces, a comparison between the sweep parallel to the interface $[100] \rightarrow [010]$ and the corresponding sweep in fcc Al reveals that the interface does not significantly affect E_d if Al PKAs are directed parallel to the interface. For directions normal to the interface E_d is evidently increased compared to that of fcc Al.

The orientation dependence for the fcc Al–Ti multilayer from the first set of directions is replotted in Fig. 8 together with the similar curves for bulk fcc Al and Ti, as well as the mean E_d value (referred to as bulk average curve). This clearly demonstrates that E_d in the fcc Al–Ti multilayer not given by the simple arithmetic mean of the bulk constituents. Comparing the multilayer curve and the bulk average curve, at [100] (parallel to the interface), the multilayer curve is lower than the bulk average, but very close to the fcc Al curve. This is expected since only Al PKAs are used in the multilayer curve. Then, as soon as the PKA is directed beyond 5° towards the interface, the multilayer curve is almost identical to the bulk average, and this persists up to about 20°. Beyond that angle, the multilayer curve is significantly larger than the bulk average towards [101] (45° towards the interface), in fact it is larger than the fcc Ti curve. By analyzing the location of the final defect, it was found that in the multilayer, the Al PKA directed towards the interface must displace Ti atoms to create a stable defect. This explains the higher value for the multilayer curve compared to the bulk average. Meanwhile, the higher value with respect to fcc Ti is understood from the fact that in the multilayer the Ti layers are under compressive strain, which effectively increases E_d as compared to that in a relaxed fcc Ti layer.

Continuing the sweep comparison from $[101] \rightarrow [010]$ (sweeping back down towards the plane parallel to the interface), the multilayer curve is larger than the bulk average until 20° and then becomes smaller than the bulk average with the exception of a small region around 75°. Hence, in general, when the PKAs are directed in the plane (or close to the plane) parallel to the interface, the multilayer layer curve is smaller than the bulk average and closer to the fcc Al curve due to the fact that Al PKAs were used and that the effect of interface is minimal in this case. On the other hand, when the PKAs are directed towards the interface, E_d is larger than the bulk average, in fact larger than fcc Ti, due to the higher displacement threshold of the compressed Ti layers. It is important to note that the orientation-dependence curve for the multilayer is only from Al PKAs. Nevertheless, it is sufficient to show that the

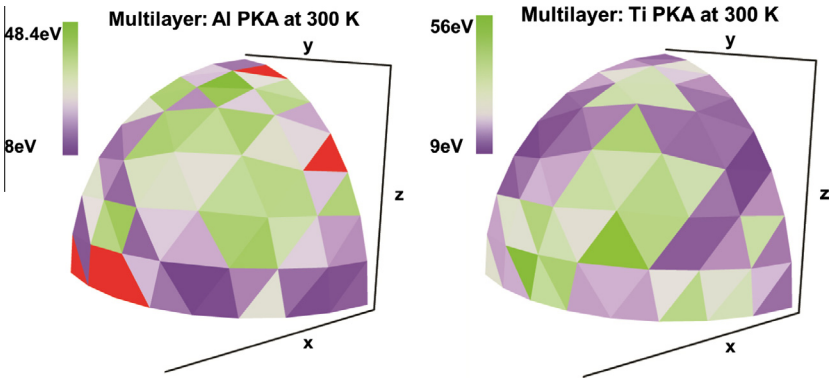

Fig. 6. Map showing the spherical distribution of displacement threshold energy in the fcc {100} Al–Ti multilayer (5 atomic layers per elemental layer) at 300 K. The distribution was obtained from PKAs randomly directed within the first octant of 3D space. Bins for which no trials were recorded are plotted in red. (For interpretation of the references to colour in this figure legend, the reader is referred to the web version of this article.)

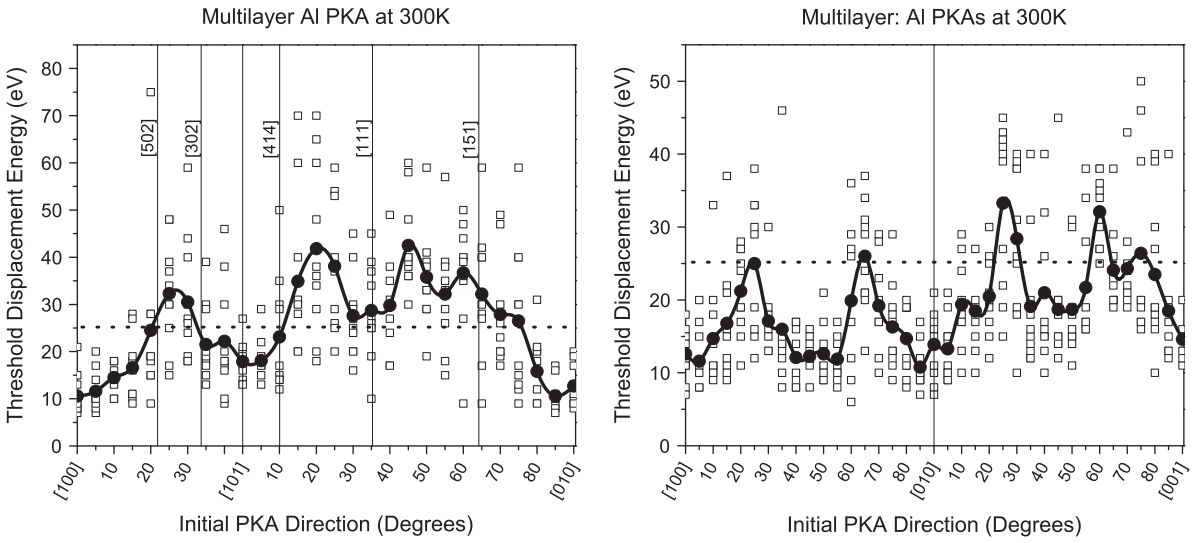

Fig. 7. Orientation dependence of the displacement threshold energy for Al PKAs in the Al–Ti fcc multilayer system. [001] is normal to the interface. Hollow squares denote the value of E_d from an individual trial in the given direction. The solid line and solid circles represent the trial average. The horizontal dashed line denotes the spherical average $E_{d,\mathrm{sph}}^{\mathrm{av}}$.

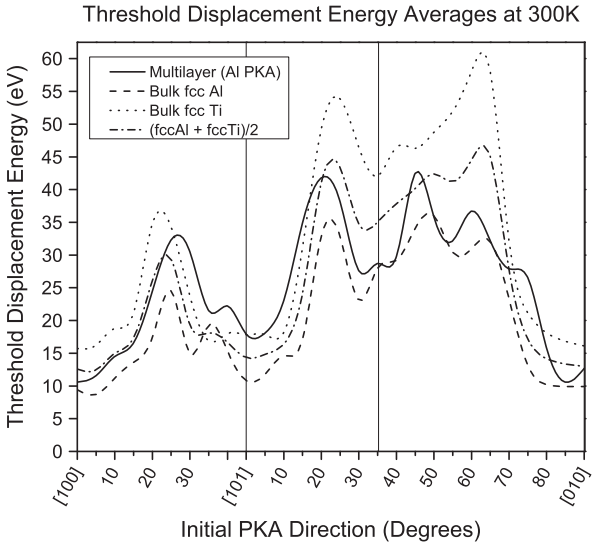

Fig. 8. Comparison of the orientation dependence of displacement threshold energy for bulk fcc Ti, bulk fcc Al, and Al PKAs in the Al–Ti multilayer.

interface plays a crucial role in affecting the displacement behavior in nanolayered systems.

3.2.3. Layer dependence and defect partitioning in multilayer

Choosing PKAs from a particular atomic layer is useful to isolate the effects seen at the interface. Fig. 9 shows E_d curves obtained from Al PKAs at atomic layers 6, 8 and 10 and Ti PKAs at atomic layers 11, 13 and 15. Note that the numbering of the atomic layer starting from the bottom is as follows: layers 1–5 are Ti layers, 6–10 are Al layers, 11–15 are Ti layers, and 16–20 are Al layers. Hence layers 8 and 13 reside in the middle of the respective Al and Ti layers. A simple sweeping pattern was used from parallel to normal to the interface along [100] → [001]. Comparing the overall trend of Al and Ti PKA curves, we see that both cases show maxima at around 20° and 70° and minima around 45°, which is associated with an easy replacement path along the close-packed direction [110] as previously discussed. However, there is an important difference when we compare the relative value of E_d

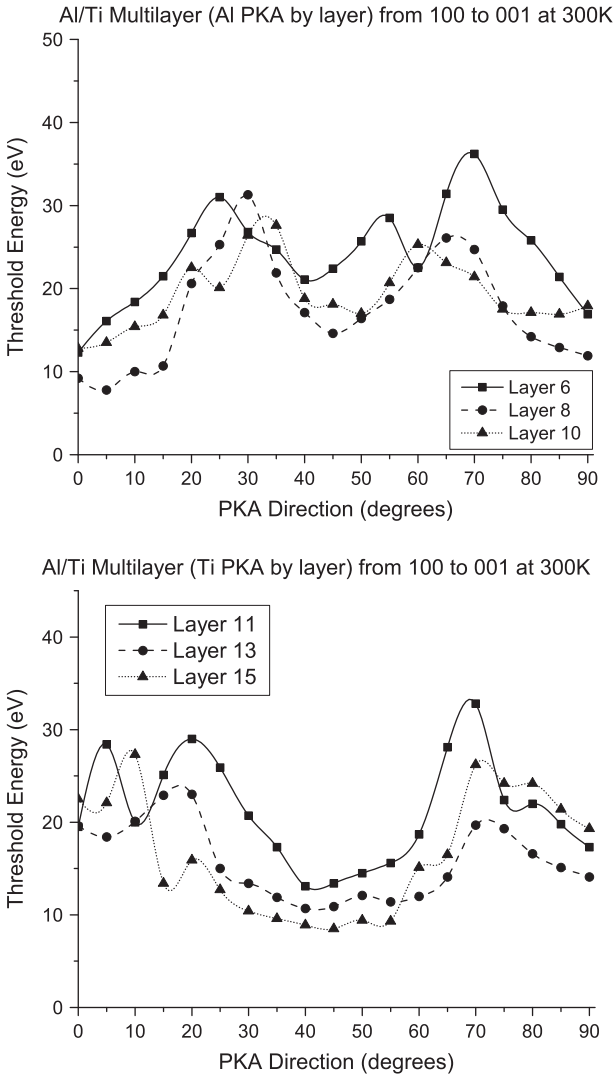

Fig. 9. Orientation dependence of displacement threshold energy in the Al–Ti multilayer initiated with PKA in a particular atomic layer. Sweep runs from [100] to [001].

in the 45° minima with respect to the value at [100]. For Ti PKAs, this corresponds to 50% decrease of the value at [100] (10 eV compared to 20 eV), while for Al PKAs, it is about 100% increase of the value at [100] (20 eV compared to 10 eV). This is understood from the fact that in the case of Al PKAs, the replacement path causes the defect to be formed in the Ti layer (hence higher E_d) while the opposite occurs in the Ti PKA case.

To analyze the layer-dependent behavior, it is useful to determine the location of the associated defect. Note that due to thermal vibration, trials from the same layer directed to the same orientation may result in a different location of a defect. Hence the defect location is calculated as the average number of interstitials that stabilize in the Al layer. The results are plotted in Fig. 10, which shows the fractions of interstitials in the Al layers as a function of the initial layer location of the PKA and the direction of the PKA. This curve is referred to as defect partitioning curve.

One of the striking effects of the interface is revealed from the defect partition curves for Al PKAs directed within 20° of [100] or within 20° parallel to the interface. In this condition, all interstitials are located in the Al region regardless of the initial location of the Al PKAs, even for Al PKA in layer 10 which is just below the Ti layer. This result is critical to understand defect partitioning in this multilayer system. It indicates that the displaced atoms from the Al layer are reflected back by the interface as long as the angle of incident is within 20° parallel to the interface. In this region of direction, the associated E_d curve (Fig. 9) clearly shows that the E_d from layer 8 is lower than that of layers 6 and 10. The lowest E_d of layer 8 is due to the fact that the most stable location for an interstitial in the Al layers is in the middle layer (layer 8) with formation energy of ~1.78 eV compared to that in the interface layer of Al which is ~2.03 eV. Once the PKA angle exceeds 20° then Ti atoms start to be involved in the displacement events. The fraction of interstitials in Al layers decreases since now some trials result in a stable defect in the Ti layers. In the Ti layer, an interstitial located at the interface layer is unstable and tends to stabilize in the next layer away from the interface with a formation energy of ~3.04 eV, while the formation energy of an interstitial in the middle layer in Ti layer is ~2.88 eV. Readers interested in the various formation energies of dumbbells in Al–Ti multilayers are referred to Ref. [46] in which we reported the effects of different interfaces as well as different multilayer thicknesses on displacement cascades.

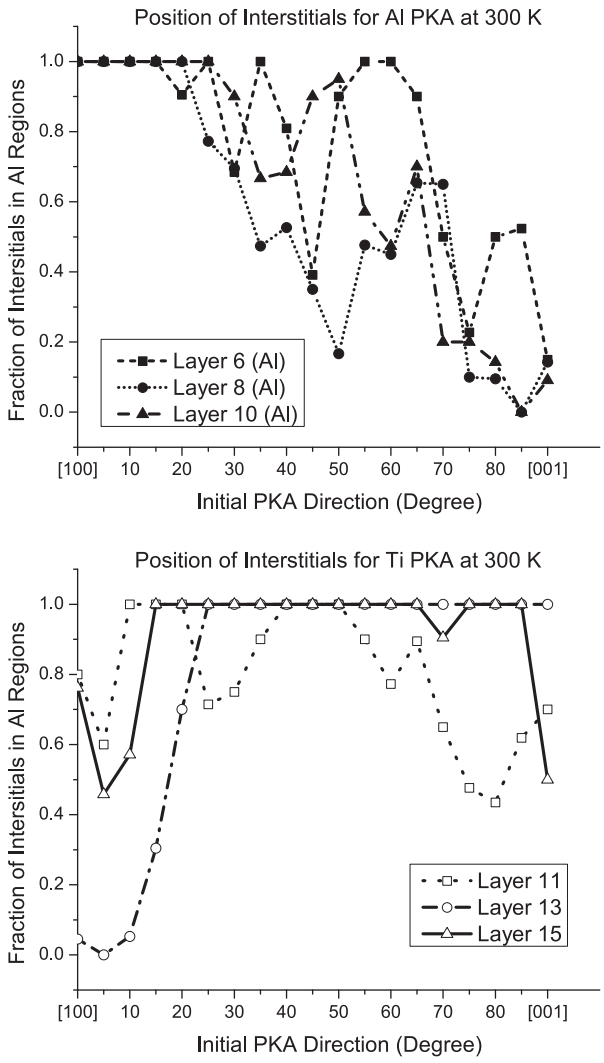

Fig. 10. Orientation dependence of the fraction of interstitials located in the Al layers in the Al–Ti multilayer initiated with PKA in a particular atomic layer.

The defect partitioning curve is even more striking in the case of Ti PKAs. The data at [100] illustrates an important property of the interface in this multilayer. In this direction parallel to the interface, Ti PKAs from the interface layers result in an interstitial in the nearby Al layer (i.e. Al layer below Ti layer for the case of Ti PKA at layer 11 and Al layer above Ti layer for the case of Ti PKA at layer 15), while Ti PKAs in the middle of the Ti layer (layer 13) create an interstitial within the Ti layer. Beyond 10° towards the interface, almost all trials result in an interstitial atom exclusively in Al layers.

Additional simulations were performed using 50 random Al PKAs and 50 random Ti PKAs with randomly oriented PKA directions. The result confirms that the interstitials are more likely to be found in Al layers, with 72.5% of interstitials from Al PKAs runs and 86% of interstitials from Ti PKAs runs are found in Al layers. Furthermore, 98% of the vacancies produced remain in the layer from which the PKA originated.

3.3. Pseudo-random direction

A large number of random directions are needed to calculate statistically sound average value of the displacement threshold energy $E_{d,\mathrm{sph}}^{\mathrm{av}}$. In this section, we combined the results from the randomly-directed PKAs as well as from the systematically-oriented PKAs to determine a pseudo-random direction, a direction whose E_d corresponds to the average $E_{d,\mathrm{sph}}^{\mathrm{av}}$. In this way, in the future, only a small number of PKA trials oriented towards the pseudo-random direction is needed to determine the $E_{d,\mathrm{sph}}^{\mathrm{av}}$. In all of the orientation-dependent E_d curves, a horizontal dashed line was plotted to mark the value of $E_{d,\mathrm{sph}}^{\mathrm{av}}$. Therefore, it is logical to determine the pseudo-random directions as the directions in the E_d curves that intersect the $E_{d,\mathrm{sph}}^{\mathrm{av}}$ line.

In bulk fcc Al, directions for which the trial average of E_d is equal to $E_{d,\mathrm{sph}}^{\mathrm{av}}$ are approximately in the [520], [210], [552], and [114] directions. Some of these directions are not ideal candidate for a pseudo-random direction as the direction is located along a steep slope in the E_d. As the pseudo-random direction is approximate in nature, rapid variations of E_d with respect to initial PKA directions are problematic. The [552] and [114] directions are therefore less accurate than [520] and [210]. For bulk fcc Al this leaves the [520] and [210] directions as the best candidates for pseudo-random directions. As expected, the same set of pseudo-random directions are found for the fcc Ti.

In bulk hcp Ti, the candidates are [320] in the basal plane, [441], [111], [117], [103], [201], and [501]. For hcp Al, the candidates are [210] in the basal plane, [552], [117], [103], [101], [201], and [501]. Directions that appear in both hcp Ti and hcp Al are [117] and [103] (both around [001]) and [201] and [501]. The [201] and [501] in hcp Ti exhibit a steep slope. Hence,

pseudo-random directions that work for both hcp Ti and hcp Al are the [103] and [117] directions.

For Al PKAs in the fcc {100} Al–Ti multilayer, the candidates for pseudo-random direction are [502] (21.8° in Fig. 7), [302] (33.7°), [414] (10.0°) and [151] (74.2°). The [502] direction also appears as a good choice in fcc Al and fcc Ti. In the multilayer, the [502] direction has a component that is normal to the interface, hence it is considered to be the representative choice for pseudo-random direction in this multilayer. However, It is unclear if this direction would remain viable for other interface configurations.

4. Conclusion

MD simulations were performed to demonstrate that interface in fcc [100] Al–Ti nanolayered structure significantly affects the displacement threshold energy E_d. Near the interface, it is easier for the heavier Ti atoms to displace the lighter Al atoms resulting in preferential location of interstitials in the Al layers. This characteristic of Al–Ti nanolayer results in a decreased value of E_d compared to the average response of the constituent materials. On the other hand, ~98% of the vacancies remain in the layer where the PKAs initially originate. Hence, in this nanolayered system, interstitials and vacancies are effectively separated by the interfaces. This defect partitioning effect is expected to reduce radiation damage recovery in this nanolayered system compared to multilayered systems that might not undergo such defect partitioning. However, it is very likely that such partitioning is an intrinsic response of multilayer systems to collision cascade damage. Therefore, a major conclusion from this research is that observed asymmetries in radiation damage response of multilayered films can be partly attributed to the initial defect partitioning during collision cascade damage and that such defect partitioning should be more carefully studied for other multilayered systems, such as Cu–Nb, that have been quite thoroughly characterized except for this. Further, defect annealing at longer times, which was not considered here, may also follow unequal fates depending on the individual layer constituents and the dissimilar interface.

Additionally, an open-source software was written to determine the location of the radiation-induced point defects, to construct spherical grids and to calculate the spherical average displacement threshold energy $E_{d,\mathrm{sph}}^{\mathrm{av}}$ from randomly-directed PKAs. The value of $E_{d,\mathrm{sph}}^{\mathrm{av}}$ was combined with the orientation-dependent curve of E_d along systematic crystallographic directions to determine a pseudo-random direction that can be used to efficiently determine $E_{d,\mathrm{sph}}^{\mathrm{av}}$ without performing the time-consuming random simulations. It was found that the representative choices of pseudo-random direction are: along [520] and [210] for fcc Al and fcc Ti, along [103] and [117] for hcp Ti and hcp Al, and along [502] for the fcc 100 nanolayered Al–Ti system considered in this work.

Acknowledgments

This research was supported by the award BRCALL08-Per4-E-1-0062 from Defense Threat Reduction Agency (DTRA). A portion of this research was performed using Olympus supercomputer at EMSL (#44724), a national scientific user facility sponsored by the Department of Energy's Office of Biological and Environmental Research and located at Pacific Northwest National Laboratory.

Appendix A. Synopsis of AXIS software

The open-source software AXIS was developed for this work. In this version, it contains features for point defects detection and the calculation of spherically-averaged values (e.g. $E_{d,\mathrm{sph}}^{\mathrm{av}}$) and its associated statitistics by construction of spherical grids using equilateral triangular grids in the first octant of 3D space and bilinear interpolation. AXIS is written in c++ with access to unix's piping and shell scripting for modularity. It is suited for the automation of post-processing. The code can be compiled on Linux machines, Mac and Windows (using cygwin) as a stand-alone executable or as a library. Compilation instructions can be found in the README file distributed with the source code given as supplemental materials of this paper. In this section, several examples of the usage are presented.

```
axis --help
```
Print out the synopsis.

```
axis --pdefect < in.dump
axis --pdefect 1.0 < in.dump
```

Detect point defects based on the occupancy of lattice sites within 1.0 Å radius (default is 0.8 Å if unspecified). The input in.dump follows LAMMPS dump file format. The lattice sites are taken from the first configuration in the in.dump. Output to stdout with format:

```
FoundInterstitial
Number of intersitials: I
Positions of interstitials
FoundVacancy
Number of Vacancies: V
Positions of vacancies
```

If no interstitials or vacancies are found, then it outputs only the key word "NoneFound" The positions of the interstitials are the actual coordinates of interstitial atoms residing in lattice sites with occupancy more than one (note that all atoms in such sites are outputted) while the locations of the vacancies are taken from the coordinates of the unoccupied lattice sites.

```
axis --defect < in.dump
axis --defect 2.75 < in.dump
```

Detect point defects based on Wigner–Seitz cells occupancy. This option employs the cell lists algorithm to do the spatial decomposition to speed up the calculation. In the above example, the space is divided into cells with edge length 2.75 Å (default is 3.0 Å if unspecified). This option is more robust and efficient than the --pdefect option. The shape of the cells follows the lattice vectors used in the in.dump file. The Wigner–Seitz cells are constructed from the first configuration in the in.dump file. Output files are inters.dump, refinters.dump and vac.dump. The inters.dump contains the actual coordinates of interstitial atoms residing in lattice sites with occupancy more than one (note that all atoms in such sites are output) while vac.dump contains the coordinates of the unoccupied lattice sites, and refinters.dump contains the coordinates of lattice sites where the interstitial atoms reside.

```
axis --sgrid 64
```

Create a spherical grid of size 64. Output the (θ, ϕ) spherical coordinates of the center of each grid in degrees. As usual, θ is the polar angle measured from $+z$ while ϕ is the azimuthal angle measured from $+x$ on xy plane.

```
axis --smean 64 < infile > outfile
```

Compute a spherical average of values using 64 grids.

Format of infile:

θ_1 ϕ_1 value$_1$
θ_2 ϕ_2 value$_2$
...

Angles are in degrees.

Format of outfile:

−−Bin Averages−−
θ_1 ϕ_1 binaverage$_1$
θ_2 ϕ_2 binaverage$_2$
...
θ_{64} ϕ_{64} binaverage$_{64}$
−−Total Average−−
spherical_average
axis −−smean 64 BinCount < infile > outfile

The BinCount argument will write additional information on the number of trials in each grid in the outfile with format:

θ ϕ bin_average bin_count
...
axis −−smean 64 OFF < infile > outfile
axis −−smean 64 OFF_C_G < infile > outfile
axis −−smean 64 OFF_C_PG < infile > outfile

The argument OFF, OFF_C_G or OFF_C_PG will write to stdout with the GEOMVIEW's.off file format that can be used to generate surface plots (e.g. the colormap figures in this paper). Different arguments specify different color maps. Details of file formats can be found in the help file.

References

[1] G. Was, Fundamentals of Radiation Materials Science, 1st ed., Springer-Verlag, 2007.
[2] M.L. Lescoat, J. Ribis, A. Gentils, O. Kaitasov, Y. de Carlan, A. Legris, J. Nucl. Mater. 428 (2012) 176.
[3] P. He, M. Klimenkov, R. Lindau, A. Moslang, J. Nucl. Mater. 428 (2012) 131.
[4] L. Hsiung, M. Fluss, S. Tumey, J. Kuntz, B. El-Dasher, M. Wall, B. Choi, A. Kimura, F. Willaime, Y. Serruys, J. Nucl. Mater. 409 (2011) 72.
[5] S. Ukai, S. Ohtsuka, Energy Mater. 2 (2007) 26.
[6] M.K. Miller, K.F. Russell, D.T. Hoelzer, J. Nucl. Mater. 351 (2006) 261.
[7] R. Lindau, A. Moslang, M. Rieth, M. Klimiankou, E. Materna-Morris, A. Alamo, A.A.F. Tavassoli, C. Cayron, A.M. Lancha, P. Fernandez, N. Baluc, R. Schaublin, E. Diegele, G. Filacchioni, J.W. Rensman, B. Schaaf, E. Lucon, W. Dietz, Fusion Eng. Des. 75 (2005) 989.
[8] G.R. Odette, M.J. Alinger, B.D. Wirth, Ann. Rev. Mater. Res. 38 (2008) 471.
[9] Y. Wu, E.M. Haney, N.J. Cunningham, G.R. Odette, Acta Mater. 60 (2012) 3456.
[10] A. Misra, M.J. Demkowicz, X. Zhang, R.G. Hoagland, JOM 59 (2007) 62.
[11] H.L. Heinisch, F. Gao, R.J. Kurtz, J. Nucl. Mater. 329 (2004) 924.
[12] X. Zhang, E.G. Fu, N. Li, A. Misra, Y.Q. Wang, L. Shao, H. Wang, J. Eng. Mater. Technol., Trans. ASME 134 (2012) 041010.
[13] P.D. Edmondson, C.M. Parish, Y. Zhang, A. Hallen, M. Miller, Scripta Mater. 65 (2011) 731.
[14] G.R. Odette, D.T. Hoelzer, JOM 62 (2010) 84.
[15] A. Kashinath, A. Misra, M.J. Demkowicz, Phys. Rev. Lett. 110 (2013) 086101.
[16] M. Demkowicz, A. Misra, A. Caro, Curr. Opin. Solid State Mater. Sci. 16 (3) (2012) 101.
[17] M. Zhernenkov, M.S. Jablin, A. Misra, M. Nastasi, Y. Wang, M.J. Demkowicz, J.K. Baldwin, J. Majewski, Appl. Phys. Lett. 98 (2011) 241913.
[18] K. Hattar, M. Demkowicz, A. Misra, I. Robertson, R. Hoagland, Scripta Mater. 58 (2008) 541.
[19] T. Höchbauer, A. Misra, K. Hattar, R.G. Hoagland, J. Appl. Phys. 98 (2005) 123516.
[20] M. Demkowicz, Y. Wang, R. Hoagland, O. Anderoglu, Nucl. Instrum. Methods Phys. Res. Sect. B: Beam Interact. Mater. Atoms 261 (2007) 524.
[21] M.J. Demkowicz, D. Bhattacharyya, I. Usov, Y.Q. Wang, M. Nastasi, A. Misra, Appl. Phys. Lett. 97 (2010) 161903.
[22] D. Bhattacharyya, M. Demkowicz, Y.-Q. Wang, R. Baumer, M. Nastasi, A. Misra, Microsc. Microanal. 18 (2012) 152.
[23] M. McPhie, L. Capolungo, A. Dunn, M. Cherkaoui, J. Nucl. Mater. 437 (2013) 222.
[24] N. Li, M. Nastasi, A. Misra, Int. J. Plast. 32 (2012) 1.
[25] E. Fu, J. Carter, G. Swadener, A. Misra, L. Shao, H. Wang, X. Zhang, J. Nucl. Mater. 385 (2009) 629.
[26] N. Li, J. Carter, A. Misra, L. Shao, H. Wang, X. Zhang, Philos. Mag. Lett. 91 (2011) 18.
[27] Q. Wei, Y. Wang, M. Nastasi, A. Misra, Philos. Mag. 91 (2011) 553.
[28] E. Fu, H. Wang, J. Carter, L. Shao, Y. Wang, X. Zhang, Philos. Mag. 93 (2013) 883.
[29] R.R. Zope, Y. Mishin, Phys. Rev. B 68 (2003) 024102.
[30] G. Kresse, J. Hafner, Phys. Rev. B 47 (1993) 558.
[31] G. Kresse, J. Furthmüller, Phys. Rev. B 54 (1996) 11169.
[32] P.E. Blöchl, Phys. Rev. B 50 (1994) 17953.
[33] G. Kresse, D. Joubert, Phys. Rev. B 59 (1999) 1758.
[34] J.P. Perdew, K. Burke, M. Ernzerhof, Phys. Rev. Lett. 77 (1996) 3865–3868.
[35] J.F. Ziegler, J.P. Biersack, U. Littmark, The Stopping and Range of Ions in Solids, Pergamon, New York, 1985.
[36] M. Hossain, J. Freund, H. Johnson, Nucl. Instrum. Methods Phys. Res. Sect. B: Beam Interact. Mater. Atoms 267 (2009) 1061.
[37] S. Plimpton, J. Comput. Phys. 117 (1995) 1.
[38] K. Nordlund, J. Wallenius, L. Malerba, Nucl. Instrum. Methods Phys. Res. Sect. B: Beam Interact. Mater. Atoms 246 (2006) 322.
[39] D. Bacon, F. Gao, Y. Osetsky, J. Nucl. Mater. 276 (2000) 1.
[40] G. Sattonnay, F. Rullier-Albenque, O. Dimitrov, J. Nucl. Mater. 275 (1999) 63.
[41] G.W. Iseler, H.I. Dawson, A.S. Mehner, J.W. Kauffman, Phys. Rev. 146 (1966) 468.
[42] H.H. Neely, W. Bauer, Phys. Rev. 149 (1966) 535.
[43] P. Vajda, Rev. Modern Phys. 49 (1977) 481.
[44] W.E. King, K.L. Merkle, M. Meshii, Threshold energy surface and frenkel pair resistivity for Cu, in: Proceedings of the Symposium on Radiation Damage Analysis for Fusion Reactors, 25–28 October 1982, J. Nucl. Mater. (Netherlands) 117 (1982) 12.
[45] S.J. Wooding, D.J. Bacon, Radiat. Eff. Defects Solids (1994) 461.
[46] W. Setyawan, M. Gerboth, B. Yao, C.H. Henager Jr., A. Devaraj, V. Vemuri, S. Thevuthasan, V. Shutthanandan, Asymmetry of radiation damage properties in Al–Ti nanolayers, J. Nucl. Mater. 445 (2014) 261.

Pacific Northwest
NATIONAL LABORATORY

U.S. DEPARTMENT OF
ENERGY

Proudly Operated by Battelle *Since 1965*

902 Battelle Boulevard
P.O. Box 999
Richland, WA 99352
1-888-375-PNNL (7665)
www.pnnl.gov